FACULTY OF ENGINEERING AND ARCHITECTURE

Experimental and numerical characterisation of the consolidation behaviour of woven fabrics for the production of composites

Brecht Tomme
Student number: 01201015

Supervisors: Prof. dr. ir. Karen De Clerck, Prof. dr. ir. Wim Van Paepegem
Counsellor: Dr. ir. Lode Daelemans

Master dissertation submitted in order to obtain the academic degree of
Master of Science in Sustainable Materials Engineering

Academic year 2018-2019

GHENT UNIVERSITY

FACULTY OF ENGINEERING AND ARCHITECTURE

Experimental and numerical characterisation of the consolidation behaviour of woven fabrics for the production of composites

Brecht Tomme
Student number: 01201015

Supervisors: Prof. dr. ir. Karen De Clerck, Prof. dr. ir. Wim Van Paepegem
Counsellor: Dr. ir. Lode Daelemans

Master dissertation submitted in order to obtain the academic degree of
Master of Science in Sustainable Materials Engineering

Academic year 2018-2019

GHENT UNIVERSITY

Preface

My bachelor thesis on nanofibre toughened composite materials really piqued my interest in the material class. When it came to choosing the topic for my master dissertation, then, the decision was easy. A lot of research concerning final material properties had already been done at the Department of Materials, Textiles and Chemical Engineering (MaTCh), so I decided to delve deeper into the production process necessary to reach that end product. Originally, I wanted this dissertation to be about experimental characterisation, but it ended up being focused on numerical modelling. This was challenging, as I had no experience in numerical modelling whatsoever, but I learnt a great many new things along the way. While this dissertation requires expanding on to yield results applicable to industry, I hope the model created here and the concepts outlined can serve as a basis for further research.

I would like to express my gratitude towards my promotors, Karen De Clerck and Wim Van Paepegem, for allowing me to investigate this topic and providing early feedback. I also wish to extend a huge thank you to my supervisor, Lode Daelemans, for always being available, answering every question I had, explaining new concepts and programs to me, helping me when I got stuck, and understanding when real life got in the way of research. I am additionally grateful towards Matthieu Boone, Jeroen Van Stappen, Maxim Deprez and Iván Josipovic at the Ghent University Centre for X-ray Tomography (UGCT), for their expertise in computed tomography, and Olivier Verschatse and Sander Rijckaert for their help around the lab. Last, but certainly not least, I would like to thank my family and friends, for supporting me throughout this project. Particularly, I would like to thank Astrid, Toon and Ester for their unconditional friendship, Jari for proving to me that personal problems can be worked through, Yentl and Lotte for continuously motivating me, Bianca, Robbe, Serge, Michiel, Dylan and Wouter for "suffering" through thesis life alongside me, my brother Michiel for keeping me entertained and my parents for their care and support.

Brecht Tomme, May 2019

Abstract

Fibre reinforced polymers (FRPs) are part of a growing market, mostly thanks to their high specific strength and stiffness. This makes them invaluable in the transportation and construction sector, for example to reduce fuel costs. All industrial FRP manufacturing processes have one thing in common: at some point during the process, pressure is applied to consolidate the reinforcing fabric. While required, this can also introduce defects into the model, leading to reduced mechanical properties or even failure. As such, there is a need for predictive tools that can model consolidation numerically.

In this dissertation, an attempt is made to construct such a fabric model in the finite element package ABAQUS. The discrete meso-scale model is built by superimposing truss and beam elements on a chain at (microscopic) fibre level, to decouple the fabric's Young's modulus and flexural rigidity. These fibres are then assembled into yarns and further integrated into a fabric. Weaving of the fabric is simulated by thermal shrinkage to reach an as-woven state, where the model is validated with experimental data gathered via micro-computed tomography (µCT)-scans. The as-woven state is then used as the input for a compression simulation. The results of this are compared to experimental results gathered from µCT images of a compression experiment carried out on a dry fabric sample.

The created truss-and-beam model proved to be an improvement over a truss-only model, but still requires finetuning to become accurate enough to be industrially useful.

Keywords

Fabric consolidation, compression behaviour, finite element analysis (FEA), ABAQUS, truss-and-beam model, discrete meso-scale model

Experimental and numerical characterisation of the consolidation behaviour of woven fabrics for the production of composites

Brecht Tomme

Supervisor(s): prof. dr. ir. Karen De Clerck, prof. dr. ir. Wim Van Paepegem, dr. ir. Lode Daelemans

Abstract— **Fibre reinforced polymers (FRPs) provide high strength and stiffness properties at a low structural mass. This offers potential in many industries, most notably in the construction and transportation sectors. These FRPs are manufactured using different processes, but one thing they all have in common is a consolidation stage. In this stage, any reinforcing fibres are subjected to pressure to increase their fibre volume fraction (V_f). This serves to improve the mechanical properties of the final part, but can also introduce defects, having the opposite effect. Effective simulations of the consolidation stage are thus required to avoid problems before they occur, saving time and money, and reducing environmental impact.**

This study attempts to construct a fabric model for consolidation simulation in the finite element package ABAQUS. A discrete meso-scale model is built by superimposing truss and beam elements at the fibre level, to decouple the fabric's Young's modulus and flexural rigidity. Weaving of the truss-and-beam model is replaced by applying thermal shrinkage. Parameters of the as-woven model are investigated and the model is validated by comparison with experimental data gathered via micro-computed tomography (µCT). The as-woven model is then used as the input for a compression simulation, which is compared to a compression experiment.

The truss-and-beam model exhibits more accurate consolidation behaviour than a truss-only model, which serves as a good proof of concept, though improvements to the model are necessary before use in industrial or research applications.

Keywords— **Fabric consolidation, compression behaviour, finite element analysis, ABAQUS, truss-and-beam model, discrete meso-scale model**

I. Introduction

THE composite materials market is continuously growing, as major industrial drivers demand ever-increasing amounts of light structural materials. The construction and transport sectors, especially, appreciate FRPs' high specific strength and toughness, notably for the production of lighter moving parts,, which greatly reduce fuel costs. FRP parts are made by different processes, balancing cost and quality. In all these processes, however, consolidation takes place. This implies that the reinforcing fibres get compressed to increase their Vf - one of the main parameters that influence the material properties.

Consolidation of a fabric is described in literature as occurring in three stages; see figure 1. In stage 1, any crimp inequalities between warp and weft directions are balanced out by yarn flattening. Here, compression is linear with pressure. In stage 2, individual fibres within yarns are compressed together, removing voids in the material and deforming the yarn cross sections. This becomes more difficult as fibres come into contact with each other, making compression exponential with pressure. In stage 3, void removal and fibre displacement have reached their limit, and further compaction requires elastic deformation of the fibres. This is again linear with pressure [1] [2] [3]. Nesting is also described to occur in multilayer fabrics. This

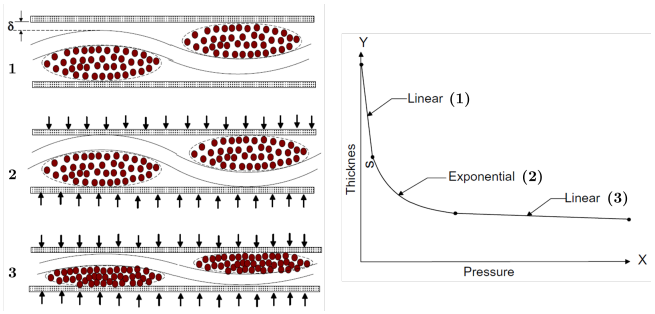

Fig. 1. The three-stage consolidation process for fabrics described in literature.

is the phenomenon where fabric layers slide into each other, aligning the yarn "hills" of one layer with the yarn "valleys" of an adjacent layer, reducing the total thickness [4].

During consolidation, defects can be introduced in a FRP. The main defects produced by compression during consolidation are porosity and fibre waviness [5]. Both can have severe effects on the mechanical properties of a composite, reducing interlaminar shear strength, transverse tensile strength, compressive strength, flexural modulus and strength, and fatigue life, often leading to failure.

To predict consolidation behaviour and avoid defects, analytical fabric models are required. Often, finite element models are used, which can be classified according to their multi-scaled nature [6]. Macro-scale models focus on the fabric as a whole - continuous models assume the fabric is a continuous material and model this using membrane or shell elements, while discrete models divide the fabric up into simplified yarns in the shape of a pin-jointed net. Meso-scale models focus on the yarns - continuous models view the yarns as three dimensional solid continuum elements, while discrete models break down the yarns into an amount of fibres. Particularly interesting is the discrete meso-scale model introduced by Zhou et al. [7], that models fibres as chains of truss elements connected by frictionless pins. Micro-scale models focus on the fibres, and a true micro-scale model would require every individual fibre to be simulated. As this is computationally expensive, micro-scale models are rare.

In this study, a discrete meso-scale model will be built to simulate consolidation behaviour. The parameters of this model will be investigated, and the model will be validated, by comparing its geometry to that of the real fabric it attempts

to model. The created model will then be used as the input for a compression simulation. Additionally, consolidation will be examined experimentally by setting up a compression experiment.

II. Materials and methods

The fabric modelled in this study is a 2/2 twill, E-glass fibre, woven fabric produced by P-D Interglas Technologies GmbH. It will be modelled in Abaqus Unified FEA (ABAQUS), version 6.18-1 (2018), by Dassault Systèmes. Python version 3.7.3 will be used to easily construct input files for ABAQUS.

Any experimental data is gathered from μCT images, generated by the HECTOR tomograph at the Ghent University Centre for X-ray Tomography. This scanner uses an XWT 240-SE microfocus source and a large PerkinElmer flat panel detector, allowing for images with a maximum spatial resolution of approximately 10 μm. ImageJ version 1.52i (contained within the Fiji distribution package, version "Madison") is employed to measure distances on the reconstructed μCT images.

The compression experiment carried out in this study uses a uniaxial CT5000-TEC compression cell by Deben (UK). The device is controlled by Deben Microtest software and uses a load cell with a maximum force of 1 kN. During the experiment, a constant strain rate of 0.5 $\frac{\text{mm}}{\text{min}}$ is applied to a single layer or four layer dry fabric sample.

III. Fabric model creation

A. Fibre model (micro-scale)

One of the main problems encountered in literature is that existing fibre models cannot accurately represent both material stiffness (i.e. the Young's modulus) and flexural rigidity, simultaneously. This is because flexural rigidity is defined as $E \cdot I$, the Young's modulus multiplied by an area moment of inertia. Assuming fibres have a circular cross section, this area moment of inertia is only dependent on the fibre geometry, namely its radius. Yet fibres, unlike metals, polymers or ceramics, have an unusually high stiffness in their fibre direction, coupled with a very low flexural rigidity. Applying this high Young's modulus, then, automatically creates an overestimation of the flexural rigidity. To remedy this, many fibre models use truss elements, which can only transmit axial forces (no bending moments or shear forces), and thus negate flexural rigidity completely. It is not an entirely negligible property, however, as it plays a crucial role in any simulations involving the bending of fibres, such as those simulating consolidation.

In this study, the Young's modulus and flexural rigidity are decoupled at the fibre level. Material stiffness is assigned to fibres by using T3D2 truss elements on a flexible chain of nodes, as in [7]. Flexural rigidity is then assigned separately by superimposing B31 beam elements onto the truss elements, between the same nodes. Beam elements are similar to truss elements but also transmit bending moments and shear forces. These superimposed beam elements can be given a drastically reduced Young's modulus (factor $\frac{1}{100}$) so as not to affect the actual stiffness of the fibres, but can be made large enough to still represent an accurate flexural rigidity by having a large area moment of inertia. The beams will become larger than the trusses, but they are purposefully not given any contact interaction properties in ABAQUS, to ensure they do not affect the fabric geometry in any way except by contributing their flexural rigidity. The actual fabric geometry will be represented by the truss elements.

B. Yarn model (meso-scale)

At the mesoscopic scale, yarns are constructed out of these truss-and-beam fibres. The real fabric contains 2314 fibres per yarn in the warp direction and 1841 fibres per yarn in the weft direction, but modelling this many yarns would be very computationally expensive. As such, only 61, 91 or 127 virtual fibres are included per yarn, in a hexagonal closed packing. This smaller amount of virtual fibres still needs to represent the same cross sectional area as the real fibres, so the individual cross sectional areas of the truss elements were increased:

$$A_{total,virtual} = A_{total,real} \tag{1}$$

$$\Leftrightarrow n_{virtual} \cdot A_{fibre,virtual} = n_{real} \cdot A_{fibre,real} \tag{2}$$

A represents the cross sectional area, and n represents the amount of fibres per yarn. This calculation results in virtual cross sectional areas that are two orders of magnitude higher than the real cross sectional areas.

It is also at this scale that the flexural rigidity of the yarn is assigned. This must be equal in total for the virtual yarn and the real yarn:

$$(E \cdot I)_{yarn,virtual} = (E \cdot I)_{yarn,real} \tag{3}$$

$$\Leftrightarrow n_{virtual} \cdot (E \cdot I)_{fibre,virtual} = (E \cdot I)_{yarn,real} \tag{4}$$

Remember that the Young's modulus in the equation for the virtual flexural rigidity is $\frac{1}{100}$ of the actual Young's modulus. From this formula, the required dimensions of the beam elements can be calculated, as long as the flexural rigidity of the real yarns is known. This is measured according to BS 3356 (1961), based on the Peirce cantilever test. An accurate yarn number is required to calculate the flexural rigidity, which is measured according to ISO 7211/5 and ISO 7211/3 (1984).

C. Fabric model (meso-scale)

The yarn model constructed thus far is integrated into an existing fabric model by Daelemans at the macroscopic scale. This model was built to emulate the same 2/2 twill weave E-glass fibre fabric that is studied here. A single unit cell consisting of four warp and four weft yarns was modelled, and boundary conditions were applied by using constraint equations and a master-slave yarn system, ensuring perfect periodicity. Evolution from the idealised, created model to the as-woven state was realised by applying a negative thermal load (thermal shrinkage), until the crimp in the virtual fabric matched that of the real fabric, as in [8]. The existing model was constructed in the same way as the model in this study at micro- and meso-scale, with the large difference being that it only used truss elements. As such, it could not model consolidation accurately.

The new truss-and-beam fabric model is created by first updating all the linearly elastic material properties in the

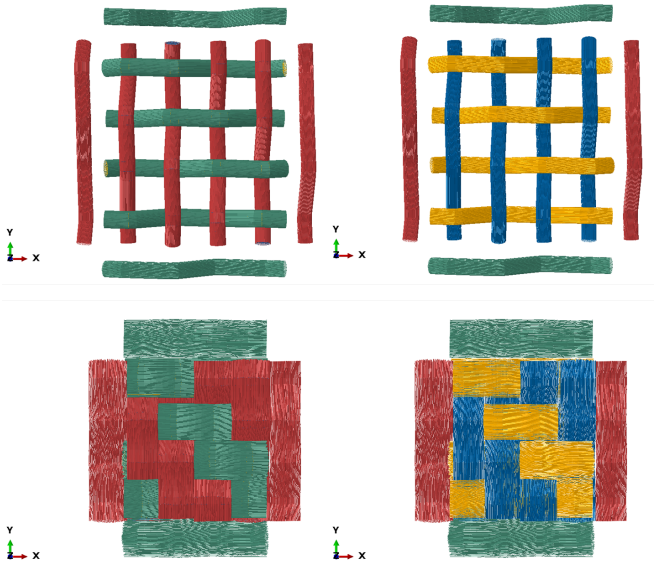

Fig. 2. The combined truss-and-beam fabric model (127 fibres per yarn) in its undeformed state (top) and its as-woven state (bottom). The truss elements (yellow and blue) determine the stiffness of the material and its real geometry while the beam elements (green and red) contribute their flexural rigidity. The outer slave yarns only serve as boundary conditions.

ABAQUS input file via a custom Python script. Accurate densities and estimates of the Young's modulus and Poisson coefficient are inserted. The main change to the truss model is then due: the superposition of beam elements on top of the existing truss elements. This is again achieved via a Python script, and the beam elements are defined as circular sections between the same nodes that hold the truss elements. Their Young's modulus is lowered by a factor 100 and their radius is set at the value required to reach the correct flexural rigidity of the yarn. A version of the completed model is shown in figure 2.

IV. Fabric model validation

To validate the constructed model, real fabric samples are µCT-scanned, and yarn widths are measured on the reconstructed images it provides. These widths are then compared to the yarn widths of the as-woven truss-and-beam fabric model, measured in ABAQUS. Several different simulations are run, investigating the effect of the amount of fibres per yarn, the coefficient of friction, the time step and the weaving process. While the µCT images are of low quality due to low resolution, high noise and low contrast, general conclusions can still be made.

With increasing amounts of fibres per yarn, it is found that the yarn width within the model increases, even though each yarn has the same total cross sectional area contained in its constituent fibres. The yarn width variability (standard deviation on the measurement) also increases, which can be explained by the fact that fibres with smaller diameters (more fibres per yarn) can migrate out of the yarn more easily in an inconsistent manner.

The coefficient of friction is a measure for interfibre friction

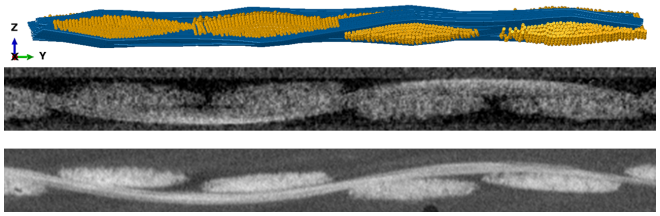

Fig. 3. A warp cross section view of the final as-woven truss-and-beam model with 127 fibres per yarn and a coefficient of friction of 0.10, deformed in a time step of 0.06 s via a two-stage weaving process. The cross section is compared to real cross sections imaged via µCT-scanning.

as instated in the contact interactions between truss elements. The lower this coefficient gets, the larger the yarn widths become, as the fibres are less hindered from slipping along each other. This leads to the irregular fanning out of fibres, accompanied by an increase in the yarn width variability.

Increasing the time step of the simulation (the real time given to ABAQUS to perform the simulation in, not the time it takes to compute it) seems to lead to more variable yarn widths, though no clear increase or decrease in yarn width is noticed. This may be a product of the inertia effects that are taken into account in dynamic simulations, where the kinetic energy is higher than the internal energy for the model. Increasing the time step is found to lead to more dynamic simulations.

The final investigated parameter is the "weaving" process (by thermal shrinkage, not actual weaving). This process can be modelled in one stage, evolving directly from the loose topology to the as-woven state with the correct crimp values, or it can be modelled in two stages. In that case, the first stage emulates the actual weaving process by applying higher tensions than required, and the second stage then allows the model to relax from this weaving process, reaching the desired crimp value. Daelemans found that the one-stage process lead to more stressed yarns in the truss-only model. This is repeated here, as smaller yarn widths are found for the one-stage weaving process, though variability does not increase or decrease. It is also determined that care should be taken with the two-stage weaving process, as it easily leads to dynamic simulations.

In the end, the model agreeing most with experimental measurements is found to be a model with 127 fibres per yarn, a coefficient of friction of 0.10, deformed in a time step of 0.06 s via a two-stage weaving process. A cross section of this model is shown in figure 3.

V. Fabric consolidation

A. Experimental compression

The compression experiment in this study is carried out by allowing the Deben cell to apply increasing loads to single layer or four layer fabric samples. At certain loads, the cell is paused and µCT-scans are taken. An example is shown in figure 4. On these µCT images, the distance between the compression cell clamps, h, can be measured, which allows for easy calculation

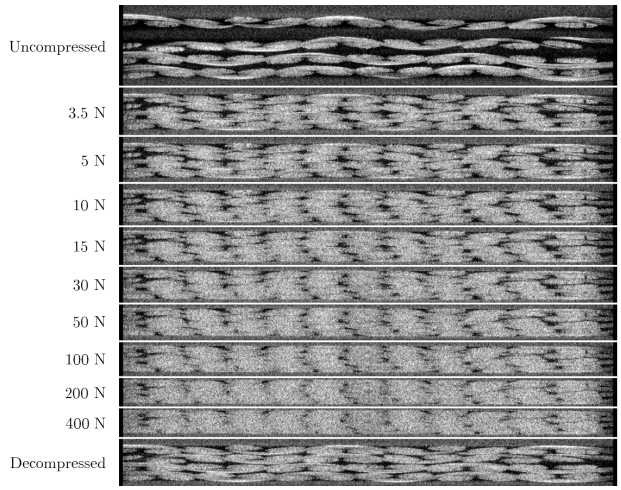

Fig. 4. µCT images of the four layer fabric sample during compression. A weft cross section is shown. Yarn flattening, void removal, yarn cross section deformation and nesting can all be observed.

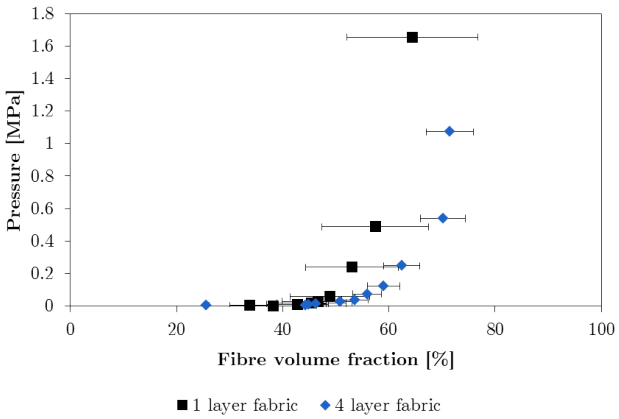

Fig. 5. Pressure-V_f plot of the compression experiment data for single layer and four layer fabric samples. The shape of the curve is in good agreement with the linear-exponential-linear consolidation behaviour reported in literature.

of the fibre volume fraction:

$$V_f = \frac{V_{fibres}}{V_{clamps}} \tag{5}$$

$$= \frac{A_{sample} \cdot \frac{\rho_A}{\rho_V}}{A_{sample} \cdot h} \tag{6}$$

$$= \frac{\rho_A}{\rho_V \cdot h} \tag{7}$$

V_{fibres} represents the volume taken up by the fibres, while V_{clamps} represents the total volume contained between the clamps of the Deben cell. A_{sample} is the average fabric area of each sample, and ρ_A and ρ_V are the areal and volumetric densities of the fabric, respectively. The Deben cell itself also returns the force F it applies at each point in time, which can be used to calculate the applied pressure P:

$$P = \frac{F}{A_{sample}} \tag{8}$$

Using these measurements, a pressure-V_f graph can be constructed to evaluate the consolidation behaviour; see figure 5. It is clear that this curve shows good agreement with the linear-exponential-linear consolidation behaviour reported in literature. Combining the µCT images with the graph shows that at low applied pressure, the yarns are moved into contact with the clamps and stage 1 consolidation occurs. Yarns are flattened and any crimp inequalities are balanced out. At higher pressures, stage 2 consolidation occurs: interyarn and interfibre voids are removed by fibre displacement, and the yarn cross sections are thus deformed. As the fibres start coming into contact with each other, interfibre friction provides an exponentially increasing resistance to displacement. Stage 3 consolidation occurs at the end of the experiment, when void removal and yarn slippage are at their limits. Further compaction is now only possible by elastic deformation of the fibres, explaining the very high increase in pressure for minimal increases in V_f. The four layer fabric displays higher V_f than the single layer fabric at equal pressures, mainly due to nesting. This can be seen in the decompression µCT image, and in the large hysteresis found between the uncompressed and decompressed states. Hysteresis always takes place, indicating that the deformation caused by compression is not fully elastic, but it is higher for the four layer fabric sample. The single layer fabric sample starts with a V_f of 33.72% while uncompressed and returns to a V_f of 38.15% after decompression, but for the four layer fabric sample these values are 25.56% and 44.30%, respectively.

B. Numerical compression

Consolidation behaviour is investigated numerically by subjecting the chosen truss-and-beam model to a compression simulation. To do this, the output nodes of the woven model are used as the input for a new simulation, and two rigid plates are added to either side of the fabric. These plates are then brought together (time step of 0.1 s), compressing the fabric between them, and subsequently separated an equal distance (time step 0.1 s) to simulate decompression. Each plate is displaced 0.18 mm, meaning a total compression of 0.36 mm is simulated. An example of the compression simulation is shown in figure 6. Again, yarn flattening and void removal are visible in this image, and yarn cross section deformation is very pronounced. An issue is encountered with warp and weft fibres migrating away from the centre of the fabric in opposite directions, but no solution has yet been found.

Images of the decompression step in the simulations show that yarns regain some of their former shape when pressure is lifted, but the fully relaxed fabric also remains more deformed and "disorganised", with fibres spread in between yarns. This confirms the hysteresis that is observed experimentally.

To gain numerical data, the reaction forces on the plate and the plate displacement are queried in ABAQUS. The reaction forces on the plates are equal (but opposite) to the forces exerted by the plates on the fabric, meaning they can be converted into the applied pressures via equation (8). The displacement of the plates can used to calculate their distance, h, as the original plate

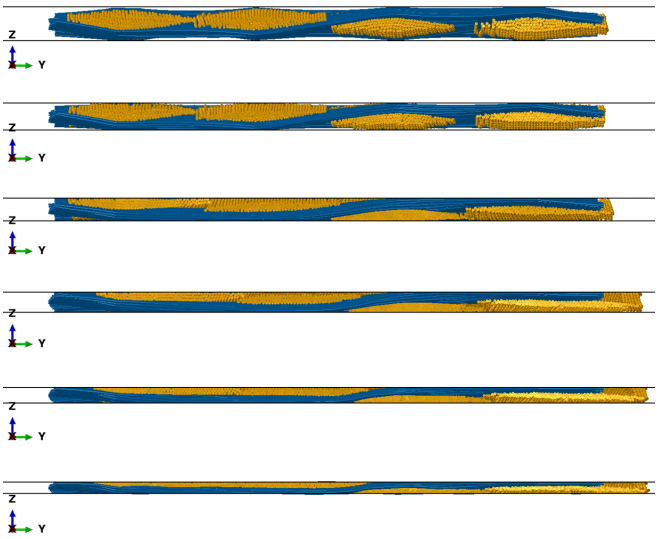

Fig. 6. A warp cross section of the compression simulation of the truss-and-beam model. The woven fabric (top) is deformed by two nearing rigid plates, until it reaches its final compressed state (bottom)

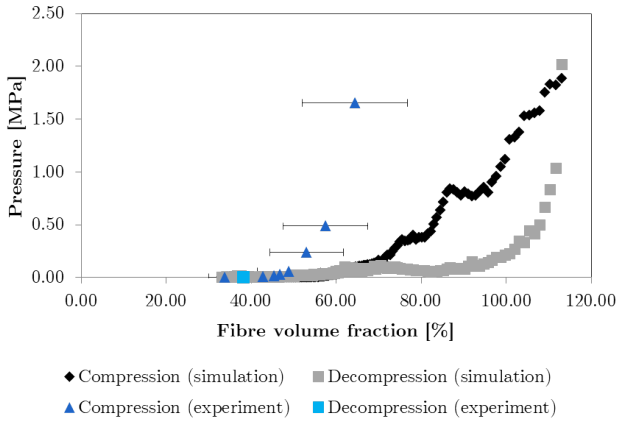

Fig. 7. Pressure-V_f plot of the compression/decompression simulation data for the truss-and-beam model, compared to the compression experiment data for the single layer fabric sample. The shape of the curve is in good agreement with the linear-exponential-linear consolidation behaviour reported in literature, but is shifted towards higher V_f.

distance before compression can be measured in ABAQUS. The distance between the plates can then be used to calculate V_f according to equation (7).

The pressure-V_f plot is given in figure 7. The shape of the curve is again found to agree with the linear-exponential-linear curve described in literature. This is an improvement of the truss-and-beam model over the truss-only model. However, when compared to the experimental results, it is clear that the curve is also shifted towards higher V_f, even reaching physically impossible V_f over 100%. The cause for this is a failure of the contact interactions between the truss elements in the model: at high levels of compression, the elements are found to clip into each other and beyond the rigid plates. A solution to this problem would likely require the definition of new contact interaction properties or boundary conditions.

VI. Conclusion

The goal of this study was to investigate consolidation behaviour of fabrics, and to create a finite element model that could simulate this behaviour accurately.

A novel, discrete meso-scale fabric model was constructed in the image of a 2/2 twill, E-glass, woven fabric. At the microscopic scale, fibres were designed by superimposing beam elements onto truss elements, in an effort to decouple the stiffness and flexural rigidity properties. The truss elements contributed to the stiffness and geometry of the material, while the beam elements' sole purpose was to contribute a flexural rigidity. These yarns were arranged in a hexagonal closed packing at the mesoscopic scale, and experimentally measured values were assigned to each element, ensuring correct dimensions and properties of the assembled yarns. At the macroscopic scale, the fabric was built by expanding on a truss-only model by Daelemans, superimposing beam elements on top of the existing truss elements. Deformation towards its as-woven state was realised by applying thermal shrinkage.

With the model constructed, the influence of several different parameters (number of fibres per yarn, coefficient of friction, time step and one- or two-stage weaving) on the deformation towards its as-woven state was investigated. From these results, the best model was chosen by comparison to experimental results gathered via µCT-scans. A combined truss-and-beam model with 127 fibres per yarn and a coefficient of friction of 0.10, deformed in a time step of 0.06 s via a two-stage weaving process was chosen.

Experimentally, consolidation behaviour was studied by carrying out a compression experiment on single layer and four layer fabric samples, and µCT-scanning the samples at certain pressures. This yielded a pressure-V_f curve that agreed well with the consolidation behaviour reported in literature. The µCT images showed yarn flattening, removal of voids and cross section deformation, as well as nesting in the case of the four layer fabric sample. Hysteresis was observed upon decompression, indicating that some of the compression deformation was inelastic in nature.

Numerically, consolidation behaviour was studied by subjecting the as-woven truss-and-beam model to a compression simulation. The fabric was surrounded by two rigid plates that were brought together and subsequently separated, modelling compression and decompression. From the reaction forces on these plates and their displacements, a pressure-V_f curve was again plotted. A similar shape of the curve was obtained as in the experimental investigation, but the curve was shifted towards much higher V_f due to contact interaction errors.

Despite the inaccuracies in the constructed truss-and-beam model, its improved bending behaviour as compared to the truss-only model (noted in the shape of its pressure-V_f curve, for example) acts as a proof of concept for the model. If the contact interaction and boundary condition issues can be solved, the potential for the model within the industry is great.

REFERENCES

[1] P. Potluri and T.V. Sagar, "Compaction modelling of textile preforms for composite structures" *Composite Structures* vol. 86, pp. 177-185, Mar 2008

[2] T. Grieser and P. Mitschang, "Investigation of the compaction behaviour of carbon fiber NCF for continuous preforming processes" *Polymer Composites* vol. 38, pp. 2609-2625, Nov 2017

[3] B. Chen and T. W, Chou, "Compaction of woven-fabric preforms in liquid composite molding processes: single-layer deformation" *Composites Science and Technology* vol. 59, pp. 1519-1526, 1999

[4] B. Chen and T. W, Chou, "Compaction of woven-fabric preforms: nesting and multi-layer deformation" *Composites Science and Technology* vol. 60, pp. 2223-2231, 2000

[5] R. A. Smith, "Composite defects and their detection" *Materials Science and Engineering* vol. 3, Jan 2009

[6] L. Daelemans, "Realistic numerical modelling of the yarn behaviour in the production of stitched sandwich panels" Master's thesis, Ghent University, May 2013

[7] G. Zhou, X. Sun and Y. Wang, "Digital-element simulation of textile processes" *Composites Science and Technology* vol. 61, pp. 311-319, 2001

[8] A. J. Thompson, B. El Said, D. Ivanov, J. P. H. Belnoue and S. R. Hallett, "High fidelity modelling of the compression behaviour of 2D woven fabrics" *International Journal of solids and Structures* vol. 154, pp. 104-113, 2018

Table of contents

Preface . . . . . **i**

Abstract . . . . . **iii**

Keywords iii

Extended abstract . . . . . **iv**

Table of contents . . . . . **x**

List of figures . . . . . **xiii**

List of tables . . . . . **xxiii**

1 Introduction **1**

1.1 The composite materials market 1

1.2 Composite consolidation 3

1.2.1 FRP manufacturing methods 3

1.2.2 Fabric consolidation behaviour 5

1.2.3 Defects introduced during consolidation 8

1.2.3.1 Porosity 8

1.2.3.2 Fibre waviness 9

1.3 Finite element modelling of fabrics 15

1.3.1 Macro-scale models 17

1.3.2 Meso-scale models 20

1.3.3 Micro-scale models 21

1.4 Goal and scope of this dissertation 22

2 Materials and methods **24**

2.1 Materials 24

2.1.1 Fabric . . . 24
2.1.2 Matrix material . . . 27
2.2 Methods . . . 27
2.2.1 Finite element analysis (FEA) . . . 27
2.2.1.1 Modelling and simulation . . . 27
2.2.1.2 Distance measurements . . . 28
2.2.2 Micro-computed tomography (µCT) . . . 29
2.2.2.1 Imaging . . . 29
2.2.2.2 Distance measurements . . . 29
2.2.3 Compression experiments . . . 31
2.2.3.1 Experiment 1: continuous loading . . . 31
2.2.3.2 Experiment 2: static loading . . . 34

3 Fabric model creation . . . 37
3.1 Fibre model (micro-scale) . . . 37
3.2 Yarn model (meso-scale) . . . 41
3.3 Fabric model (macro-scale) . . . 46
3.3.1 Existing truss fabric model . . . 46
3.3.2 New truss-and-beam fabric model . . . 48

4 Fabric model validation . . . 54
4.1 µCT image quality . . . 54
4.2 Influence of the model parameters . . . 57

5 Fabric consolidation . . . 73
5.1 Experimental compression . . . 73
5.1.1 Machine and image data . . . 73
5.1.2 Experimental compression results . . . 77
5.2 Numerical compression . . . 85
5.2.1 Compression simulation . . . 85
5.2.2 Numerical compression results . . . 90

6 Conclusion . . . 94
6.1 Summary . . . 94
6.2 Further research . . . 95

Bibliography **97**

Appendix A: Python code **110**

List of figures

1.1 A polymer matrix containing reinforcement materials. These reinforcement materials are most commonly long, continuous fibres (left) or short fibres (middle). Particulates (right) are a less common alternative that provide different properties [4]. 2

1.2 Several different composite manufacturing methods: wet hand lay-up (top left), vacuum assisted resin transfer moulding (VARTM) (top right), vacuum assisted resin infusion (VARI) (middle left), filament winding (middle right) and autoclave processing (bottom) [21]. In each process, the pressure applied during consolidation is marked by the blue arrows. 4

1.3 The mechanism behind the compaction of a single layer of woven fabric. In stage 1, any crimp inequalities are balanced out by removal of the gap δ, by flattening of the yarns. This is linearly related to the flexural rigidity of the yarns. In stage 2, voids between the individual fibres are removed, causing exponentially more interfibre friction as the fibres make contact with each other. In stage 3, the fibres are all touching and further compression is near impossible, requiring elastic deformation of the fibres themselves. This is linearly related to the transverse modulus of the fibres [22]. 7

1.4 A two-layer plain weave fabric before (left) and after (right) nesting. The total laminate thickness is reduced by a distance ${r_z}^{nesting}$ that is inherent to the fabric and is not affected by applied consolidation pressure [25]. 7

1.5 Two modes of failure facilitated by porosity in a composite: intralaminar fracture caused by the transverse stress exceeding the matrix' tensile strength, and interlaminar fracture (delamination) caused by interlaminar shear stresses exceeding the material's interlaminar shear strength (ILSS). The composite's fibre direction is aligned with the Y-axis [44]. 10

1.6 Fibre waviness in a composite sample. In-plane fibre waviness occurs when fibres bend within their designated lamina (left) and out-of-plane waviness or wrinkling occurs when fibres bend out of their designated lamina (right). . . 10
1.7 The mechanism behind out-of-plane fibre waviness upon consolidation over a curve. When the ply ends are unconstrained and the plies can slip over one another freely, the arc length reduction of the plies due to consolidation is compensated by in-plane compression or end-point extension (left). When the ply ends are constrained or the plies cannot slip over one another, the plies must buckle outwards to compensate for the arc length reduction (right) [48]. 12
1.8 The shear-induced wrinkling mechanism for woven or bi-axial non-crimp fabrics (NCFs). As the fabric is draped or consolidated over a curved geometry, its warp and weft yarns rigidly rotate towards one another, until they each a critical shear locking angle, after which continued rotation is physically blocked and the built-up shear and compressive forces are manifested as wrinkles [56]. 13
1.9 The maximum wrinkle angle (θ), wavelength (λ) and amplitude (h) of an out-of-plane waviness defect [70]. 13
1.10 Hierarchy of the multi-scale nature of fibrous material modelling [75]. 17
1.11 Triangular shell finite elements used in the continuous macro-scale model by Boisse et al. [80]. 18
1.12 Simulation of the continuous macro-scale model by Boisse et al. draping over a tetrahedron. [81]. 19
1.13 The truss-membrane discrete macro-scale model by Cherouat et al. (left) and the pantographic beam-membrane discrete macro-scale model by Harrison (right) [87]. 19
1.14 The discrete yarn model by Wang et al., made up of truss elements connected by frictionless pins at the nodes [97]. 21
1.15 The discrete meso-scale model by Chakladar et al., where yarns are constructed from 37 chains of beam elements. The upper and lower rigid bars are used for a compaction simulation [105]. 22

2.1 Pattern of a 2/2 twill weave, with a single, repeating unit cell marked within the red square [120]. 25
2.2 The E-glass fibre 2/2 twill fabric produced by P-D Interglas Technologies GmbH, used as a basis for the finite element model in this dissertation [119]. 25

2.3 The yarn width measuring process in ABAQUS/CAE. First, the deformed fabric is displayed and beam profiles are rendered (top left). All unnecessary fibres are then temporarily removed from view, in this case leaving only weft fibres displayed (top middle). Each yarn is measured at 5 equidistant points along its axis; this is achieved by free body cuts (top right). The yarn cross section is angled to see which fibres form the extrema, and the distance between them is measured by querying the distance between the frontmost nodes of each fibre, as indicated by the red dots (middle). The measured distance is read from the "Deformed distance" row and the column corresponding to the measuring direction, in this case along the X-axis, corresponding to "1" (bottom). 30
2.4 The yarn width measuring process in ImageJ. First, the reconstructed µCT image sequence is imported, revealing an XY cross section of the fabric. At this point the scale is set so that the voxel size is correct (top). A reslice is then taken, along one of the axes. This produces an XZ or a YZ cross section of the fabric, revealing the cross sections of the weft and warp yarns, respectively (middle). A straight line is drawn between the voxels on the extrema of the yarn cross sections, as indicated by the yellow line, and the length of the line is queried (bottom). 32
2.5 The Deben CT5000-TEC cell, mounted on the HECTOR tomograph [130]. . 33
2.6 The steel squares used to create a top mould for the static loading experiment. Via grinding, the smallest square was ensured to be the correct size and have a flat surface (left). These squares were glued to each other to make the mould (right). 35
2.7 Experimental setup to create the composite samples under static loading. The mass of the weight was varied to achieve different load pressures. The composite consisted of 1 or 4 layers of glass fibre fabric embedded in resin. The glass plate and mould were treated with release agent or covered in release foil so as not to stick to the resin. 36

3.1 A fibre model consisting of structural truss or beam elements, sequentially connected by single-point nodes along the centre line [75]. 38

3.2 The setup for a digital experiment to visualise the difference in bending behaviour in fibres made of truss elements and those made of beam elements [75]. 39
3.3 The bending behaviour of a fibre made of truss elements (left) and beam elements (right). It is clear that trusses do not provide realistic bending behaviour because they do not transmit bending moments between nodes. Beam elements bend accurately. 40
3.4 The difference between idealised closed packing and more realistic open packing for the assembly of fibres in a yarn model [75]. 43
3.5 The setup of a Peirce cantilever test. A fabric sample is laid on top of a flat surface and gradually slid forward until its free edge bends down to reach a line θ° (usually 41.5°) below the top surface. The overhanging length l is then measured [134]. 46
3.6 Slave yarns inserted along the edges of a fabric unit cell to ensure periodicity. Each slave yarn is a copy of the master yarn on the opposite side of the unit cell and is tied to that master yarn via multi-point coinstraints (MPCs) in each corresponding node [107]. 48
3.7 The basic truss fabric model (61 fibres per yarn) by Daelemans in its undeformed, loose topology state. The warp yarns (X-direction) are yellow, the weft yarns (Y-direction) are blue. The green and red slave yarns have an artificially reduced Young's modulus. 49
3.8 The basic truss fabric model (61 fibres per yarn) by Daelemans in its deformed, as-woven state. The warp yarns (X-direction) are yellow, the weft yarns (Y-direction) are blue. The green and red slave yarns have an artificially reduced Young's modulus. 50
3.9 The combined truss-and-beam fabric model (127 fibres per yarn) in its undeformed state (top) and its as-woven state (bottom). The truss elements, representing the real fabric geometry, are yellow in the warp direction (X-direction) and blue in the weft direction (Y-direction) (right). The beam elements, only contributing their flexural rigidity, are made from the same material as the slave yarns with an artificially reduced Young's modulus and are coloured green in the warp direction (X-direction) and red in the weft direction (Y-direction) (left). 52

3.10 The combined truss-and-beam fabric model (61 fibres per yarn) with oversized beam elements in its undeformed state (top) and its as-woven state (bottom). The truss elements are coloured yellow and blue (right) while the beam elements are coloured green and red (left). It is clear that the beams contribute to the flexural rigidity of the fabric because the as-woven state is much looser but at the same time do not constrict node movement through contact interactions. 53

4.1 A comparison of the µCT images of single layers of glass fibre fabric. Previous scans at the UGCT provided images with very high resolution, where every fibre is visualised individually, even if the contrast is low (top/left). Scans of experiment 1 showed very low resolution and high amounts of noise (middle/middle). Scans of experiment 2 had a better resolution and contrast with the matrix material, but lower contrast between yarns and almost equally much noise (bottom/right). 56

4.2 The influence of the coefficient of friction on warp (top) and weft (bottom) yarn width in the truss-and-beam model with 61 fibres per yarn. The time step for weaving is set at 0.040 s and the two-stage weaving process is used. Note that the X-axes do not start at 0 mm. The bars shown encompass the average yarn width and one standard deviation along either side. 58

4.3 The influence of the coefficient of friction on warp (top) and weft (bottom) yarn width in the truss-and-beam model with 91 fibres per yarn. The time step for weaving is set at 0.040 s and the two-stage weaving process is used. Note that the X-axes do not start at 0 mm. The bars shown encompass the average yarn width and one standard deviation along either side. 59

4.4 The influence of the coefficient of friction on warp (top) and weft (bottom) yarn width in the truss-and-beam model with 127 fibres per yarn. The time step for weaving is set at 0.040 s and and the two-stage weaving process is used. Note that the X-axes do not start at 0 mm. The bars shown encompass the average yarn width and one standard deviation along either side. 60

4.5 The influence of the time step on warp (top) and weft (bottom) yarn width in the truss-and-beam model with 61 fibres per yarn. The coefficient of friction is set at 0.00 and the two-stage weaving process is used. Note that the X-axes do not start at 0 mm. The bars shown encompass the average yarn width and one standard deviation along either side. 62
4.6 The influence of the time step on warp (top) and weft (bottom) yarn width in the truss-and-beam model with 127 fibres per yarn. The coefficient of friction is set at 0.10 and the two-stage weaving process is used. Note that the X-axes do not start at 0 mm. The bars shown encompass the average yarn width and one standard deviation along either side. 63
4.7 Energy balance for the weaving process of the truss-only model with 61 fibres per yarn, a time step of 0.04 s, a coefficient of friction of 0.15 and a two-stage weaving process (top), and the truss-and-beam model with the same parameters (bottom). The truss model is clearly quasi-static, as the internal energy is always higher than the kinetic energy. The truss-and-beam model remains mostly quasi-static, but becomes less stable towards the end of the simulation. 64
4.8 Energy balance for the weaving process of the truss-and-beam model with 127 fibres per yarn, a time step of 0.1 s, a coefficient of friction of 0.10 and a one-stage weaving process (top), and the same model with a two-stage weaving process (bottom). The one-stage weaving simulation is clearly quasi-static, as the internal energy is always higher than the kinetic energy. The two-stage weaving simulation behaves oppositely, becoming highly dynamic and more unstable at high time steps. 66
4.9 The influence of the one- or two-stage weaving process on warp (top) and weft (bottom) yarn width in the truss-and-beam model with 127 fibres per yarn. The coefficient of friction is set at 0.10. Note that the X-axes do not start at 0 mm. The bars shown encompass the average yarn width and one standard deviation along either side. 67
4.10 Validation of the truss-and-beam model with 127 fibres per yarn, a coefficient of friction of 0.10 and a two-stage loading process (relaxation allowed) via comparison of its warp (top) and weft (bottom) yarn heights with experimental data. Note that the X-axes do not start at 0 mm. The bars shown encompass the average yarn width and one standard deviation along either side. 68

4.11 An XY-view of the final truss-and-beam model with 127 fibres per yarn and a coefficient of friction of 0.10, deformed from its loose topology state (top left) to its as-woven state (bottom right) in a time step of 0.06 s via a two-stage weaving process. Only the truss elements are shown, as they represent the fabric geometry. These are yellow in the warp direction (X-direction) and blue in the weft direction (Y-direction). Note the relaxation occurring between the last two images. 70
4.12 An XZ-view of the final truss-and-beam model with 127 fibres per yarn and a coefficient of friction of 0.10, deformed from its loose topology state (top left) to its as-woven state (bottom right) in a time step of 0.06 s via a two-stage weaving process. Only the truss elements are shown, as they represent the fabric geometry. These are yellow in the warp direction (X-direction) and blue in the weft direction (Y-direction). Note the relaxation occurring in the last two images. 71
4.13 A YZ-view of the final as-woven truss-and-beam model with 127 fibres per yarn and a coefficient of friction of 0.10, deformed in a time step of 0.06 s via a two-stage weaving process. The cross sections of the warp yarns (yellow) are shown and compared to cross sections of warp yarns imaged via µCT-scanning in experiment 1 (middle) and experiment 2 (bottom). 72
4.14 An XZ-view of the final as-woven truss-and-beam model with 127 fibres per yarn and a coefficient of friction of 0.10, deformed in a time step of 0.06 s via a two-stage weaving process. The cross sections of the weft yarns (blue) are shown and compared to cross sections of weft yarns imaged via µCT-scanning in experiment 1 (middle) and experiment 2 (bottom). 72

5.1 Calibration curves to evaluate the compliance of the polyether ether ketone (PEEK) jaws used to apply pressure in experiment 1. The compliance is equal to the slope of the linear elastic regions in the displacement-force curve (top). These regions can be described with a Young's modulus, found similarly as the slope in the stress-strain curve (bottom). Linear elastic behaviour was expected, but two regions with differing Young's moduli were not. Additionally, the moduli are much lower than the reported value for PEEK. 76

5.2 Plots of the pressure versus the fibre volume fraction (V_f) for the single layer fabric sample (top) and the four layer fabric sample (bottom), after corrections were applied to the machine data. The machine data still differs from the image data, though they should be the same. The shape of the curves is in good agreement with the linear-exponential-linear consolidation curve observed in literature. 78
5.3 Plots of the clamp distance as gathered from the image data versus the machine data, for the single layer fabric sample (top) and the four layer fabric sample (bottom). While clearly correlated, both values are not identical: the slopes of the trendlines should be 1. 79
5.4 Plot of the pressure versus the V_f for the µCT image data of the single layer and the four layer fabric samples. The shape of the curves is in good agreement with the linear-exponential-linear consolidation curve observed in literature. The four layer fabric sample seems to have a higher V_f at equal stress, indicating a larger thickness reduction took place, which can be ascribed to more crimp balance, a higher void content before compression, and nesting. 80
5.5 µCT images of the single layer fabric sample during compression. The XZ section shows the cross section of the weft yarns (top), while the YZ section shows the cross section of the warp yarns (bottom). Yarn flattening, void removal and minor yarn cross section deformation can be observed. 82
5.6 µCT images of the four layer fabric sample during compression. The XZ section shows the cross section of the weft yarns (top), while the YZ section shows the cross section of the warp yarns (bottom). Yarn flattening, void removal and minor yarn cross section deformation can be observed. From the decompressed image, it is clear that nesting has taken place. 83
5.7 Experimental weft (top) and warp (bottom) yarn width measurements of the single layer fabric sample under increasing compression. The error margins are large due to the low µCT image quality, so no statistically significant results can be obtained. Note that the X-axes do not start at 0 mm. The bars shown encompass the average yarn width and one standard deviation along either side. The anomalous measurement at 10 N should be discounted. 84

5.8 A YZ-view of the compression simulation of the truss-and-beam model. The as-woven fabric (top) is deformed by the nearing of two rigid plates, until it reaches its final compressed state (bottom). The plates are displaced by 0.18 mm each, in a time step of 0.1 s. Only the truss elements are shown, as they represent the fabric geometry. These are yellow in the warp direction (X-direction) and blue in the weft direction (Y-direction). Note that the warp and weft yarns seem to migrate away from each other in the Y-direction. . . 86
5.9 An XZ-view of the compression simulation of the truss-and-beam model. The as-woven fabric (top) is deformed by the nearing of two rigid plates, until it reaches its final compressed state (bottom). The plates are displaced by 0.18 mm each, in a time step of 0.1 s. Only the truss elements are shown, as they represent the fabric geometry. These are yellow in the warp direction (X-direction) and blue in the weft direction (Y-direction). 87
5.10 A YZ-view of the decompression simulation of the truss-and-beam model. The fully compressed fabric (top) is allowed to relax by the separating of two rigid plates, until it reaches its final relaxed state (bottom). The plates are displaced by 0.18 mm each, in a time step of 0.1 s. Only the truss elements are shown, as they represent the fabric geometry. These are yellow in the warp direction (X-direction) and blue in the weft direction (Y-direction). Note that the warp and weft yarns seem to migrate away from each other in the Y-direction. . . 88
5.11 An XZ-view of the decompression simulation of the truss-and-beam model. The fully compressed fabric (top) is allowed to relax by the separating of two rigid plates, until it reaches its final relaxed state (bottom). The plates are displaced by 0.18 mm each, in a time step of 0.1 s. Only the truss elements are shown, as they represent the fabric geometry. These are yellow in the warp direction (X-direction) and blue in the weft direction (Y-direction). Note that the warp and weft yarns seem to migrate away from each other in the X-direction. 89
5.12 Energy balance for the compression/decompression simulation of the truss-and-beam model in a total time step of 0.2 s. Both loading steps in the simulation are clearly quasi-static, as the internal energy is always higher than the kinetic energy. 90

5.13 Plot of the pressure versus the V_f for the numerical compression/decompression simulation of the truss-and-beam model, compared to the experimental results of the single layer fabric sample from experiment 1. The shape of the simulation curves is in good agreement with the experimental linear-exponential-linear consolidation curve, but it is shifted towards higher V_f. 93

5.14 A zoomed in YZ-view of fully compressed truss-and-beam models, at a compression of 0.284 mm (top) and 0.36 mm (bottom). The smaller compression seems to cause few contact problems, but the larger compression results in clipping of the fibres within each other and beyond the plates. . . . 93

List of tables

2.1 Relevant properties of the glass fibre fabric material used in this dissertation, either supplied by the manufacturer or experimentally determined. 27
2.2 The masses (and their respective exerted pressures) placed on top of the composite samples, to provide static loading during curing. 35

3.1 The cross sectional area each virtual fibre needs to have to accurately represent real fibres without having as many fibres per yarn. These cross sectional areas define the size of the truss elements in the yarn model. 44
3.2 The flexural rigidity of the real yarns in both warp and weft directions, and the corresponding radii that the virtual beam elements need to have to accurately represent the real flexural rigidity if their Young's modulus is artificially reduced by a factor 100. 46

Chapter 1

Introduction

1.1 The composite materials market

Composites are heterogeneous materials consisting of clearly distinguishable phases, usually created to combine the properties of their constituent materials - emphasizing good properties, diminishing the effect of lesser properties or generating new properties altogether [1].

Man-made composite materials have been designed throughout human history, spanning as far back as the Indus Valley Civilisation around 7000 B.C., where huts were built using mud bricks reinforced with straw [2]. While better construction materials have since been developed to replace these mud bricks - including composite materials such as (steel reinforced) concrete - other composite materials remain current, such as paper, invented in China around 105 B.C. [3]. In the current day and age, the term "composites" - as used in the structural materials market - most commonly refers to FRPs. These consist of reinforcing fibres embedded into a polymer matrix; see figure 1.1. Each vertical layer of embedded fibres forms a lamina, and the stack of laminae form the composite as a whole. Within each lamina, the fibres can be aligned in a certain direction, oriented randomly or woven as a fabric.

The fibres predominantly determine the stiffness of the combined material and act as the principal load-bearing constituent, while hindering matrix crack propagation [1]. The two dominant reinforcing fibres used in the FRP market are glass fibres and carbon fibres, with polymer fibres (e.g. aramid, ultra high molecular weight polyethylene (UHMWPE), flax) and metallic fibres (e.g. steel, aluminium, titanium) representing a smaller portion of the market. The matrix, on the other hand, encases the fibres to keep them in their intended position

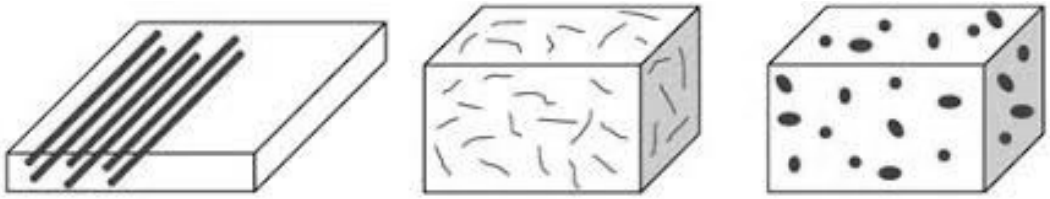

Figure 1.1: A polymer matrix containing reinforcement materials. These reinforcement materials are most commonly long, continuous fibres (left) or short fibres (middle). Particulates (right) are a less common alternative that provide different properties [4].

and protect them from the environment, while also being responsible for the transmission of external loads onto the fibres, increasing material toughness and reducing fibre fracture [1]. Polymer matrices are split into thermosets (e.g. polyesters, vinylesters, epoxies, phenolics, polyimides) and thermoplastics (e.g. polyethylene, polypropylene, polyamide, polysulphone, polyphenylene, sulphide, polyether sulphone, PEEK), each with different properties [1]. More niche applications sometimes require non-polymeric matrices to form general fibre reinforced composites (FRCs). Metals (e.g. steel), for example, may be used for their electrical and heat conductivity, and ceramics (e.g. glass, carbon) may be used for their heat resistance and insulation [1].

The main advantage of FRPs is their high specific stiffness and strength - the ratio of these properties to their mass. In the construction sector, this opens up design options for architecturally creative buildings without heavy foundations and facilitates quick construction times [1]. In the wind energy sector - one of the most important for FRPs [5] - the specific stiffness and strength of glass fibre reinforced polymers (GFRPs) are required to produce large turbine blades, as any metallic turbine blades would buckle under their own weight. The low structural mass provides the most significant benefit in the transport sector, however, making it the largest market for FRPs, with a market share of 33% [5]. The use of composite materials in this sector notably started in the aeronautical and aerospace industry, where any mass reduction in aircraft, satellites, rockets, etc. leads to increased fuel efficiency and thus reduced costs and a lower environmental impact [6, 7, 8]. In the last decade, the automotive industry has also taken a keen interest in composite materials, especially in carbon fibre reinforced polymers (CFRPs), for the same reasons [9, 10, 11]. It has been calculated that a reduction in automobile mass of 10% leads to a decrease in fuel consumption of 6-8%, which makes lighter materials close to necessary to adhere to ever-tightening automotive emission standards [12, 13].

A second benefit FRPs have over competing materials is their corrosion and chemical resistance, which leads to high demand in the pipe and tank industry [14, 15], and generally low maintenance in all applications [1]. Similarly, their flame retardant properties and tunable electrical conductivity/resistivity encourage FRP use in the electrical and electronics industry [16, 17].

Thanks to all these major industrial drivers, the worldwide composite materials market is continuously growing. To illustrate this, consider that the Airbus A350 (launched in 2013) is composed of FRP parts for 55% by mass, or almost 80% by volume, while its predecessor, the A380 (launched in 2005), consists of only 20% FRP by mass [1]. Lucintel estimates that by 2024, the intermediate materials market (for FRC parts) will reach €36 billion, while the end product market is expected to reach €102.8 billion [18].

1.2 Composite consolidation

1.2.1 FRP manufacturing methods

With a market this size, it is clear that the industrial production of composite parts needs to be efficient. This is achieved by having many different manufacturing methods available, each more suited to the production of specific parts than the rest. Wet hand lay-up or spray-up techniques require only minimal investment and as such are suited to small production series, for example. Resin infusion techniques such as vacuum assisted resin transfer moulding (VARTM) can create larger shapes with consistent mechanical properties and two finished surfaces, while autoclave processes can create composites with even better mechanical properties at a high investment cost [1]. Pultrusion, filament winding, tape laying, injection moulding and compression moulding round off the list of common, industrial composite manufacturing methods.

While it is outside the scope of this dissertation to delve into the specifics of each manufacturing method, one thing all methods have in common - with the exception of 3D-printing which is still in its development and upscaling stage [19] - is that, at some point during the process (this can be before or after impregnation with the matrix material), the reinforcement fibres are submitted to an external pressure and are thus compressed; see figure 1.2. This is called the consolidation stage of the process.

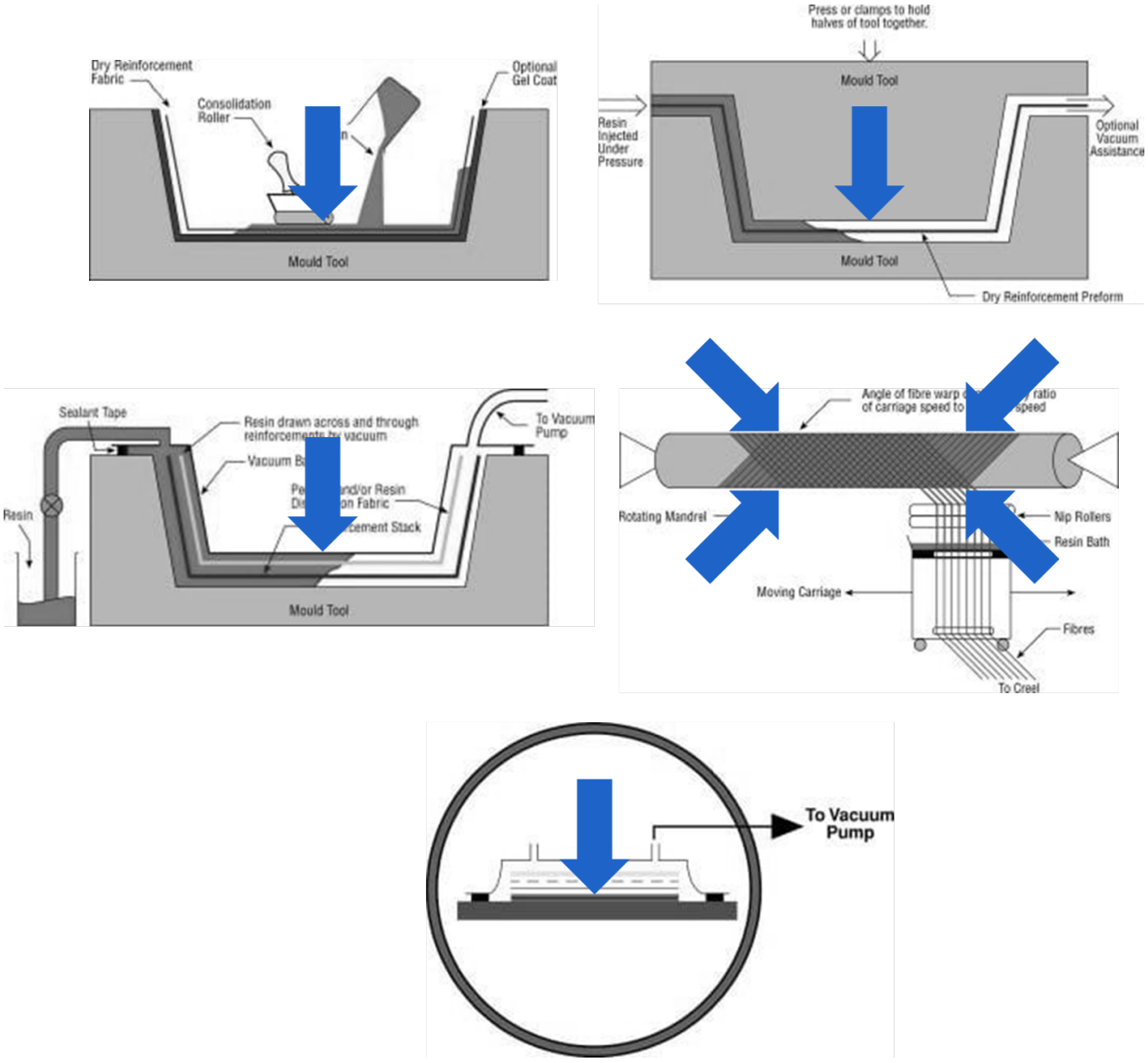

Figure 1.2: Several different composite manufacturing methods: wet hand lay-up (top left), VARTM (top right), VARI (middle left), filament winding (middle right) and autoclave processing (bottom) [21]. In each process, the pressure applied during consolidation is marked by the blue arrows.

1.2.2 Fabric consolidation behaviour

The goal of the consolidation stage is to increase the composite's V_f. This is defined as the volume the fibres take up in the entire volume of the composite, and is often expressed as a percentage:

$$\begin{aligned} V_f &= \frac{V_{fibres}}{V_{composite}} \\ &= \frac{V_{fibres}}{V_{fibres} + V_{matrix} + V_{voids}} \\ &= \frac{V_{fibres}}{V_{fibres} + V_{matrix} + V_{voids}} \cdot 100\% \end{aligned}$$

V_{fibres}, V_{matrix} and V_{voids} are the absolute volumes of the fibres, the matrix and any voids in the composite, respectively. As pressure is increased during a consolidation stage, the fibres are pushed together and matrix material is pushed away, increasing the V_f. This is why a wet hand lay-up method, where pressure is applied to the fibres by hand, produces parts with lower V_f than a vacuum assisted resin infusion (VARI) method, where atmospheric pressure is applied. The highest V_f can be reached via autoclave processes, where external pressures can exceed 7 bar [20].

A composite's V_f is one of the main parameters that influence its material properties [1]. As V_f increases, the amount of fibres embedded in the composite increases, providing strength and stiffness, but the amount of matrix material capable of taking up global deformation decreases. As such, every FRC product aims towards a certain V_f. Generally, high-end applications require high strength and stiffness, and thus desire a higher V_f.

While the compaction behaviour of a fabric depends on several parameters (compaction speed, number of compaction cycles, number of fabric layers, stacking sequence, etc.), the actual mechanism behind fabric compaction is always similar. As can be seen in figure 1.3, there are three global stages. In stage 1, the perpendicularly applied compressive force acts on the highest and lowest points of the fabric, flattening the yarns until any gaps in their thickness direction (δ) are removed. This means one set of yarns receives an increase in curvature while the other receives a corresponding decrease in curvature, which is why the process is termed "crimp balance" (crimp describes the undulation of the fibres). This thickness reduction is linear with increasing pressure as it depends solely on the

flexural rigidity of the yarns. As this is generally quite low, large thickness reductions are possible. Note that these gaps are a symptom of the weaving process: woven fabrics generally have unequal crimp in warp and weft directions. Since NCFs do not display this geometry, they are not affected by crimp balance. In stage 2, the individual fibres within the yarns are compressed together, removing voids between them and thus deforming the yarn cross-sections. The thickness reduction is now no longer linear but rather exponential with the applied pressure, as the fibres start interacting with each other and interfibre friction starts influencing the equation. At this point, a much larger surface area of the fabric is uniformly in contact with the plate providing the consolidation pressure. When the removal of voids and the slipping of fibres reach their limits, stage 3 is reached. In this stage, further compression is almost impossible, requiring elastic deformation at the fibre level itself, which is linearly related to the transverse modulus of the fibres. This serves as a physical limit to the V_f obtainable through compression [22, 23, 24].

When multiple layers of fabric are stacked on top of each other before consolidation (as is almost always the case with FRCs), a secondary phenomenon can take place: nesting. This is where the layers slide into each other under influence of compression, as in figure 1.4. The "hills" and "valleys" of adjacent layers will thus align more, reducing the total thickness of the stacked fabrics by a certain value, as compared to the non-nesting situation. This value is not dependent on the applied external pressure, only on the fabric geometry and material properties. Note that nesting has an immediate effect in woven fabrics and unidirectional NCFs: it contributes to thickness reduction of the plies from stage 1 of the aforementioned mechanism [23, 25, 26]. The thickness of each layer is reduced by increased nesting as the amount of layers in a stack is increased - until a critical limit. Chen et al. determined that for a glass fibre fabric, that limit was 10 plies: the thickness of each ply did not reduce further due to nesting from 10 to 25 plies. The total thickness reduction due to nesting was found to be 15% for two plies and up to 29% for any ply number above 10. [26]. Saunders et al. identified the steady state starting at 5 plies, for a plain weave glass fibre fabric [27].

Upon release of the consolidation pressure, much of the deformation is returned. Stage 3 is completely inverted as all deformation there (if any) is fully elastic, but the fabric as a whole does not return to its original, uncompressed state. This is because macroscopic deformations such as void removal, fibre entanglement and nesting can all be permanent. According to Grieser et al., if the fabric is held under pressure before decompression, the fibres get more time to realign and thus invert less, which results in higher V_f [23].

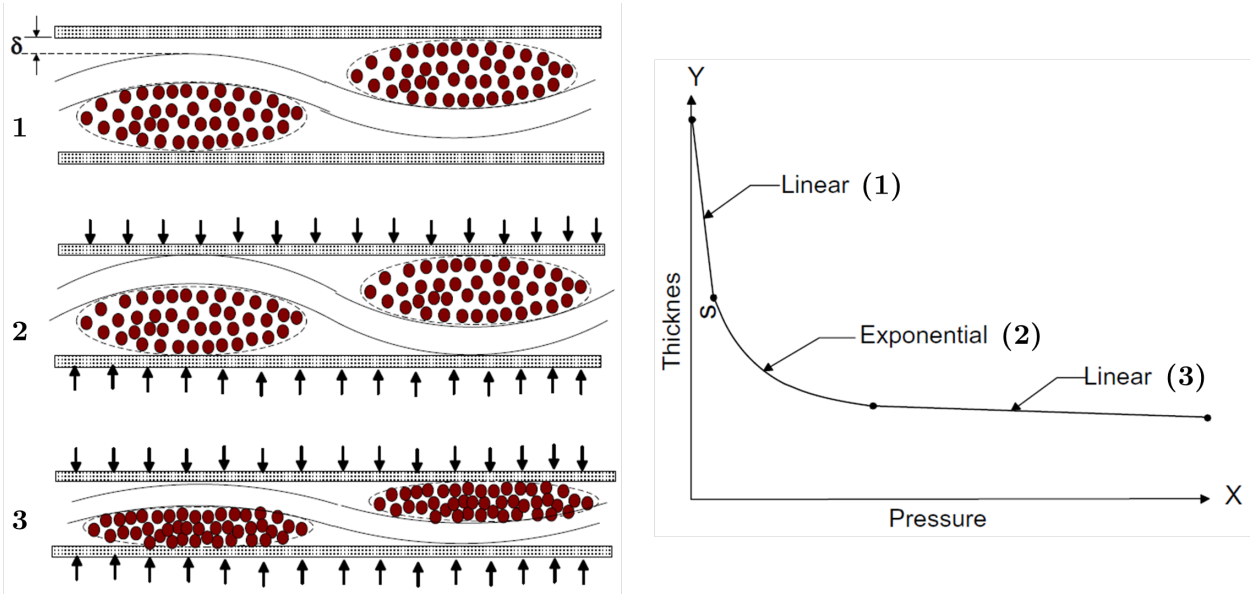

Figure 1.3: The mechanism behind the compaction of a single layer of woven fabric. In stage 1, any crimp inequalities are balanced out by removal of the gap δ, by flattening of the yarns. This is linearly related to the flexural rigidity of the yarns. In stage 2, voids between the individual fibres are removed, causing exponentially more interfibre friction as the fibres make contact with each other. In stage 3, the fibres are all touching and further compression is near impossible, requiring elastic deformation of the fibres themselves. This is linearly related to the transverse modulus of the fibres [22].

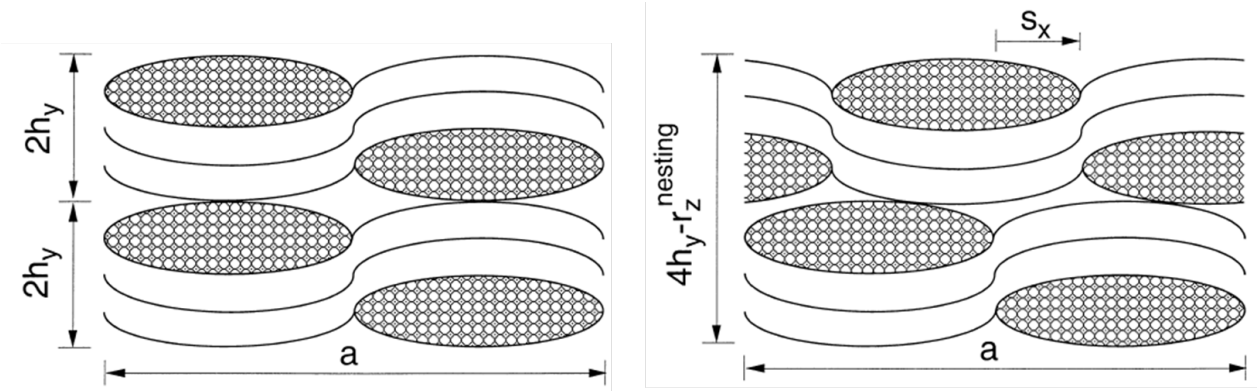

Figure 1.4: A two-layer plain weave fabric before (left) and after (right) nesting. The total laminate thickness is reduced by a distance $r_z{}^{nesting}$ that is inherent to the fabric and is not affected by applied consolidation pressure [25].

1.2.3 Defects introduced during consolidation

While the pressure applied during consolidation is necessary to reach the required V_f, it can simultaneously lead to the introduction of defects in the composite part. These differ from defects created during the composite's lifetime because they often prevent the part from ever entering service and as such, lead to completely wasted materials or expensive and time-consuming repair processes. Beside not reaching the correct V_f, the two main defects produced by compression during consolidation are porosity and fibre waviness [28].

1.2.3.1 Porosity

Porosity is the term used for the presence of small voids in the matrix. These voids are created by air bubbles or volatile compounds being trapped within the composite before the curing stage, which is the result of insufficient matrix material being used or incorrect curing parameters. Of the latter, pressure is just one component (the others being temperature, duration, vacuum bleeding, etc. [28]), but it contributes heavily and as such, specific pressures have even been used in autoclave tests to purposefully induce porosity for research purposes, from 0.3 vol% to 40 vol% [29, 30, 31, 32]. Liu et al. discovered that it is not only the volume fraction of voids that is dependent upon the applied pressure, but also the location, distribution, shape and size of individual voids [29]. Irregularly shaped voids or voids at critical locations can be more dangerous than the sheer volume of voids in general, for example due to a higher chance of causing crack initiation [33, 34].

While porosity is always accompanied by a loss of mechanical properties, this deterioration is not isotropic [33, 35]. As porosity affects the matrix and does not affect the integrity of the fibres or their alignment, the in-plane effects of porosity in the fibre direction (along the axis of the fibres) are minimal [30]. In composites with uni-directionally aligned fibres, however, this means a large detrimental effect can be observed in the transverse direction, orthogonal to the fibre direction. Voids that facilitate crack initiation under transverse stress can lead to intralaminar fracture along the fibres; see figure 1.5. The material properties that are affected by the void content are those that are matrix-dominated instead of fibre-dominated, i.e. compressive modulus and strength, in-plane and interlaminar shear properties, and fatigue life [32, 33, 36]. Demma et al. state that any observed effects depend on the reduction in matrix material at a macro-scale, or the local reduction in fibre-matrix contact or crack initiation at a micro-scale [37].

The material property most severely affected by porosity is interlaminar shear strength (ILSS). This is a measure for the composite's ability to endure out-of-plane shear stresses between laminae, which can exist even in pure in-plane loading, due to the binding together of layers with anisotropic properties. One layer can force Poisson contraction upon another layer, for example, while that layer will in turn hinder Poisson contraction of the first layer, causing stress throughout the thickness of the material [1]. When interlaminar shear stresses exceed the ILSS, this causes interlaminar fracture or delamination (a separation of the laminae); see figure 1.5. According to Mohite, this is the prevalent lifespan-limiting damage composite materials accrue [38]. Siver and Ghiorse reported similar results: an increase in porosity of 1% in carbon fibre/epoxy systems was found to decrease ILSS by 9-9.7% [30, 39].

Concerning the effect of porosity on compressive strength, results in literature vary strongly. Suarez et al. have observed reductions in compressive strength of 40% for void volume fractions of just 4% [40], but Cinquin et al. later found that a void volume fraction of 11% in the same CFRP material only corresponded to a reduction in compressive strength of 14% [41].

The opposite is true for flexural measurements - results have always been consistent: Both Olivier et al. and Almeida et al. describe CFRPs losing approximately 20% of their flexural modulus and 28% of their flexural strength for a void volume fraction of 14% [32, 42].

Fatigue life was also found to decrease with increasing void content by Almeida et al., but only if the volume fraction of voids is above 2% [42]. Chambers et al. reported that increasing the void volume fraction from 2% to 3.1% in a CFRP, resulted in a severe fatigue life drop from 2000 cycles to 106 cycles [43].

1.2.3.2 Fibre waviness

Fibre waviness is the phenomenon that occurs when fibres within a FRC are not aligned as intended because of fibre bending. This can be split up into two types of defect: in-plane waviness, which occurs when fibres bend two dimensionally, within the lamina, and out-of-plane waviness (better known as wrinkling), which occurs when fibres bend three dimensionally, out of the lamina; see figure 1.6.

In-plane fibre waviness is a difficult defect to detect: it cannot be visualised via ultrasonic inspection - the most commonly used inspection technique during composite manufacturing -

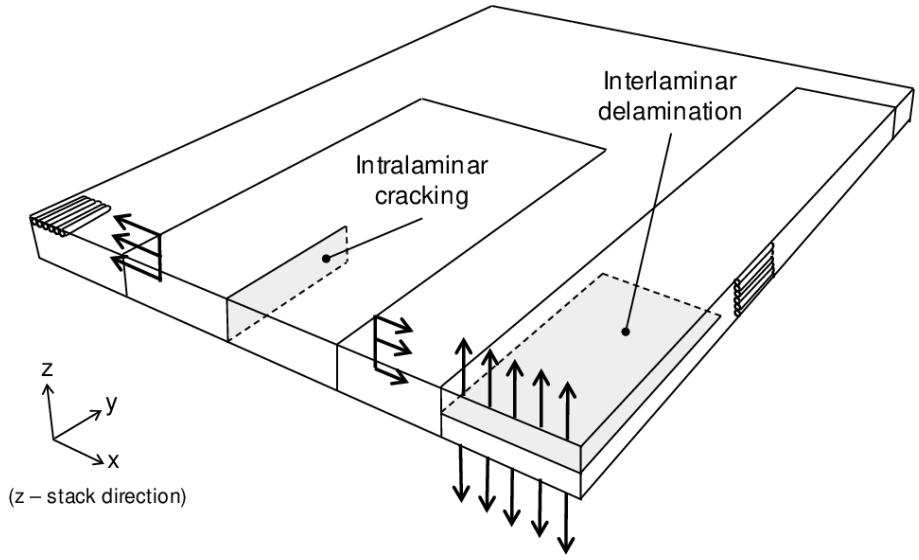

Figure 1.5: Two modes of failure facilitated by porosity in a composite: intralaminar fracture caused by the transverse stress exceeding the matrix' tensile strength, and interlaminar fracture (delamination) caused by interlaminar shear stresses exceeding the material's ILSS. The composite's fibre direction is aligned with the Y-axis [44].

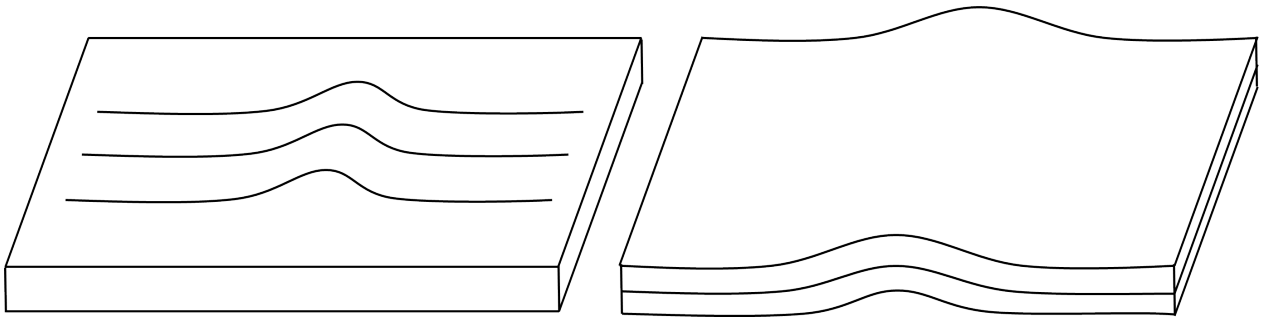

Figure 1.6: Fibre waviness in a composite sample. In-plane fibre waviness occurs when fibres bend within their designated lamina (left) and out-of-plane waviness or wrinkling occurs when fibres bend out of their designated lamina (right).

and methods to detect it, such as micro-computed tomography (µCT), are not feasible for large structures [45]. At the same time, in-plane waviness leads to matrix-rich areas within a lamina, unsupported by reinforcing fibres, which in turn lead to high stress concentrations and decreases in local mechanical strength, possibly culminating in delaminations [46]. While this difficulty of detection and the substantial effects on material properties make in-plane fibre waviness a dangerous defect, Kugler and Moon determined that it is not affected by consolidation pressure. Only sample length, cooling rate and mould material affect the introduction of in-plane fibre waviness and as such, it falls outside the scope of this dissertation [47].

Out-of-plane fibre waviness is a different matter. The main mechanism behind wrinkle formation during consolidation is outlined in figure 1.7. When a composite is compressed over a curve, its thickness is reduced, meaning the outer ply moves towards the centre of the curve. The radius of the curve is smaller there, so its arc length decreases. The physical length of the ply cannot simply disappear, however, so the ply must compensate. It does this by in-plane compression or by extending its length at the edges, creating the so-called book-end effect. In practice, neither of these compensations can often take place: if the length change is applied along a fibre direction, this direction is virtually inextensible and so cannot compress. If the ply has constrained ends (as most moulds will enforce) or the composite generally does not allow interply slip (due to high interply friction, for example), the book-end effect cannot occur. The only option left then, to the ply, is to buckle out of its plane, creating the wrinkle. Each ply under the outer layer follows the same course of action, with a diminishing length difference as the innermost ply is neared [48, 49, 50, 51].

This wrinkling is determined by several key parameters during the consolidation process: laminate thickness [45, 48, 49, 52, 53], ply stacking sequence [49], fibre tensile stiffness and flexural rigidity [49, 54], consolidation temperature [45], mould geometry [45, 49, 52, 53], and - most importantly - interply friction [45, 48, 49], which is in turn affected by the consolidation pressure. This pressure simultaneously drives and restricts the interply slip, and to reach an optimum V_f, it must be balanced with other consolidation parameters such as temperature and rate [55].

For FRCs made from woven fabrics or biaxial NCFs, there is one other important wrinkling mechanism, shown in figure 1.8. When the fabric is draped or consolidated over a geometry such as a double curved surface (e.g. a hemisphere or a tetrahedron), the warp and weft

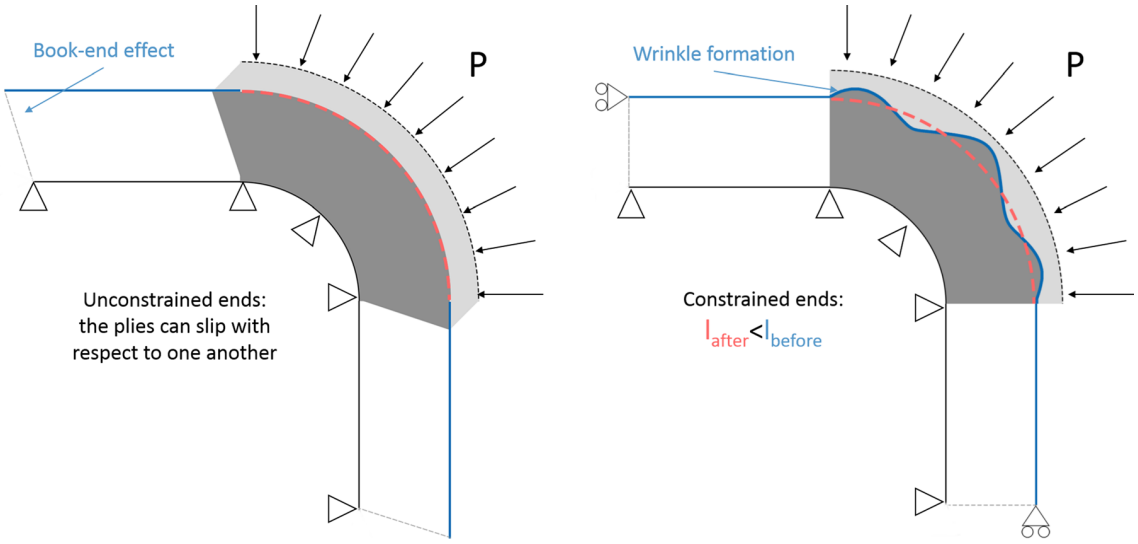

Figure 1.7: The mechanism behind out-of-plane fibre waviness upon consolidation over a curve. When the ply ends are unconstrained and the plies can slip over one another freely, the arc length reduction of the plies due to consolidation is compensated by in-plane compression or end-point extension (left). When the ply ends are constrained or the plies cannot slip over one another, the plies must buckle outwards to compensate for the arc length reduction (right) [48].

yarns rotate rigidly and the starting angle between them (usually 90°) is reduced. The friction of these crossing yarns only increases the in-plane shear stress. If this trellising continues, the yarns will eventually interlock and prevent further rotation. At this critical shear locking angle, compressive and shear forces build up until the ply buckles outward, creating the wrinkle [56, 57, 58, 59]. The research group under Hivet and Allaoui at the Université d'Orléans remarked that this mechanism for out-of-plane fibre waviness occurs largely during draping rather than consolidation, as the shear-inducing friction (between mould and fabric, fabric and fabric, and yarn and yarn) is governed by relative positioning and orientation, instead of consolidation pressure [60, 61].

Piggott et al. argue that out-of-plane fibre waviness defects are very important because they affect not only material properties but also part geometry and dimensions. This can lead to problems during assembly and expensive trimming [62]. Even if the wrinkling does not change the geometry of the part enough to warrant rejection, Zhu et al. found that fibre waviness can change a composite's in-plane Poisson ratio to be negative, causing unexpected geometrical changes upon loading [63, 64]. Farnand et al. noted that internal wrinkling cannot be seen from the outside surface of a part, meaning that even for these three-dimensional defects, non-destructive damage inspections are necessary [45].

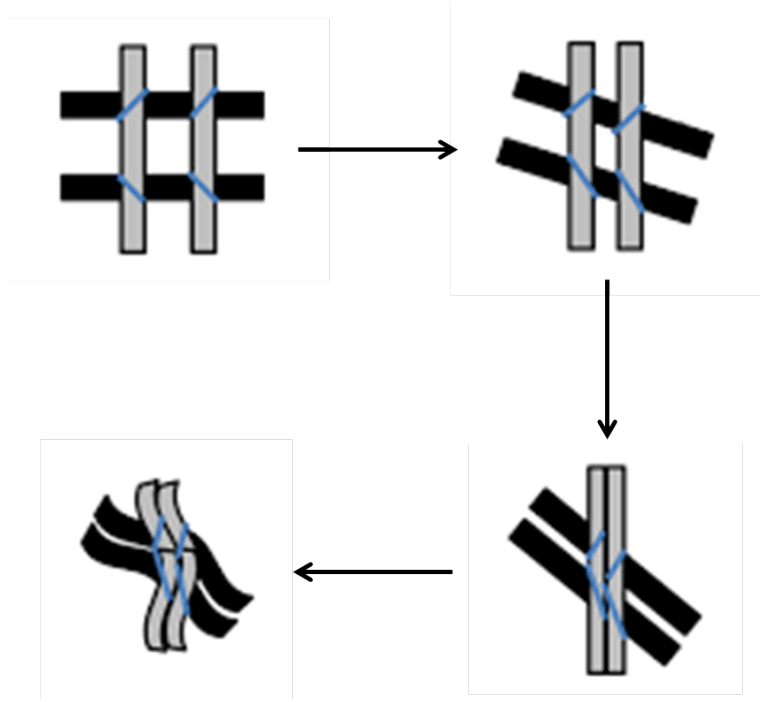

Figure 1.8: The shear-induced wrinkling mechanism for woven or bi-axial NCFs. As the fabric is draped or consolidated over a curved geometry, its warp and weft yarns rigidly rotate towards one another, until they each a critical shear locking angle, after which continued rotation is physically blocked and the built-up shear and compressive forces are manifested as wrinkles [56].

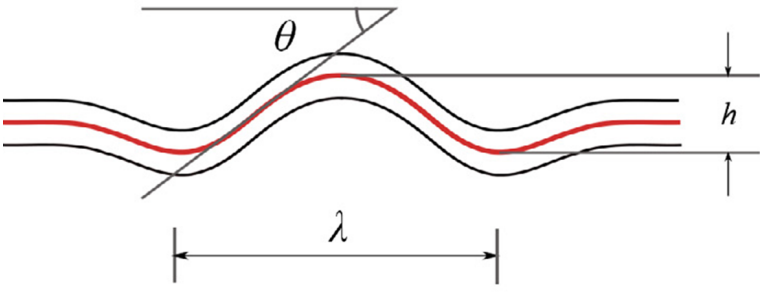

Figure 1.9: The maximum wrinkle angle (θ), wavelength (λ) and amplitude (h) of an out-of-plane waviness defect [70].

The effect of out-of-plane fibre waviness on the mechanical properties of a FRP depend most strongly on the maximum wrinkle angle (θ), followed by the wrinkle wavelength (λ) and the total size (particularly transverse to the fibre direction) of the undulating region; see figure 1.9. Sometimes, the maximum wrinkling angle is linked to the ratio of its amplitude to its wavelength [65, 66].

In compression along the fibre direction, composites with wrinkling defects fail in one of two ways. If the maximum wrinkle angle is small (approximately under 4-6°), the waviness has little influence on the compressive strength and fibre failure takes place, as would be the case if no wrinkle defects were present. The fibre properties then dominate the failure mechanism. If the maximum wrinkle angle is larger, the matrix properties determine the strength and failure mechanism of the FRP. Interlaminar shear stresses are generated around the wrinkle due to the compression, and inter-fibre failure then takes place in the form of interply delaminations or intraply matrix cracking [67, 68]. Xie et al. found a reduction of 40% in compressive strength for a CFRP as the maximum wrinkle angle increased from 4° to 28° [65]. For a similar quasi-isotropic carbon fibre/epoxy, Mukhopadhyay et al. observed a decrease in compressive strength of 34% in samples with maximum wrinkle angle of 9.9° and 11.4°, with respect to a pristine sample [68]. Nimbal et al. discovered that the location of wrinkles (and their accompanying matrix-rich zones) within a composite has a more significant influence on the reduction of compressive strength than the total number of wrinkles present [69].

Under a tensile load, wrinkles negate the stiffness of the surrounding region, which undermines its ability to carry load. As such, transverse matrix cracks can easily occur. The wrinkles also act as local interlaminar shear stress concentrators, causing delamination around the defects before any tensile fracture of the fibres takes place. This effect is amplified near the edge of composites with multi-axial reinforcing fibres, as the in-plane shear stress is localised there [70, 71]. Bloom et al. found a reduction in tensile strength of 39% in a glass fibre/epoxy laminate for a maximum wrinkle angle of 39.4°, compared to a pristine sample [71].

While in-plane compressive and tensile strengths are significantly reduced by out-of-plane fibre waviness, flexural strengths are even more affected. Matrix-rich areas are created by more wrinkled plies next to less wrinkled plies, and these areas become larger with increasing maximum wrinkle angle, increasing wave amplitude, decreasing wavelength, increasing number of concave waves and increasing wrinkle length. Larger matrix-rich areas have a weaker load carrying capacity than smaller matrix-rich or balanced fibre/matrix areas. Under

bending, the dominant failure mode is once again interlaminar shear leading to delamination and microbuckling. [66, 72] Allison et al. reported a 37% reduction in flexural strength for a glass fibre/epoxy sample with large concave up waves ($\frac{h}{\lambda} = 0.102$) with respect to a flat sample [66]. Potter et al. simulated the problem via finite element analysis (FEA) and observed a reduction of up to 72% in stress at initiation of failure under bending, if all plies were affected by wrinkling. If 25% of plies were affected, the reduction was still 35%. This corresponded to a practical experiment that was also executed on a unidirectional FRP, where 50% of plies were affected. The result of that was a flexural strength reduction of approximately 50% [72].

The final mechanical property that should be mentioned is fatigue life. Due to the small, local delaminations incurred early on by repetitive compressive or tensile loads, the material can fail, even if the applied loads are below the ultimate strength values of the wrinkled composite (which are already lower than those of a pristine composite as mentioned above). These small delaminations grow steadily with an increasing number of cycles until they become critical, leading to structural failure [73, 74]. Hörrmann et al. measured a 50% shorter fatigue life in a CFRP under a cyclical compression-compression and tension-compression load, as compared to a sample without defects [73]. Mukhopadhyay et al. found that the fatigue life of wrinkled CFRP samples was approximately one order of magnitude lower than pristine samples under the same cyclical tension-tension load [74].

1.3 Finite element modelling of fabrics

Analytical modelling of fabrics was uncommon before the 21$^{\text{st}}$ century, as it was locked behind limited computing capabilities. As computers have become increasingly powerful in the past two decades, so too has the numerical modelling of fibrous materials become increasingly popular, particularly by use of the finite element method. As computational power is still finite, large fabrics are almost never modelled in their entirety. Instead, they are represented by a unit cell in the case of periodic materials such as woven, knitted or braided fabrics, or an elementary volume in the case of non-woven fabrics. This is a limited area or volume of the fabric that can be extended to represent the entire material when periodic boundary conditions are applied [75].

Modelling fibrous materials differs from modelling more conventional materials such as metals, polymers or ceramics because of two features: the actual material properties and

their multi-scaled nature. Fibrous materials have properties that conventional materials do not exhibit. Fibres in any kind of fabric represent heterogeneous elements - rather than being part of a homogeneous material - that give the fabric anisotropic properties: tensile stiffness and strength are often many times higher in the fibre direction than in the transverse directions. This becomes particularly pronounced in fabrics where the fibres are aligned along one direction. Additionally, fabrics generally exhibit very low interfibre friction and thus low cohesion between the fibres, meaning large relative displacements can easily take place. In other words, shear stiffness through the thickness and thus flexural rigidity are very low [76]. Combining these unconventional properties with porosity and compressibility means simplifications are often made. For example, flexural rigidity is a property that is ignored in many models.

The multi-scaled nature of fibrous materials entails that they can be broken down into different constituents depending on the scale. At the macroscopic scale (from several centimetres to metres), the fabric as a whole is examined. At the mesoscopic scale (from one to several millimetres), fabrics are considered to be made out of yarns. At the microscopic scale (several micrometers), yarns are broken down into fibres. This multi-scaled nature allows for the modelling of fabrics at any of the scales, depending on the desired scope or dimensions of the model [77]. The macro-scale models can be split into continuous or discrete macro-scale models. Continuous models assume the fabric as a whole is a continuous material, while discrete models assume it is made out of an amount of simplified yarns. A similar split exists for the meso-scale models: at the mesoscopic scale, continuous models simulate each yarn but assume the yarns are continuous, while discrete models divide the yarns into an amount of fibres. Usually these fibres have larger dimensions than the actual fibres, so as not to simulate thousands of fibres per yarn. Micro-scale models are not further split up, as they all consider individual fibres to be continuous elements. Note that sometimes small parts of the fabric are modelled at a lower scale to determine accurate properties, which are then homogenised at a larger scale to reduce computation times. For example, a small section of yarn might be accurately modelled using a very large amount of fibres at the microscopic scale, after which the gathered fibre properties are used to make a homogenised meso-scale yarn model which no longer requires many elements. This can in turn be used to construct a macro-scale model; see figure 1.10. This results in models with as little loss of information as possible, though only microscopic models can ever truly be accurate, as all others make simplifications in the name of computational efficiency [75].

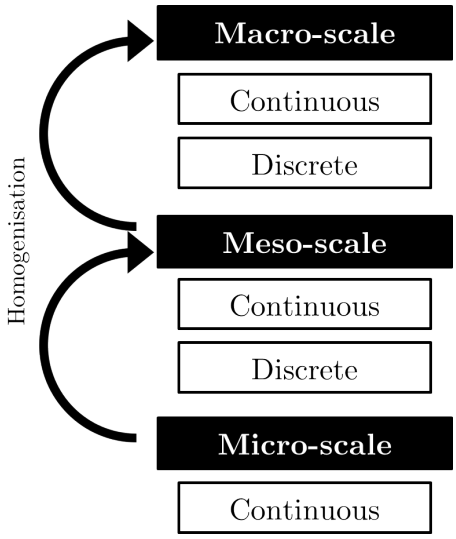

Figure 1.10: Hierarchy of the multi-scale nature of fibrous material modelling [75].

1.3.1 Macro-scale models

At the macroscopic scale, large areas of fabric can be modelled without high computational costs. This is useful when global fabric behaviour over those large areas, such as draping or wrinkling, is more important than local yarn behaviour, such as cross section deformation. As such, it is used extensively in forming and draping simulations, which are necessary to optimise the lay-up stage of composite manufacturing.

Continuous macro-scale models portray the fabric as one large, two dimensional surface. To take the fibrous material properties into account, homogenised material properties are used. Membrane elements are often employed, which are two dimensional surface elements that only transmit in-plane forces (no moments) and have no flexural rigidity [78]. For example, Nadler et al. created a multi-scale model using membrane elements but based all their mechanical properties on homogenisations of the properties at the fibre and yarn scales [79]. The most active research group developing continuous macro-scale models in recent times has been the group under Boisse et al., at the Université de Lyon. They use shell elements, which are plates that utilise the two dimensional theory of shells to approximate a three dimensional continuum material by having one dimension - the thickness - significantly smaller than the other dimensions. They have three three rotational and three displacement degrees of freedom [78]. Boisse et al. created triangular shell elements between three nodes that are subjected to tensile stresses, in plane shear moments and bending moments caused by the yarns within them and within their neighbouring shell elements. The fabrics made

from these shell elements have been draped over hemispherical, cylindrical and tetrahedral shapes, and the simulations show good correlation with experimental results in wrinkling behaviour; see figure 1.12 [54, 80, 81].

Discrete macro-scale models are based on the cargo-net or pin-jointed net approach, proposed by Kawabata et al. in 1973 [82, 83, 84]. In this approach, several points in the fabric where yarns cross each other are modelled as pins with an associated mass. These pins are then connected by one dimensional elements, allowing yarn interactions such as crimp and shear locking to be modelled. The yarns are assumed to be inextensible and are allowed to rotate, but not translate. This is not a huge restriction, as in reality these nodes do not displace much, excluding the case of out-of-plane penetration (e.g. ballistic impact simulations). Cherouat et al. used truss elements as connectors, which transmit only axial forces along their centre line and thus have no shear stiffness [78], but superimposed membrane elements onto that net to achieve the desired shear stiffness; see figure 1.13 [85]. Diehl et al. used a similar model but replaced the membrane elements for shell elements in applications where flexural rigidity (also not provided by truss elements) was more important than shear stiffness, such as fabric consolidation [77]. King et al. later created a truss pin-jointed network without membranes or shells, but with springs connecting the pin joints, making three dimensional yarn interaction possible, important for the modelling of cross sectional deformation, in-plane shear and phenomena such as crimp balance [86]. Harrison recently returned to the truss-membrane model but replaced the truss elements with beam elements, which are similar but can also transmit flexural forces [78], and used hinge elements between beam nodes. This allowed for independent control of axial stiffness along the fibre directions, in-plane shear compliance and both the out-of-plane and in-plane flexural moduli of the fabric; see figure 1.13 [87].

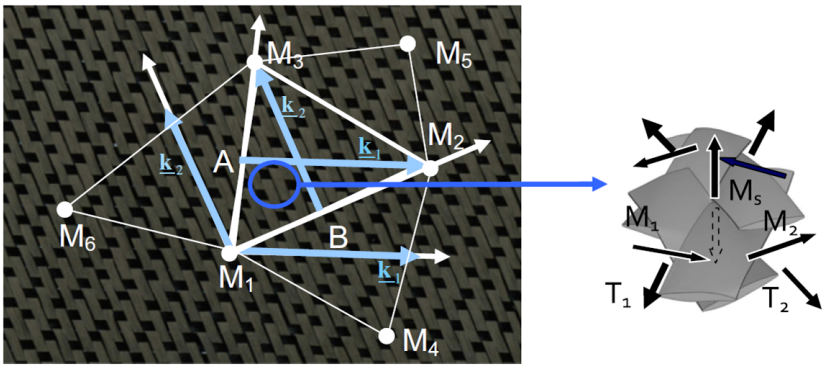

Figure 1.11: Triangular shell finite elements used in the continuous macro-scale model by Boisse et al. [80].

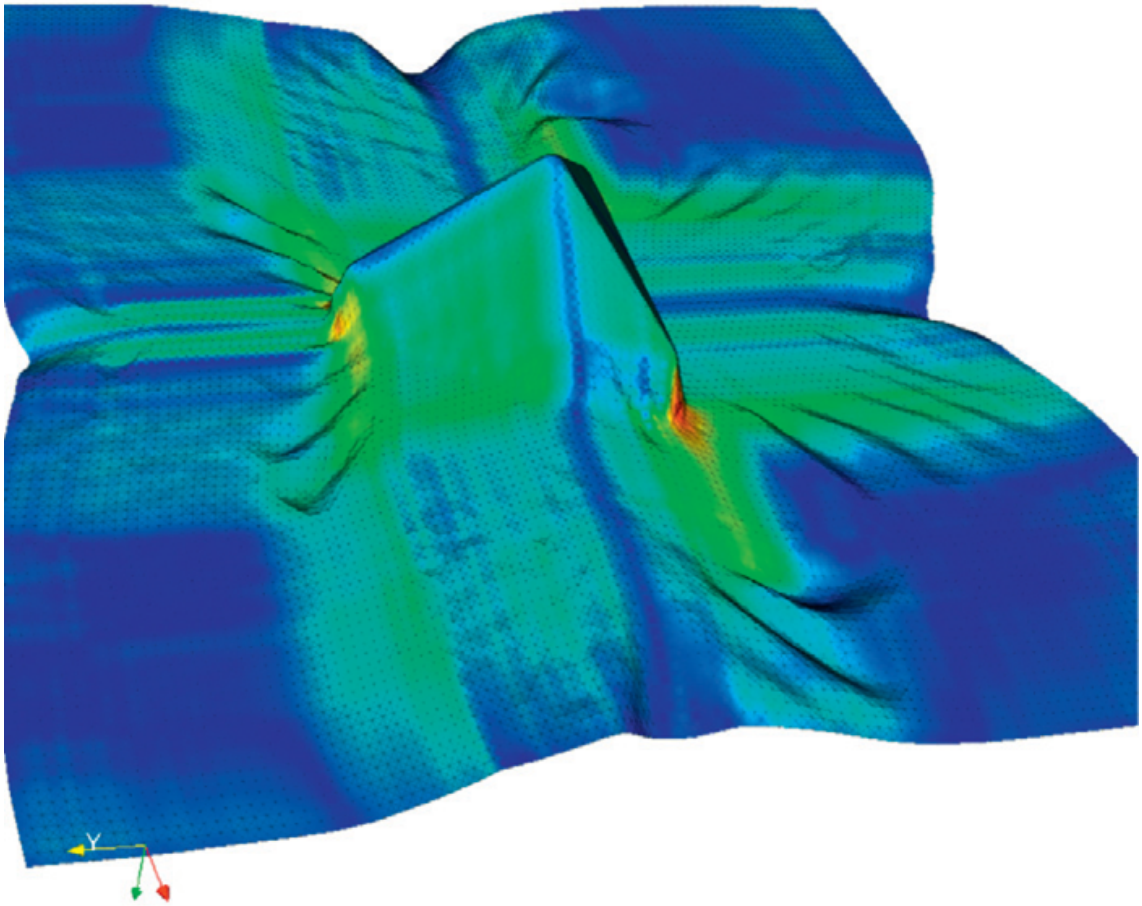

Figure 1.12: Simulation of the continuous macro-scale model by Boisse et al. draping over a tetrahedron. [81].

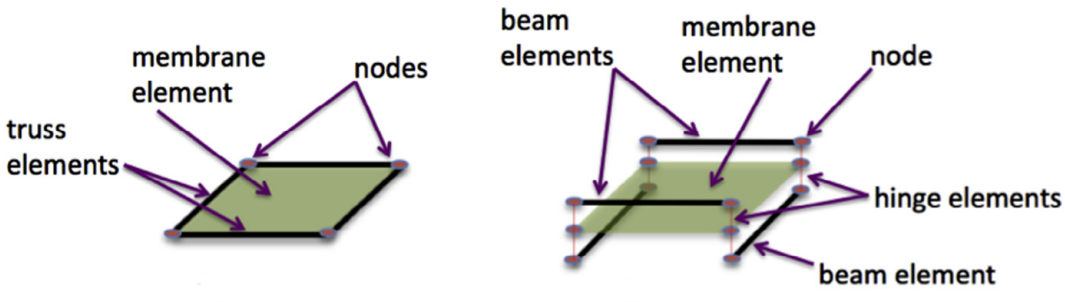

Figure 1.13: The truss-membrane discrete macro-scale model by Cherouat et al. (left) and the pantographic beam-membrane discrete macro-scale model by Harrison (right) [87].

1.3.2 Meso-scale models

The mesoscopic scale is focused on yarns, and thus meso-scale models are adopted in applications or situations where yarn behaviour is of paramount importance, such as the consolidation examined in this dissertation, or ballistic impact on woven high-strength fabrics.

Continuous meso-scale models have received a lot of attention in research due to their ease of construction and relatively low required computational power, but the yarns they model require constitutive laws and mechanical coefficients to reproduce fibre behaviour. Due to the anisotropic material properties yarns exhibit, this behaviour is often simplified to be orthotropic, or even transversally isotropic [75]. To properly model a yarn, Gasser et al. argue that it must act like a flexible thread and as such, needs to have shear moduli and a Poisson ratio close to zero. The transverse Young's modulus must also be much lower than the Young's modulus in the fibre direction; Page et al. propose a difference of a factor 100 [88, 89, 90]. Unlike continuous macro-scale models, contact interaction properties and associated interyarn friction are also needed here. All models use three dimensional solid continuum elements - which are the standard volume elements composed of one material [78] - shell elements, or a combination of the two. Shells are only used to cut down on computation time, but they do not allow for changes in yarn cross section, weakening the accuracy of the model [91]. These elements are given the required material properties by gathering experimental data and assigning them via constitutive laws, usually hypoelastic laws. This allows the elements to have orthotropic properties such as differing stiffness and strength in the fibre direction and transverse directions. Examples of continuous meso-scale models can be found in the biaxial tension simulations by Boisse et al. [89, 92, 93], the in-plane shear simulations by Badel et al. [94, 95], and the compaction simulations by Nguyen et al. [96] and Potluri et al. [22].

Discrete meso-scale models break down yarns into their constituent fibres, but do not model each individual fibre to retain lower computation times. To do so, virtual fibres that are several times the size of the real fibres, and are thus no longer truly microscopic, are employed. This still allows for interfibre interaction and displacement but can present small differences with reality. In general, discrete meso-scale fabric models are the most accurate models that can be built while retaining acceptable computation times. The discrete model stems from the work done by Wang et al. who modelled yarns as one dimensional chains of "two-node digital rod elements", that correspond to truss elements. These elements were connected

at their end nodes, instated as frictionless pins; see figure 1.14 [97]. This was of course a yarn model, and did not divide the yarn up into fibres and so always had a fixed cross section. Zhou et al. created the first real discrete meso-scale fabric model by seeing to this issue. They split the yarn into fibres and deemed that between 19 and 50 virtual fibres sufficed to represent any amount of real fibres [98]. Miao et al. later expanded on this model to improve the efficiency of the simulation, particularly its contact algorithm. They also created a final fabric model in the as-woven state without simulating the whole weaving process, but by static relaxation of yarns, saving computing time [99, 100]. Beam elements were first introduced to this multi-chain model by Durville, to study the mechanical behaviour of entangled materials [101, 102] or woven fabrics [103, 104]. Fibres were always assumed to be linearly elastic. Chakladar et al. used a similar beam multi-chain model to improve upon the discrete macro-scale model by King et al.; see figure 1.15 [105]. Green et al., Mahadik et al. and Thompson et al. studied the compaction of 3D woven fabrics using the beam model, but used elastic-plastic beam elements with constraints on the yarn end nodes to ensure periodicity [76, 106, 107]. The main weakness of this model was the inherent link between in-plane stiffness and flexural rigidity, leading to an overestimation of the flexural rigidity and requiring artificial solutions. This will be further examined in section 3.1. Thompson et al. additionally applied a negative thermal load (thermal shrinkage) to the original fabric topology to obtain the as-woven state, and found this to be equivalent to applying tension during a weaving process, drawing the fabric together [107].

1.3.3 Micro-scale models

Modelling of fabrics at the microscopic scale is rarely done and hard to find in literature, because it is so computationally intensive. At this scale, each real fibre is modelled as a virtual fibre with the same dimensions and properties, leading to the best possible fabric model. A micro-scale model was built by Duhovic et al. to investigate deformation in knitted fabrics, but only 20 fibres of the 120 fibres per yarn were actually modelled.

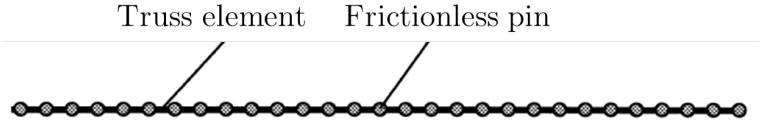

Figure 1.14: The discrete yarn model by Wang et al., made up of truss elements connected by frictionless pins at the nodes [97].

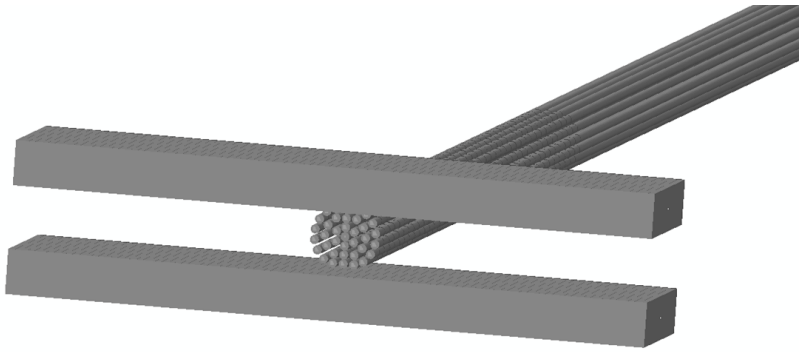

Figure 1.15: The discrete meso-scale model by Chakladar et al., where yarns are constructed from 37 chains of beam elements. The upper and lower rigid bars are used for a compaction simulation [105].

Nevertheless, the fibres were kept true to their real dimensions - a diameter of 17 µm - and the model was thus microscopic in scale. Each fibre was modelled using linearly elastic beam elements with a circular profile [108]. Instead of studying a global fabric, micro-scale modelling has also been used to study the behaviour of single yarns, for example by Van Langenhove. They constructed a model to predict yarn stress-strain and torque-strain behaviour, using geometrical fibre properties (e.g. twist angle, packing density, interfibre friction) as inputs [109, 110, 111].

1.4 Goal and scope of this dissertation

It is clear that the consolidation stage during the composite manufacturing process has a significant effect on the final mechanical properties and geometry of the produced FRP part. Currently, ensuring a correct V_f is reached while keeping defects at a minimum relies heavily on the manufacturer's experience and trial-and-error [48]. This is the cause of a lot of waste generation. For example, Airbus estimates that between 30% and 50% of composite parts for aircraft are scrapped due to manufacturing errors or induced defects [112]. This obviously translates into high costs, both in wasted materials and processing time, and in waste disposal. Material costs are significant in composite production, representing 20-60% of the total production cost of CFRPs, depending on the manufacturing throughput [113, 114, 115]. As most FRPs are not recyclable and are disposed of via landfill or incineration, this waste generation also imposes a heavy burden on the environment [112]. As such, a better understanding of fabric consolidation behaviour is necessary, so that accurate

predictions can be made before production commences, leading to parts with fewer defects, reduced manufacturing inspection costs and increased manufacturing throughput [45]. As experimental manufacturing trials are expensive, FEA of fabric consolidation has become the most important predictive tool in the industrial community [48].

The goal of this dissertation, then, is to create a robust fabric model that can be used as such a predictive tool. The model needs to be able to take any load (particularly compressive loads) and accurately portray consolidation. A woven fabric will be modelled instead of a NCF as they are known to have better drapeability, meaning woven fabrics are used when complex mould geometries and thus more defects are involved [116]. Actual simulation of these defects is beyond the scope of this dissertation, though the goal is for the created fabric model to be applicable to this end in future work. Next to all the numerical analysis, consolidation behaviour of a woven fabric will also investigated experimentally.

In chapter 2, the fabric used during this dissertation is given, as are the tools used to create and validate the model, and to perform and process the experiments. In chapter 3, the creation of the model is outlined from the ground up, starting at the microscopic scale and ending at the macroscopic scale. In chapter 4, the model is validated by comparing the simulated as-woven results to the geometry of the real fabric, and the fabric model with the most accurate parameters is chosen. In chapter 5, this model is subjected to consolidation and results are discussed. The experimental consolidation results are also found here. Note that many of the parameters that affect consolidation such as temperature and number of compression iterations have not been taken into account in this dissertation. The focus is kept at the applied pressure.

Chapter 2

Materials and methods

2.1 Materials

2.1.1 Fabric

The fabric that the finite element model in this dissertation is based on, is a 2/2 twill weave produced by P-D Interglas Technologies GmbH, to aviation and automotive standards. This means that the weft yarn passes over two warp yarns, then under two warp yarns, and so on. One unit cell of this weave is defined to be a cut-out area of four warp yarns and four weft yarns, as that is the smallest repeating unit in the fabric geometry; see figure 2.1.

The fabric is made of E-glass, combining filaments with a diameter of 9 µm, both in the warp and the weft direction. According to the producer, this creates warp yarns with a yarn number of 340 tex and weft yarns with a yarn number of 272 tex. The thread count is 6 warp ends per cm, and 6.7 weft ends per cm. The fabric as a whole has an areal density of 390 $\frac{g}{m^2}$ and is treated with a 0.5-1.5% FK 144 finish (Interglas style 92140); see figure 2.2 [117, 118, 119].

As the areal and volumetric densities of the material are important factors in the calculation of the V_f and in the simulation, these properties were experimentally measured. To measure the area of a surface, an accurate ruler was used on a square fabric coupon, cut out using glass fibre scissors. To measure the mass of such a coupon, a calibrated scale was used. To determine the volume, the fabric coupons were individually submerged in water and the

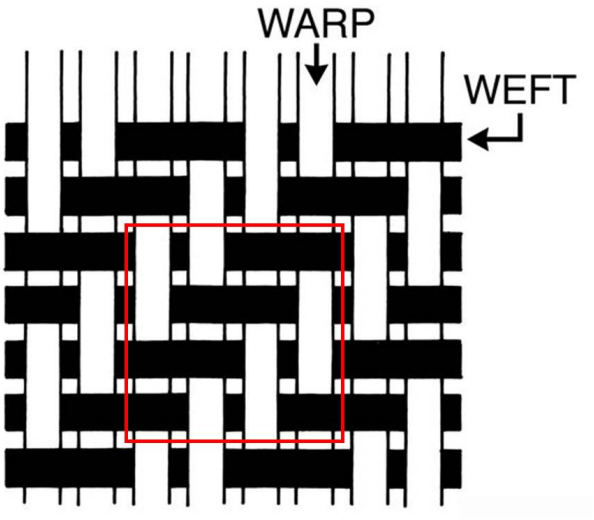

Figure 2.1: Pattern of a 2/2 twill weave, with a single, repeating unit cell marked within the red square [120].

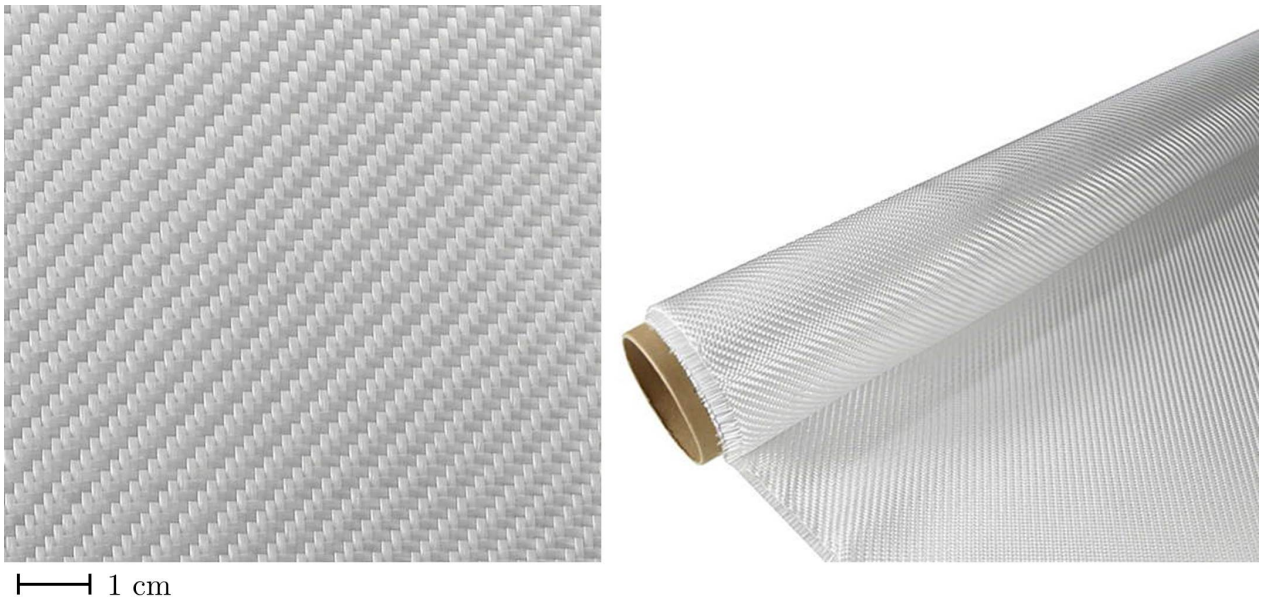

Figure 2.2: The E-glass fibre 2/2 twill fabric produced by P-D Interglas Technologies GmbH, used as a basis for the finite element model in this dissertation [119].

displaced volume of water (equal to the volume of the fabric) was measured via its mass.

$$\rho_A = \frac{m_{fabric}}{A_{fabric}}$$
$$\rho_V = \frac{m_{fabric}}{V_{fabric}}$$

Here, ρ_A and ρ_V are the areal and volumetric densities, respectively, while $\mathrm{m_{fabric}}$, $\mathrm{A_{fabric}}$ and $\mathrm{V_{fabric}}$ are the mass, surface area and volume of the fabric. An average areal density of 386.52 $\frac{\mathrm{g}}{\mathrm{m^2}}$ was found, with a standard deviation of 6.60 $\frac{\mathrm{g}}{\mathrm{m^2}}$. This is very close to the predetermined areal density of 390 $\frac{\mathrm{g}}{\mathrm{m^2}}$ given by the manufacturer. For the volumetric density, an average of 2295.08 $\frac{\mathrm{kg}}{\mathrm{m^3}}$ was measured, with a standard deviation of 10.30 $\frac{\mathrm{kg}}{\mathrm{m^3}}$, which is somewhat lower than the conventional values of 2540-2550 $\frac{\mathrm{kg}}{\mathrm{m^3}}$ for E-glass density [121].

To be able to calculate the required flexural rigidity of the simulated beam elements (see section 3.2), an accurate measurement of the yarn number was required. This measurement was executed according to ISO 7211/5 and ISO 7211/3 (1984). The standards require a yarn number to be estimated by simply measuring the mass and length of several yarns with a scale and a ruler, and calculating the yarn number:

$$\text{yarn number} = \frac{m_{yarn}}{l_{yarn}}$$

Here, $\mathrm{m_{yarn}}$ and $\mathrm{l_{yarn}}$ represent the mass and length of a yarn, respectively. This resulted in average yarn number estimates of 341.92 tex for the warp direction, and 263.23 tex for the weft direction. To now more accurately measure the yarn lengths, prestress was applied to each yarn in the fibre direction. The standards specify a prestress of $0.5 \cdot$ estimated yarn number, in cN, but only 63 cN was available in the used ITF maillemeter. As such, maximum prestress was applied. The length of 10 warp and 10 weft yarns was measured with the maillemeter, and bundles of 50 yarns of each direction were weighed using a calibrated scale. Using the above formula, the yarn number was found to be 337.88 tex in the warp direction, with a standard deviation of 0.71 tex, and 268.75 tex in the weft direction, with a standard deviation of 0.41 tex. Both values are similar to those provided by the manufacturer of the fabric.

The relevant physical properties of the fabric, that will be used throughout this dissertation, are summarised in table 2.1.

	Warp	Weft
Weave	2/2 twill	
Volumetric density $[\frac{\text{kg}}{\text{m}^3}]$	2295.08	
Areal density $[\frac{\text{g}}{\text{m}^2}]$	386.52	
Young's modulus [GPa]	70	
Poisson coefficient [-]	0.2	
Yarn number [tex]	337.88	268.75
Fibre diameter [µm]	9	9

Table 2.1: Relevant properties of the glass fibre fabric material used in this dissertation, either supplied by the manufacturer or experimentally determined.

2.1.2 Matrix material

For the compression experiment with static loading, an epoxy resin was used to make small composite samples. EPIKOTE Resin MGS RIMR 135 was used, with EPIKURE Curing Agent MGS RIMH 137, both produced by Hexion [122]. A mass ratio of 10 parts epoxy resin to 3 parts curing agent was used.

2.2 Methods

2.2.1 Finite element analysis (FEA)

2.2.1.1 Modelling and simulation

The software used for the finite element modelling of the fabric and analysis of its compression behaviour is Abaqus Unified FEA, also called ABAQUS, by the Dassault Systèmes Simulia Corporation. This is in fact an entire product suite, containing pre-processing (ABAQUS/CAE), processing (ABAQUS/Standard, ABAQUS/Explicit, etc.) and post-processing (ABAQUS/CAE) software, thus not requiring any external software to execute entire analyses [75]. In the pre-processing step, the model is constructed geometrically and then meshed. Material properties and boundary conditions are also applied at this stage. The processing step is somewhat of a black box for the user, but it is during this step that any calculations are performed. Essentially, the solver calculates the forces at each

node for each time step, according to Newton's second law of motion. In this dissertation, ABAQUS/Explicit is used, because it allows for contact between truss elements and remains stable when calculating large deformations. In the post-processing step, any results of the simulation can be requested and visualised.

The ABAQUS product suite is commonly used for FEA in the oil and gas, life sciences, aerospace, automotive, industrial equipment, consumer packed goods and electronics industries [123]. It was chosen because the Department of Materials, Textiles and Chemical Engineering (MaTCh) at Ghent University has extensive experience with the suite, and because it is has a good reputation within academic and commercial institutions for the modelling of fabrics [48, 50, 51, 75, 81, 87, 124, 125, 126]. ABAQUS version 6.18-1 (2018) was used.

To assist in modifying and creating input files for ABAQUS, scripts were written in Python version 3.7.3. The *Tkinter* package was used to create a graphical user interface (GUI), though this was only implemented for ease of repetitive use and had no technical impact.

2.2.1.2 Distance measurements

The post-processing ABAQUS/CAE was used to measure the yarn widths and heights of the as-woven but uncompressed fabric models, to compare their geometries to experimental data for model validation. To do so, the deformed fabric was shown in the CAE viewer, with beam profiles rendered for easier distinction of the individual fibres. The required warp or weft fibres were then displayed while removing all other elements from view to prevent the selection of incorrect nodes. It should be noted that the truss elements were always displayed and the beam elements were always hidden, as the truss elements represent the actual geometry of the fabric and the beam elements only contribute their flexural rigidity (see section 3.1). Once a correct angle was found to view the yarn under so that the fibres at the extrema ("left" and "right" for yarn width, i.e. highest and lowest X or Y coordinates, or "top" and "bottom" for yarn height, i.e. highest and lowest Z coordinates) were unmistakably identified, the distance between these extrema was queried. ABAQUS/CAE measures distances in X, Y and Z components instead of a vector sum, but as the warp yarns were modelled to align with the X-direction and the weft yarns were modelled to align with the Y-direction, this was acceptable. It means warp yarn widths were always measured in the Y-direction, weft yarn widths were always measured in the X-direction, and yarn heights were always measured in

the Z-direction. Whether the result was positive or negative depended only on which of the two nodes was selected first and had no impact: physically, lengths are always positive. Note that ABAQUS measures the distance between nodes which lie on the centre line of the fibres; this means the actual yarn widths and heights are two fibre radii larger than the result it returns. For each yarn, this measuring process was repeated five times along the length of the yarn, in equidistant intervals. The yarns were virtually cut through for easier access to the nodes at those interval boundaries by using the free body cuts integrated in the CAE viewer. Figure 2.3 shows an example of this measuring process for the width of a weft yarn.

2.2.2 Micro-computed tomography (µCT)

2.2.2.1 Imaging

To evaluate the results of compression experiments and to validate the created fabric model, µCT-scanning was used. This is a method for the three dimensional imaging of both dry and embedded fabrics via X-rays. The main advantages it has is that it is a highly accurate, non-destructive technique, allowing for the examination of cross sections without difficult mechanical sectioning that can generate damage in the material [127]. It can also be performed in-situ if desired [128, 129].

All µCT-scans were executed at the Ghent University Centre for X-ray Tomography (UGCT), on a tomograph named HECTOR. This tomograph generates X-rays with an XWT 240-SE microfocus source and utilises a large PerkinElmer flat panel detector, which allows for images with a maximum spatial resolution of approximately 10 µm [130].

To create compound images of µCT cross sections, GIMP version 2.8.22 was used. No measurements were performed with this program.

2.2.2.2 Distance measurements

To process the µCT-scans, which are reconstructed into image sequences, the Java-based image processing program ImageJ was used. Specifically, the Fiji distribution package (version "Madison") that contains ImageJ version 1.52i was used. Just like in ABAQUS/CAE, the program was used to measure yarn widths and heights, but from experimental data rather than simulations. It was also used to measure the distance between compression plates in the determination of V_f. To do this, the reconstructed image sequence

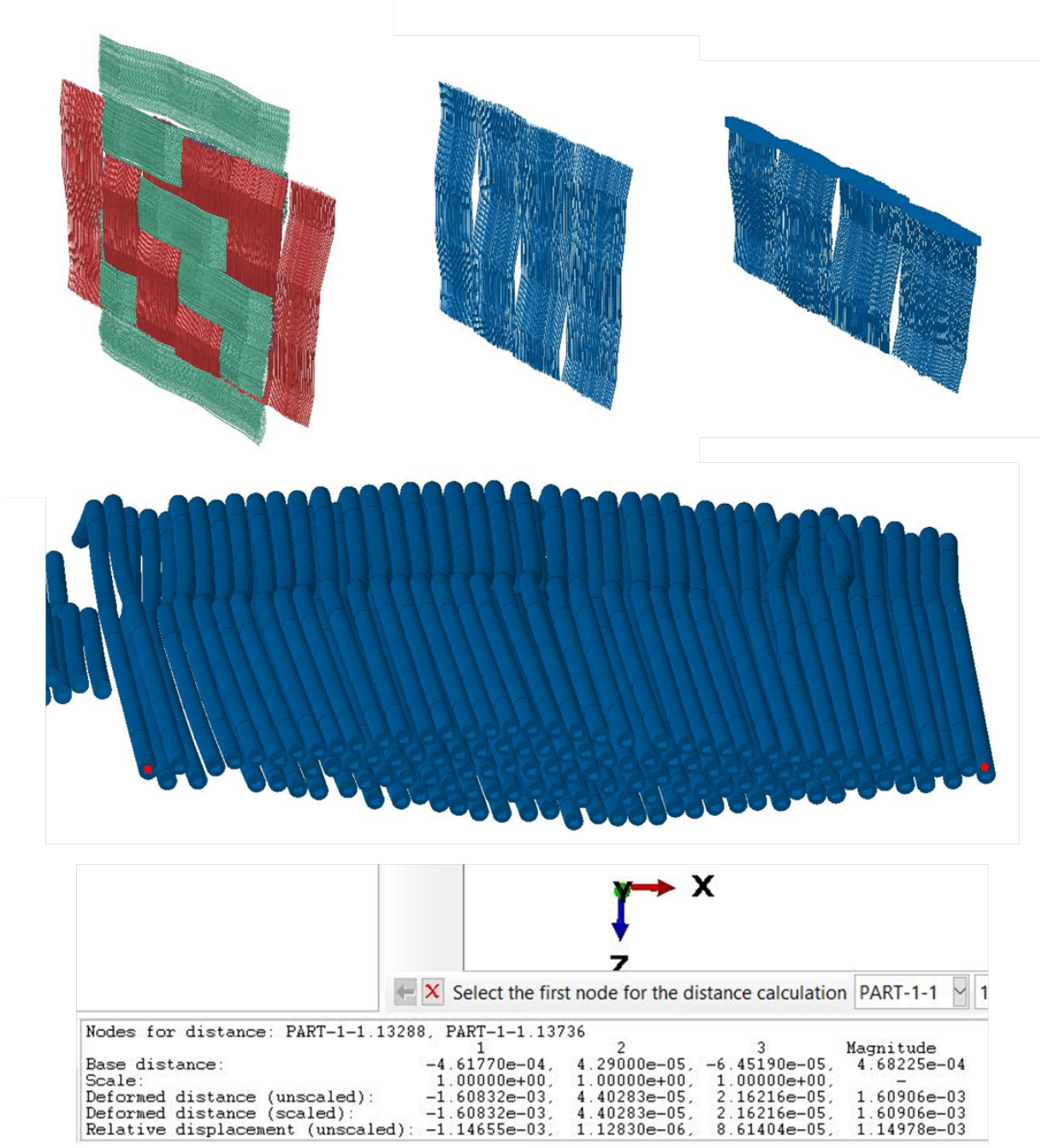

Nodes for distance: PART-1-1.13288, PART-1-1.13736

	1	2	3	Magnitude
Base distance:	-4.61770e-04,	4.29000e-05,	-6.45190e-05,	4.68225e-04
Scale:	1.00000e+00,	1.00000e+00,	1.00000e+00,	-
Deformed distance (unscaled):	-1.60832e-03,	4.40283e-05,	2.16216e-05,	1.60906e-03
Deformed distance (scaled):	-1.60832e-03,	4.40283e-05,	2.16216e-05,	1.60906e-03
Relative displacement (unscaled):	-1.14655e-03,	1.12830e-06,	8.61404e-05,	1.14978e-03

Figure 2.3: The yarn width measuring process in ABAQUS/CAE. First, the deformed fabric is displayed and beam profiles are rendered (top left). All unnecessary fibres are then temporarily removed from view, in this case leaving only weft fibres displayed (top middle). Each yarn is measured at 5 equidistant points along its axis; this is achieved by free body cuts (top right). The yarn cross section is angled to see which fibres form the extrema, and the distance between them is measured by querying the distance between the frontmost nodes of each fibre, as indicated by the red dots (middle). The measured distance is read from the "Deformed distance" row and the column corresponding to the measuring direction, in this case along the X-axis, corresponding to "1" (bottom).

was imported into the program, displaying an XY ("top-down") cross section of the fabric. To ensure correct scaling, the digital voxel size was set to correspond to the voxel size stipulated in the reconstruction data file. This XY view was then resliced to transfer to an XZ or YZ point of view instead, revealing cross sections of the individual yarns. Zooming in on these allowed for the measurement of distances by drawing straight lines and querying their length. Figure 2.4 shows an example of this measuring process for the width of a yarn. Note that some of these µCT-images had a high amount of noise and low contrast, and as such, selecting the correct voxels at the extrema proved difficult. To compensate for this uncertainty, the error margins were manually increased, depending on the severity of the noise.

2.2.3 Compression experiments

In this dissertation, two experiments were carried out with the same goals in mind: to experimentally observe fabric behaviour during compression, and to have empirical data against which to validate the created finite element model. The first experiment used in-situ µCT to scan a dry fabric sample as it was being compressed. The second experiment consisted of subjecting resin-embedded fabric samples to a static load and µCT-scanning them after the matrix had cured, capturing the fabric deformation. In both cases, single layers of the glass fibre fabric and stacks of 4 layers of the fabric were compressed and scanned.

2.2.3.1 Experiment 1: continuous loading

For the in-situ scanning experiment, a uniaxial compression cell by Deben (UK) was used, called the CT5000-TEC. This device was developed to fit on the HECTOR tomograph at the UGCT and is controlled by Deben Microtest software; see figure 2.5 [130]. A load cell with a maximum force of 1 kN was used and a constant strain rate of 0.5 $\frac{\text{mm}}{\text{min}}$ was applied to the dry fabric samples. The load was exerted by the Deben cell onto the samples via two circular PEEK jaws, or clamps. The top jaw had a height of 59.5 mm and the bottom jaw had a height of 19.5 mm. Both had a radius of 44 mm.

While the pressure could be increased continuously, the µCT-scanning did not happen continuously. Around certain loads (e.g. 1.2 N, 5 N, 10 N, 15 N, 30 N, 120 N, 240 N, 800 N and back down to 0 N for the single layer of glass fibre fabric), the Deben cell compression was paused and a µCT-scan was taken. As such, continuous machine data is available from the Deben cell, but only discrete image data is available from the tomograph.

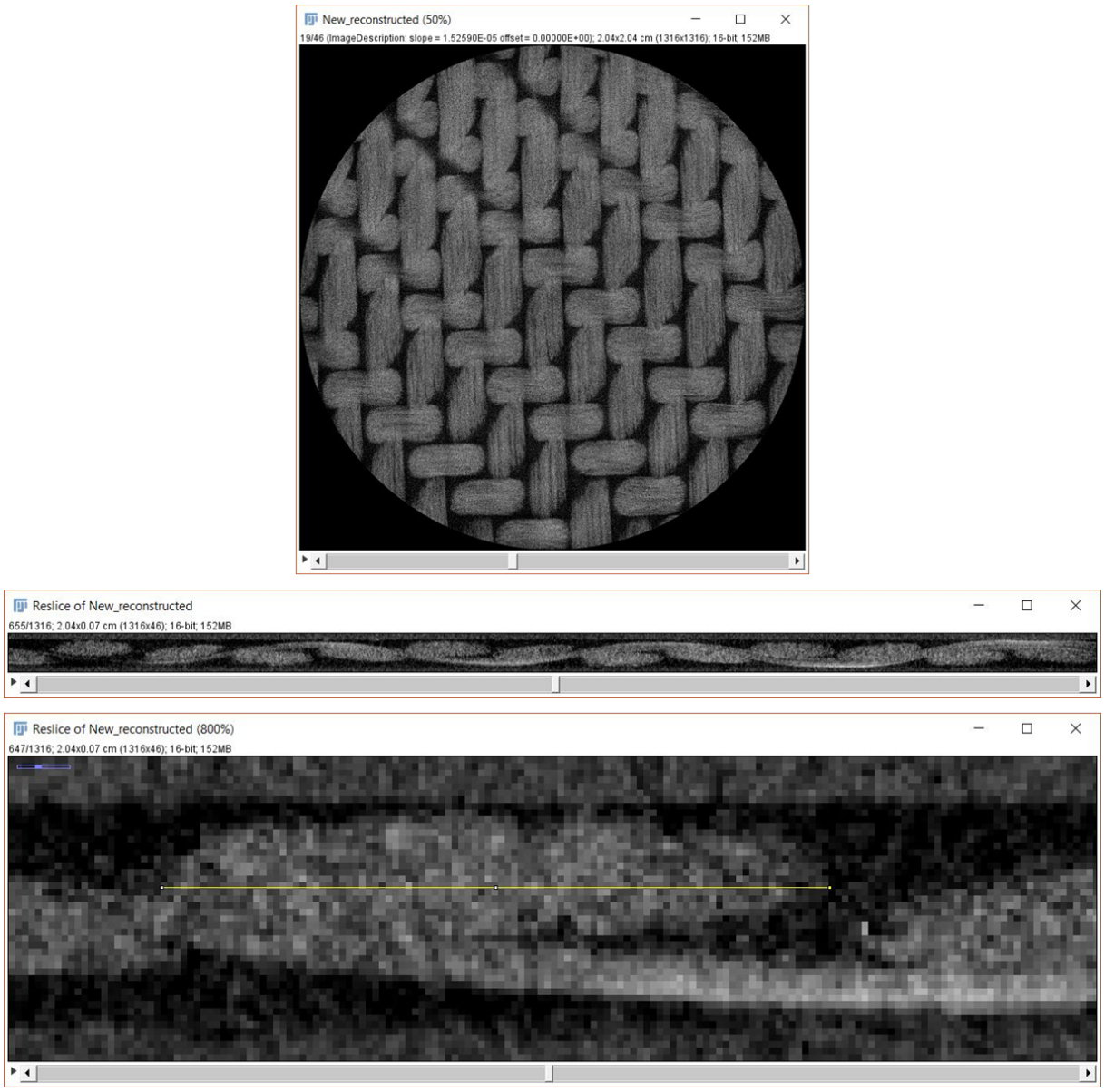

Figure 2.4: The yarn width measuring process in ImageJ. First, the reconstructed µCT image sequence is imported, revealing an XY cross section of the fabric. At this point the scale is set so that the voxel size is correct (top). A reslice is then taken, along one of the axes. This produces an XZ or a YZ cross section of the fabric, revealing the cross sections of the weft and warp yarns, respectively (middle). A straight line is drawn between the voxels on the extrema of the yarn cross sections, as indicated by the yellow line, and the length of the line is queried (bottom).

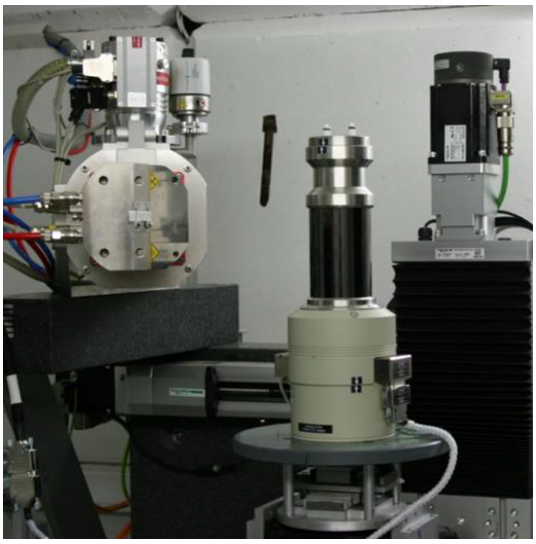

Figure 2.5: The Deben CT5000-TEC cell, mounted on the HECTOR tomograph [130].

For the test on the single layer of fabric, the samples used in this experiment contained 13 warp yarns and 14 weft yarns. The average yarn width before compression was measured in µCT images (as described in subsubsection 2.2.2.2) to be 1.619 mm with a standard deviation of 0.089 mm in the warp direction, and 1.581 mm with a standard deviation of 0.094 mm in the weft direction. The 4 layer sample consisted of only 12 warp yarns and 12 weft yarns. The warp yarns had an average width of 1.629 mm with a standard deviation of 0.109 mm, and the weft yarns had an average of 1.543 mm with a standard deviation of 0.025 mm. These measurements allow for the calculation of the average fabric area of each sample (A_{sample}):

$$\begin{aligned} A_{sample} &= (N_{warp} \cdot d_{warp}) \cdot (N_{weft} \cdot d_{weft}) \\ \Rightarrow A_{sample,1\ layer} &= (13 \cdot 1.619mm) \cdot (14 \cdot 1.581mm) \\ &= 466.063\ mm^2 \\ \Rightarrow A_{sample,4\ layers} &= (12 \cdot 1.629mm) \cdot (12 \cdot 1.543mm) \\ &= 361.955\ mm^2 \end{aligned}$$

Here, N_{warp} and N_{weft} are the amount of warp or weft yarns in the sample, respectively, and d_{warp} and d_{weft} are the average widths of the warp and weft yarns in the sample. $A_{sample,1\ layer}$ is the average fabric area of the single layer sample, and $A_{sample,4\ layers}$ is the average fabric area of the sample constructed out of 4 layers of fabric stacked on top of each other. These values will become necessary when calculating the pressures these samples are subjected to during consolidation.

2.2.3.2 Experiment 2: static loading

In the second experiment, the noise and inaccuracies generated by the Deben cell (see section 4.1) were attempted to be negated by creating fabric samples compressed under static loads, and by fixing the fabric deformation under those loads by embedding the fabric in resin before µCT-scanning. To apply the static loads, aluminium weights were used. Since relevant pressures had to be achieved and a maximum of approximately 10 kg could be placed on a sample, the sample surface areas had to be small but still representative of the entire fabric. Samples were cut using glass fibre scissors to be 2 cm · 2 cm (4 cm^2), containing at least 9 unit cells and allowing pressures to reach around 0.25 MPa:

$$\begin{aligned} P &= \frac{F_{weight}}{A_{fabric}} \\ &= \frac{m_{weight} \cdot g}{A_{fabric}} \\ &= \frac{10\ kg \cdot 9.81\ \frac{N}{kg}}{4\ cm^2} \\ &= 0.2455\ MPa \end{aligned}$$

P is the pressure on the fabric, F_{weight} is the force exerted by the weight onto the fabric, A_{fabric} is the surface area of the fabric, m_{weight} is the mass of the aluminium weights and g is the gravitational acceleration constant (approximated as 9.81 $\frac{N}{kg}$). This value of 0.25 MPa is much lower than the ultimate pressures reached using the Deben cell, but most µCT-scans were actually taken below this pressure. 6 out of 8 scan points of the single layer fabric and 8 out of 10 points of the 4-layer fabric were below this threshold.

A problem now occurred: these small 4 cm^2 samples had to be subjected to the full force of the weights, distributed equally over the fabric surface. To facilitate this, top moulds were made out of steel sheets. Squares of 6 cm · 6 cm, 4 cm · 4 cm and 2 cm · 2 cm were cut using a tabletop metal shear. It was ensured that the smallest of these squares had the exact intended size and a flat surface by grinding. These squares were then glued to each other (using epoxy glue) in a pyramid shape; see figure 2.6.

The eventual setup used to create the compressed composite samples is shown in figure 2.7. The fabric - 1 layer or 4 layers - was placed on a glass plate that had been treated with a release agent. A small amount of epoxy resin was then manually added to the fabric - just enough to cover it. No attention was paid to the entrapment of air bubbles that would

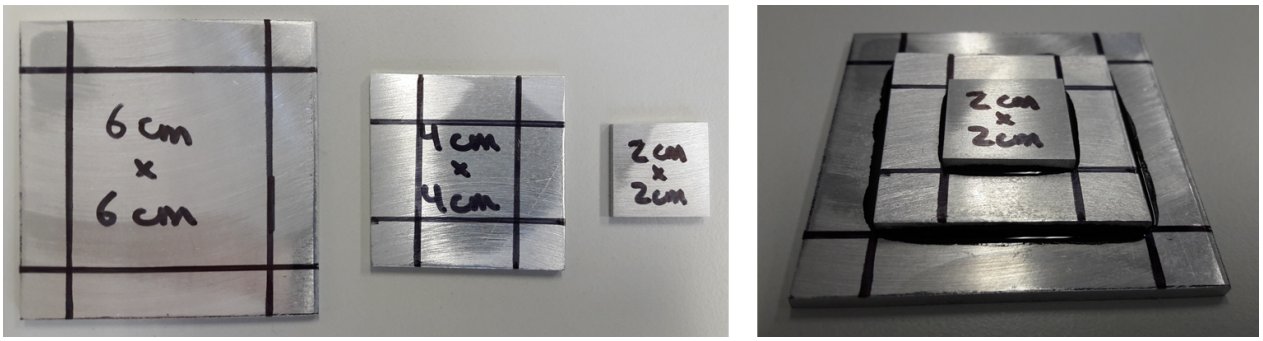

Figure 2.6: The steel squares used to create a top mould for the static loading experiment. Via grinding, the smallest square was ensured to be the correct size and have a flat surface (left). These squares were glued to each other to make the mould (right).

usually be avoided when making a FRP, as the resin's only purpose was to anchor the fibres. A release foil was placed on top of the fabric-resin mix and the mould was carefully aligned on top of that. This mould provided a larger, 6 cm · 6 cm surface to place the aluminium weights on top of, while only transferring that weight to a 2 cm · 2 cm area underneath the mould - exactly the size of the fabric samples. The composites were left to harden for 48 hours at room temperature, and were then cured for 1 hour at 80°C.

The final pressure applied to the fabric depended on the mass placed on top of it, as seen in the previous formula. It should be noted that the mass of the steel top mould was also taken into account, but the mass of the release foil or resin was deemed negligible. The final masses (weights + mould) placed on the composite samples were weighed using a calibrated scale and are shown in table 2.2, alongside the pressure they exerted on the samples.

Goal mass [kg]	**Real mass [kg]**	**Pressure [MPa]**
0	0	0
0.5	0.501	0.0123
1	0.99	0.0243
2	2.087	0.0512
5	4.943	0.1212
10	10.009	0.2455

Table 2.2: The masses (and their respective exerted pressures) placed on top of the composite samples, to provide static loading during curing.

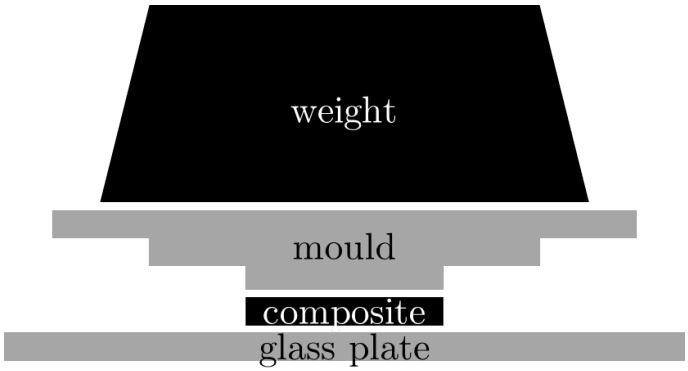

Figure 2.7: Experimental setup to create the composite samples under static loading. The mass of the weight was varied to achieve different load pressures. The composite consisted of 1 or 4 layers of glass fibre fabric embedded in resin. The glass plate and mould were treated with release agent or covered in release foil so as not to stick to the resin.

Chapter 3

Fabric model creation

The fabric model in this thesis is built at multiple scales. First, the fibres and their mechanical properties are examined at the microscopic scale, where the individual finite elements are chosen to best represent all deformation behaviour in a fibre. These fibres are then combined into a yarn at the mesoscopic scale, where the flexural rigidity of the yarn as a whole needs to be implemented. Finally, the yarns are woven into a fabric at the macroscopic scale. The final model can be considered a discrete meso-scale model, as fibres are kept discrete, even at the fabric level, rather than yarns or even the entire fabric being imagined as continuous elements. It is not a full micro-scale model because not every real fibre is represented by a virtual fibre. Instead, a smaller amount of larger virtual fibres make up the yarns.

3.1 Fibre model (micro-scale)

At the microscopic scale, fibres (or more accurately, filaments) can easily be modelled as flexible, one-dimensional chains made up of sequentially connected structural elements; see figure 3.1. This provides a highly flexible structure, as the elements can rotate relative to each other at the connection nodes.

As mentioned in subsection 1.3.2, particularly relevant structural elements in the modelling of fibres are truss and beam elements. In ABAQUS, these are long, thin, cylindrical rods that act as one-dimensional elements in a two- or three-dimensional environment. Truss elements only transmit axial forces along their centre line and thus do not transmit forces perpendicular to the centre line or any moments [78]. When these elements are used, the connecting nodes function as frictionless pins [75]. The restricted load transmission means

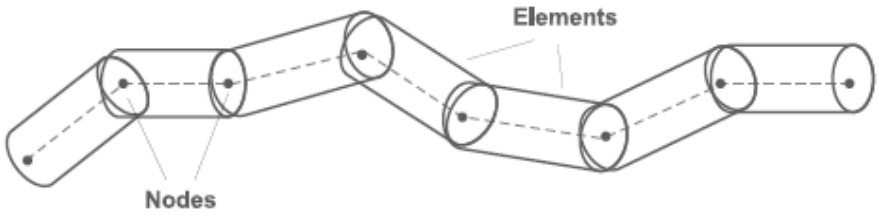

Figure 3.1: A fibre model consisting of structural truss or beam elements, sequentially connected by single-point nodes along the centre line [75].

trusses are usable as computationally cheap elements for the modelling of fibres if those fibres are loaded in the fibre direction, especially in tension, where no buckling takes place, but they are weak candidates in any case where other loading is applied. To simulate the consolidation stage, where pressure is applied perpendicular to the fibre directions and where the fibres are expected to bend, these elements alone are not sufficient.

Beam elements are much broader in the transmission of loads. They are designed as flexural members and so can transmit bending moments and shear forces alongside the usual axial forces [78]. There are two main types of beam elements: Euler-Bernouilli beams that calculate deformation during bending as a function of the applied moment and the element's flexural rigidity, and Timoshenko beams that also allow for transverse shear in the calculation [131]. In any case, both types of beam elements are intrinsically more suited to the modelling of fibres than truss elements, in any load situation where bending takes place.

To illustrate the difference in bending behaviour, a digital experiment was set up, as described by Daelemans [75]. A 20 mm length of fibre (modelled after carbon fibre but with increased diameter for clearer visualisation) is clamped to a curved rigid surface, called the die, on one side. Its other end is suspended over the die and is pulled downwards by 12.5 mm, as if to simulate the bending of the fibre over the die under the influence of gravity; see figure 3.2. The qualitative results are shown in figure 3.3. It is clear that because trusses do not transmit bending moments, their bending behaviour is unrealistic: the elements only start displacing when the element connected to them is displaced in the axial direction. This creates a fibre which seems to "float in the air". If the length of the trusses is reduced to zero, a completely flexible thread would be obtained. Beam elements do transmit bending moments, and as such, the whole fibre immediately starts displacing when a load perpendicular to the fibre direction is applied.

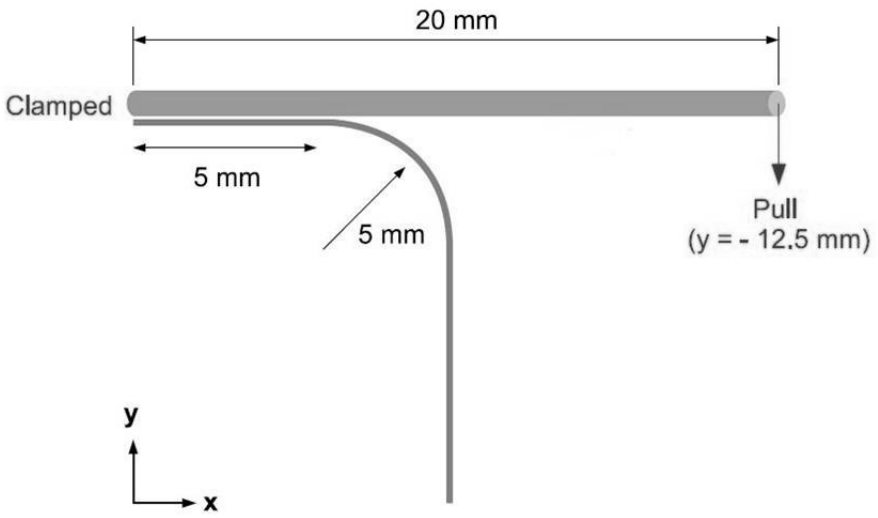

Figure 3.2: The setup for a digital experiment to visualise the difference in bending behaviour in fibres made of truss elements and those made of beam elements [75].

In this dissertation, both truss and beam elements are used simultaneously. T3D2 trusses are used, which is ABAQUS' notation for truss elements in a three-dimensional space with one node on either side of each element, on the centre line. The trusses have only three degrees of freedom (translational) at each node. B31 beams are used, which is ABAQUS' notation for Timoshenko beam elements in a three-dimensional space that use linear interpolation. The beams have six degrees of freedom at each node (three translational and three rotational). The actual implementation of these elements on a fibre is easy within ABAQUS: when a wire part is created and meshed, the structural elements can be generated in between the mesh nodes. The mesh in this dissertation was created so that each element was approximately 0.16 mm long.

Considering that consolidation applies compressive forces perpendicular to the fibre direction, it would seem that modelling the fibre using beam elements would be appropriate. This is, however, problematic due to the nature of fibre properties, as Green et al., Mahadik et al. and Thompson et al. discovered [76, 106, 107]. Unlike other materials, fibres have a very high tensile strength and Young's modulus coupled with very low but not negligible flexural rigidity. As flexural rigidity is defined as $E \cdot I$, where E is the Young's modulus and I is the area moment of inertia, it is clear that a high Young's modulus can only be coupled with a low flexural rigidity if the area moment of inertia is low. The latter, however, is only dependent on the geometry of the fibre's cross-section, which is assumed to be a circle. With r being the radius of the fibre, its area moment of inertia is calculated as follows:

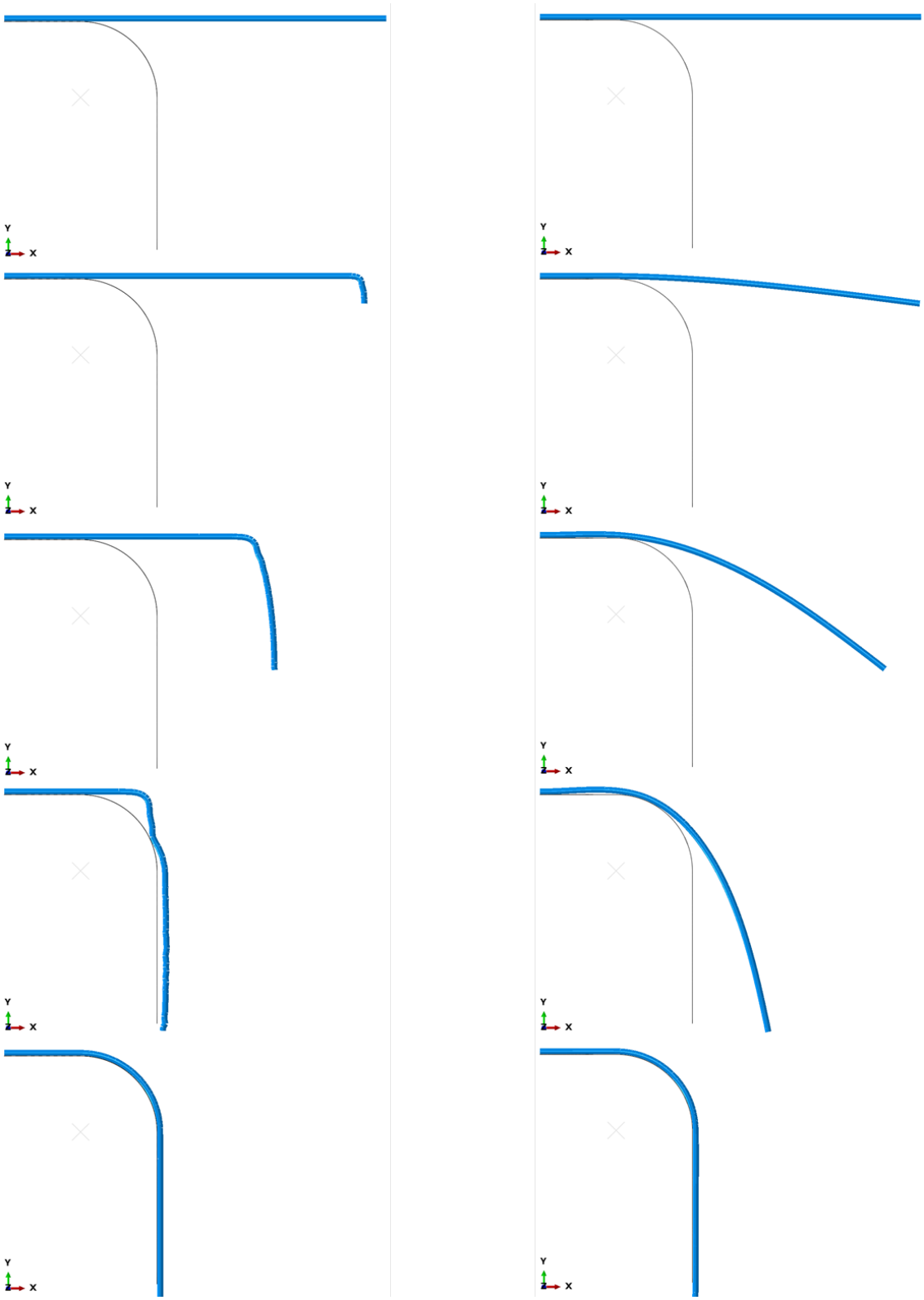

Figure 3.3: The bending behaviour of a fibre made of truss elements (left) and beam elements (right). It is clear that trusses do not provide realistic bending behaviour because they do not transmit bending moments between nodes. Beam elements bend accurately.

$$
\begin{aligned}
I_{xx} &= \iint_R y^2 \, dx \, dy \\
&= \iint_R (r \cdot sin\theta)^2 \, dx \, dy \\
&= \int_0^{2\cdot\pi} \int_0^r r^2 \cdot sin^2\theta \cdot r \, dr \, d\theta \\
&= \int_0^{2\cdot\pi} \frac{r^4 \cdot sin^2\theta}{4} \, d\theta \\
&= \frac{\pi \cdot r^4}{4} \\
I_{yy} &= \frac{\pi \cdot r^4}{4}
\end{aligned}
$$

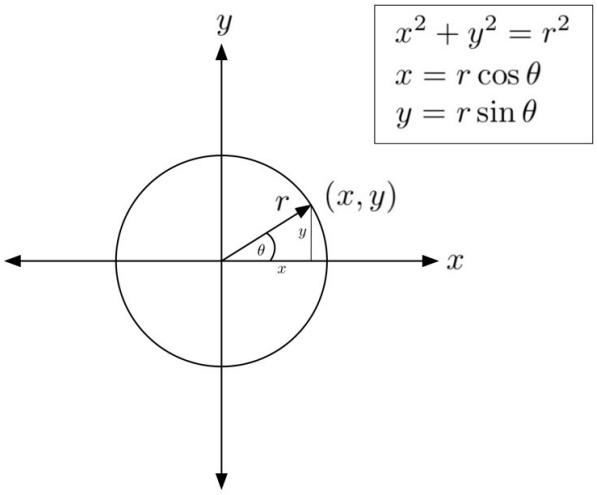

This means that the area moment of inertia cannot artificially be lowered while keeping a circular profile and a correct fibre radius, which leads to an overestimation of the flexural rigidity. To tackle this problem, a novel method is introduced in this dissertation, which has not yet been reported in literature: the Young's modulus and flexural rigidity properties are disconnected from each other. First, truss elements are used to model the fibre geometry and are given the correct Young's modulus of the modelled material. Beam elements are subsequently superimposed on top of these truss elements, between the same nodes, to determine the flexural rigidity. These beam elements are given a Young's modulus equal to the real modulus divided by 100 (inspired by Page et al. [90]), so as not to affect the stiffness of the total model in any significant way. To compensate, the area moment of inertia is multiplied by 100 to reach the correct flexural rigidity. This is done by increasing the radius of the beam elements by $\sqrt[4]{100}$ but removing any contact interaction properties from those elements. In this way, overly large beam elements do not influence the actual fibre (or yarn or fabric) geometry but do contribute their flexural rigidity and transmission of bending moments. A test fibre model with truss and beam elements superimposed in this way was created and subjected to the digital visualisation experiment (as in figure 3.2) and was found to display the same qualitative bending behaviour as the beam model, as was expected.

3.2 Yarn model (meso-scale)

To construct an accurate yarn model, the yarn in the real fabric must be examined. It is clear that the yarn is actually a tow - an untwisted bundle of continuous filaments - as is often the

case for fibres used in composite applications. To create such a tow, fibres have to be placed alongside each other, arranged into a certain packing. Real yarns tend to have an imperfect, open packing, but in yarn models this disorder is replaced by an idealised structure. The most common idealised packing model is (hexagonal) closed packing. In this model, the fibres are fit into a hexagonal pattern surrounding a central fibre, which minimises the voids left between the fibres; see figure 3.4 [132]. After deformation, for example by incorporating the yarn into a woven fabric model, the idealised packing is removed. Miao et al. found that the initial packing (whether open or closed) has no significant effect on the deformed geometry and, as such, the easy to implement hexagonal closed packing model will be used in this dissertation [99]. In the model assembly in ABAQUS/CAE, yarns can be created in this way by copying a fibre axisymetrically around a central fibre.

In this hexagonal closed packing, the amount of fibres per yarn can only assume certain values. If l is the amount of hexagonal layers (not counting the central fibre), the amount of fibres in a yarn n is found as [133]:

$$n = 1 + 3 \cdot l \cdot (l + 1)$$

This means the amount of fibres per yarn can be 1, 7, 19, 37, 61, 91, 127, and so on. Of course, the amount of fibres in a real yarn is orders of magnitude above these values. This can be estimated from the material properties listed in table 2.1:

$$\begin{aligned}
n_{real} &= \frac{yarn\ number}{mass\ per\ unit\ length_{fibre}} \\
&= \frac{yarn\ number}{A_{fibre,real} \cdot \rho} \\
&= \frac{4 \cdot yarn\ number}{\pi \cdot {d_{fibre,real}}^2 \cdot \rho} \\
\Rightarrow n_{real,warp} &= \frac{4 \cdot 337.88\ tex}{\pi \cdot (9\mu m)^2 \cdot 2295.08 \frac{kg}{m^3}} \\
&= 2314.28\ \frac{fibres}{yarn} \\
\Rightarrow n_{real,weft} &= \frac{4 \cdot 268.75\ tex}{\pi \cdot (9\mu m)^2 \cdot 2295.08 \frac{kg}{m^3}} \\
&= 1840.74\ \frac{fibres}{yarn}
\end{aligned}$$

Here, $A_{fibre,real}$ is the cross sectional area of the real fibre, ρ is the volumetric density of

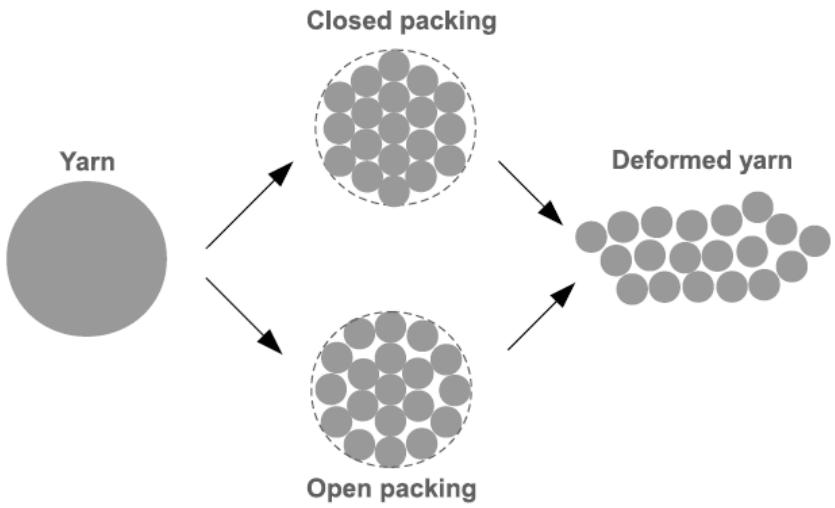

Figure 3.4: The difference between idealised closed packing and more realistic open packing for the assembly of fibres in a yarn model [75].

E-glass and $d_{fibre,real}$ is the diameter of the real fibre. For FEA, it is not realistic to model yarns consisting of thousands of fibres, as that would require too much computational power. In this dissertation, yarns made up of 61, 91 and 127 fibres ($n_{virtual}$) are used instead. This smaller amount of fibres still needs to represent the same cross sectional area as the real fibres to accurately portray the yarn geometry. If the total area of the real and virtual fibres is noted as $A_{total,real}$ and $A_{total,virtual}$, respectively, then the cross sectional area of the single virtual fibre ($A_{fibre,virtual}$) can be expressed as follows:

$$
\begin{aligned}
A_{total,virtual} &= A_{total,real} \\
\Leftrightarrow n_{virtual} \cdot A_{fibre,virtual} &= n_{real} \cdot A_{fibre,real} \\
\Leftrightarrow A_{fibre,virtual} &= \frac{n_{real} \cdot \pi \cdot {d_{fibre,real}}^2}{4 \cdot n_{virtual}} \\
\Rightarrow A_{fibre,virtual,warp} &= \frac{2314.28 \ \frac{fibres}{yarn} \cdot \pi \cdot (9\mu m)^2}{4 \cdot n_{virtual}} \\
\Rightarrow A_{fibre,virtual,warp} &= \frac{1840.74 \ \frac{fibres}{yarn} \cdot \pi \cdot (9\mu m)^2}{4 \cdot n_{virtual}}
\end{aligned}
$$

The numerical results of this calculation are summarised in table 3.1. These virtual cross sectional areas are two orders of magnitude larger than the cross sectional area of the real fibres ($6.36 \cdot 10^{-11}$ m^2), which explains why the model that is being built is a discrete meso-scale model instead of a true micro-scale model.

$\mathbf{n_{virtual}}$ $[\frac{\mathbf{fibres}}{\mathbf{yarn}}]$	**61**	**91**	**127**
$\mathbf{A_{fibre,virtual,warp}}$ $[\mathbf{m^2}]$	$2.41 \cdot 10^{-9}$	$1.62 \cdot 10^{-9}$	$1.16 \cdot 10^{-9}$
$\mathbf{A_{fibre,virtual,weft}}$ $[\mathbf{m^2}]$	$1.92 \cdot 10^{-9}$	$1.29 \cdot 10^{-9}$	$9.22 \cdot 10^{-10}$

Table 3.1: The cross sectional area each virtual fibre needs to have to accurately represent real fibres without having as many fibres per yarn. These cross sectional areas define the size of the truss elements in the yarn model.

The virtual cross sectional areas in table 3.1 define the size of the truss elements in the yarn model, as it is these elements' responsibility to portray the geometry of the yarns in the combined truss-beam model. The beam elements, on the other hand, are designed solely to contribute flexural rigidity to the virtual yarn. This is done by equating the flexural rigidity of the virtual yarn ($(E \cdot I)_{yarn,virtual}$) to that of the real yarn ($(E \cdot I)_{yarn,real}$):

$$
\begin{aligned}
(E \cdot I)_{yarn,virtual} &= (E \cdot I)_{yarn,real} \\
\Leftrightarrow n_{virtual} \cdot (E \cdot I)_{fibre,virtual} &= (E \cdot I)_{yarn,real} \\
\Leftrightarrow I_{fibre,virtual} &= \frac{(E \cdot I)_{yarn,real}}{n_{virtual} \cdot E} \\
\Leftrightarrow \frac{\pi \cdot {r_{fibre,virtual}}^4}{4} &= \frac{(E \cdot I)_{yarn,real}}{n_{virtual} \cdot E} \\
\Leftrightarrow r_{fibre,virtual} &= \sqrt[4]{\frac{4 \cdot (E \cdot I)_{yarn,real}}{\pi \cdot n_{virtual} \cdot E}} \\
\Rightarrow r_{fibre,virtual,warp} &= \sqrt[4]{\frac{4 \cdot (E \cdot I)_{yarn,real,warp}}{\pi \cdot n_{virtual} \cdot E}} \\
\Rightarrow r_{fibre,virtual,weft} &= \sqrt[4]{\frac{4 \cdot (E \cdot I)_{yarn,real,weft}}{\pi \cdot n_{virtual} \cdot E}}
\end{aligned}
$$

Here, $(E \cdot I)_{fibre,virtual}$ and $I_{fibre,virtual}$ are the flexural rigidity and area moment of inertia of a single virtual fibre, respectively. $r_{fibre,virtual}$ is the radius of a single virtual fibre and defines the size of the beam elements in the combined truss-beam model. Note that the Young's modulus in this equation is artificially lowered by a factor 100, as discussed above.

To be able to calculate the required dimensions, the flexural rigidity of the real yarn must first be known. This is measured experimentally according to BS 3356 (1961), based on the Peirce cantilever test. In this test, a fabric sample cut to 200 mm in length and 25 mm in width is placed on top of a flat surface, which is coated to reduce friction with the fabric. The

sample is then slid forward. This makes the leading edge of the fabric bend downwards under gravity as it is no longer supported (much like the digital bending test that was performed on single fibres in figure 3.2). When the fabric is bent enough so that the edge reaches a certain angle θ below the top surface, the test is stopped and the overhanging length l is measured using a graduated ruler; see figure 3.5. This overhanging length is multiplied by a scaling factor f_1 to reach a certain bending length c [134]:

$$\begin{aligned} c &= f_1 \cdot l \\ &= \sqrt[3]{\frac{cos\frac{\theta}{2}}{8 \cdot tan\theta}} \cdot l \end{aligned}$$

The angle θ is taken as 41.5° in the used standard because for this angle, the scaling factor becomes 0.5093, which is often rounded down to 0.5 for ease of use [135]. With the correct bending length, the flexural rigidity of a real fabric ($(E \cdot I)_{fabric,real}$) can finally be calculated:

$$(E \cdot I)_{fabric,real} = w \cdot c^3$$

Here, w stands for the areal weight of the fabric. For the yarn model in this dissertation, a slightly altered version of the Peirce cantilever test was performed, using single yarns as specimens instead of fabric cut-outs. This means that instead of an areal weight, a linear weight w_{yarn} was used in the formula instead:

$$\begin{aligned} (E \cdot I)_{yarn,real} &= w_{yarn} \cdot c^3 \\ &= yarn\ number \cdot g \cdot c^3 \\ \Rightarrow (E \cdot I)_{yarn,real,warp} &= yarn\ number_{warp} \cdot g \cdot c_{warp}^3 \\ \Rightarrow (E \cdot I)_{yarn,real,weft} &= yarn\ number_{weft} \cdot g \cdot c_{weft}^3 \end{aligned}$$

An average overhang length of 69.8 mm was found for the glass fibre fabric's warp yarns (with a standard deviation of 7.6 mm), and an average of 65.8 mm was found for the weft yarns (with a standard deviation of 6.2 mm). With these measurements, calculation of the flexural rigidities and required beam radii is possible. The results are shown in table 3.2.

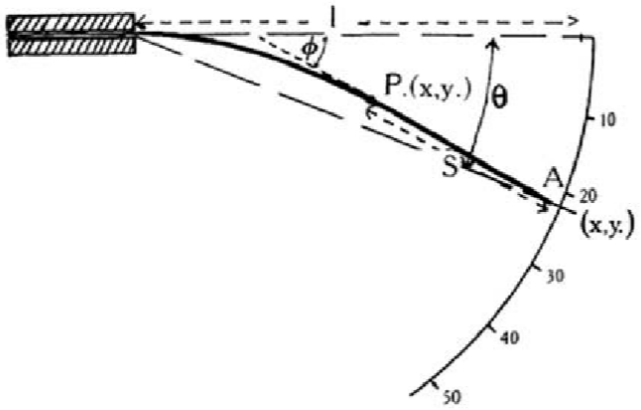

Figure 3.5: The setup of a Peirce cantilever test. A fabric sample is laid on top of a flat surface and gradually slid forward until its free edge bends down to reach a line $\theta°$ (usually 41.5°) below the top surface. The overhanging length l is then measured [134].

$\mathbf{n_{virtual}}$ $[\frac{\mathbf{fibres}}{\mathbf{yarn}}]$	**61**	**91**	**127**
$\mathbf{(E{\cdot}I)_{yarn,real,warp}}$ $[\mathbf{N{\cdot}m^2}]$	$1.49 \cdot 10^{-7}$		
$\mathbf{r_{fibre,virtual,warp}}$ $[\mathbf{m}]$	$4.59 \cdot 10^{-5}$	$4.15 \cdot 10^{-5}$	$3.82 \cdot 10^{-5}$
$\mathbf{(E{\cdot}I)_{yarn,real,weft}}$ $[\mathbf{N{\cdot}m^2}]$	$9.92 \cdot 10^{-8}$		
$\mathbf{r_{fibre,virtual,weft}}$ $[\mathbf{m}]$	$4.15 \cdot 10^{-5}$	$3.75 \cdot 10^{-5}$	$3.45 \cdot 10^{-5}$

Table 3.2: The flexural rigidity of the real yarns in both warp and weft directions, and the corresponding radii that the virtual beam elements need to have to accurately represent the real flexural rigidity if their Young's modulus is artificially reduced by a factor 100.

3.3 Fabric model (macro-scale)

3.3.1 Existing truss fabric model

Now that the combined truss-and-beam fibre model has been integrated into a yarn model, all that is left is to integrate these yarns into a woven fabric model. An already existing model built by Daelemans in 2017 was used as a basis for this. That model was constructed to emulate the same 2/2 twill weave, glass fibre fabric as described in subsection 2.1.1. Three versions of the model exist, including 61, 91 or 127 fibres per yarn. They have identical fibre and yarn models as described in this dissertation, except that they use pure truss element chains as fibres instead of combined truss-and-beam element chains.

A single unit cell consisting of four warp yarns and four weft yarns was modelled, and to ensure the unit cell was representative for the entire fabric, periodic boundary conditions were imposed. First, the nodes at both ends of each yarn were connected by equations so that they could only displace in the exact same way, creating simple periodicity. This did not hinder unravelling of the yarns and left free edges, so conditions to simulate neighbouring yarns along the edges of the unit cell were required. A system of so-called master and slave yarns was used to this end. Along each edge of the unit cell, a copy of the yarn on the opposite side of the unit cell (the master yarn) was introduced as a slave yarn; see figure 3.6. Each node in the slave yarn was then tied to its corresponding node in the master yarn via pin MPCs, to duplicate the master yarn in all six degrees of freedom, creating "perfect" periodicity. These slave yarns act as a contact surface for the yarns along the edges of the unit cell within the layer, but also in adjacent layers if the single layer was copied above or below itself [107]. It was discovered that simply duplicating the master yarns seemed to provide stress relief for the edge yarns of the unit cell, as all deformation was force-controlled. As such, a force applied to an edge yarn caused only half as much deformation as that same force applied to an inner yarn because the force had to deform both the master and slave yarn. To combat this, the Young's modulus of the slave yarns was reduced by a factor 100 so that their deformation became governed purely by that of the master yarns.

After the loose topology of the single unit cell and its slave yarns was modelled, a method for reaching the as-woven state was required. This was achieved by applying a negative thermal load to the yarns, similar to Thompson et al., using thermal shrinkage to relax the woven fabric structure [107]. The applied load was calculated so that the final yarn length would equal the experimentally measured yarn length; in other words, ensuring the crimp was equal. It was found that relaxing directly to the crimped state, however, resulted in a stressed fabric with lower than expected thickness. To solve this, the real weaving process was more accurately taken into account: during weaving, yarns are subjected to high axial forces and have low crimp, but when they are cut from the roll they can relax, reducing stress and increasing crimp. To model this, the loading step was split into two stages. In stage 1, the weaving is simulated and the thermal shrinkage is equal to an arbitrary 1.25 times the desired final crimp value. In stage 2, the relaxation is simulated and the thermal shrinkage is set to reach the desired final crimp value. This two-step loading process resulted in higher thickness fabrics with lower remaining stress. While replacing an actual weaving simulation, the thermal shrinkage will be further referred to as the "weaving" process in this dissertation.

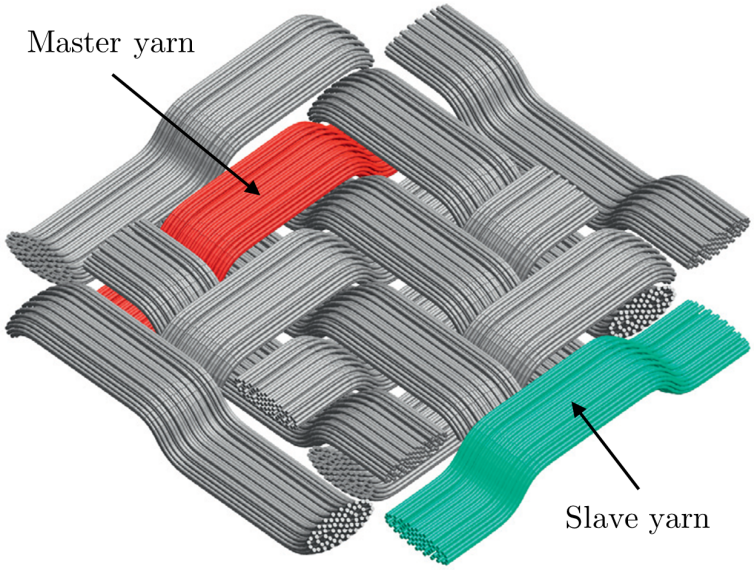

Figure 3.6: Slave yarns inserted along the edges of a fabric unit cell to ensure periodicity. Each slave yarn is a copy of the master yarn on the opposite side of the unit cell and is tied to that master yarn via MPCs in each corresponding node [107].

The model was validated based on the comparison of the digital warp yarn width, weft yarn width and fabric thickness with the corresponding experimental values. The portrayal of the as-woven state was found to be accurate, which was to be expected as the weaving process is governed by axial loads which can be transmitted by trusses; see figures 3.7 and 3.8. The lack of any flexural rigidity (due to the lack of beam elements), however, means that it cannot simulate compression behaviour correctly.

3.3.2 New truss-and-beam fabric model

To create the fabric model outlined in this dissertation, the linearly elastic material properties defined in the truss model were first updated. A more accurate experimental density was measured for the fabric, and estimates of the Young's modulus and Poisson coefficient were inserted; see table 2.1. This was done via a custom Python script, which became the foundation for a modular and reusable ABAQUS input file editor, given in full in appendix A. The script determines the location of the material properties definitions, then copies the whole input file but applies whatever changes are requested to the lines containing the information on the material properties. It works with a GUI to allow for easier user input of the desired changes.

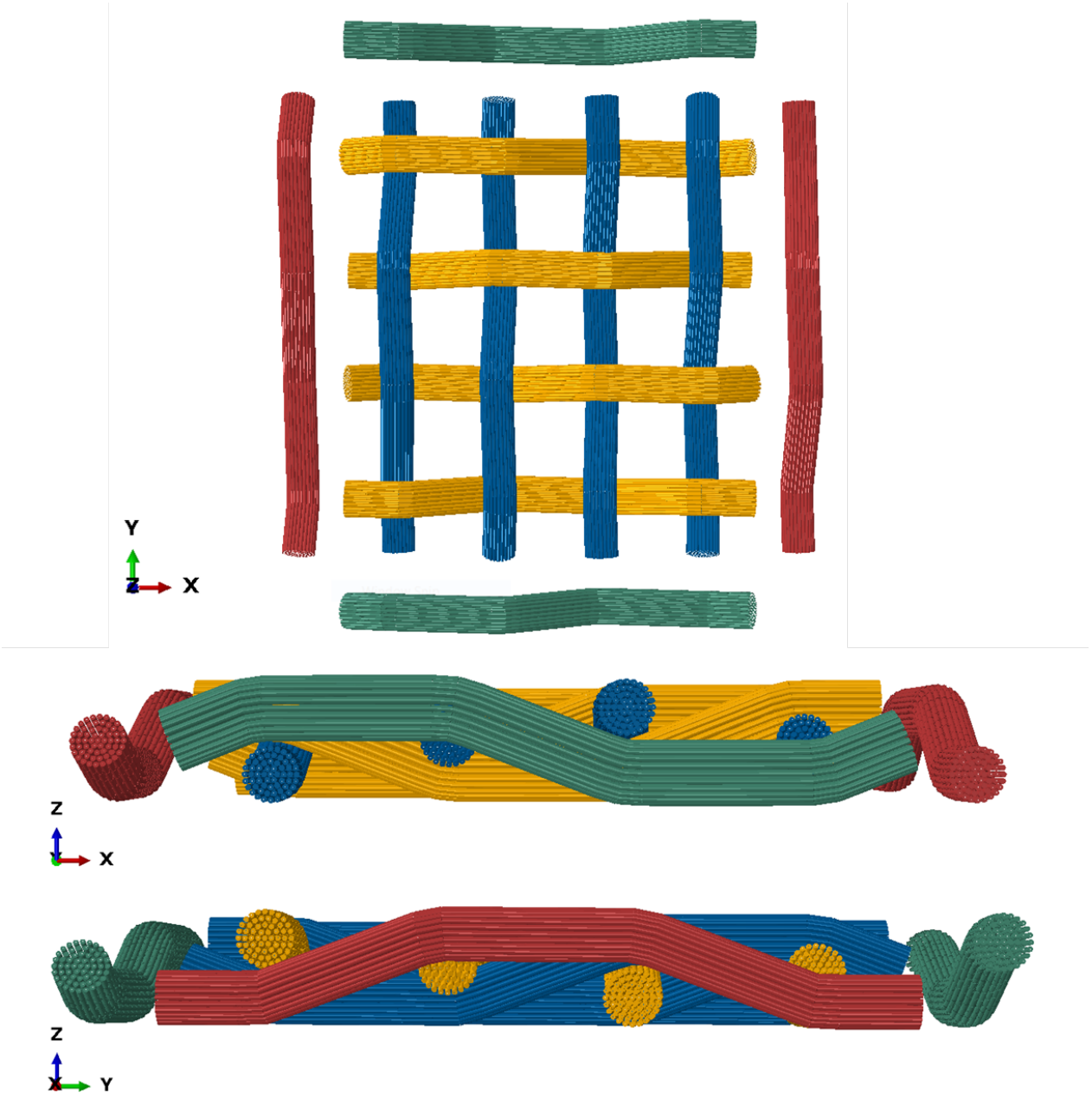

Figure 3.7: The basic truss fabric model (61 fibres per yarn) by Daelemans in its undeformed, loose topology state. The warp yarns (X-direction) are yellow, the weft yarns (Y-direction) are blue. The green and red slave yarns have an artificially reduced Young's modulus.

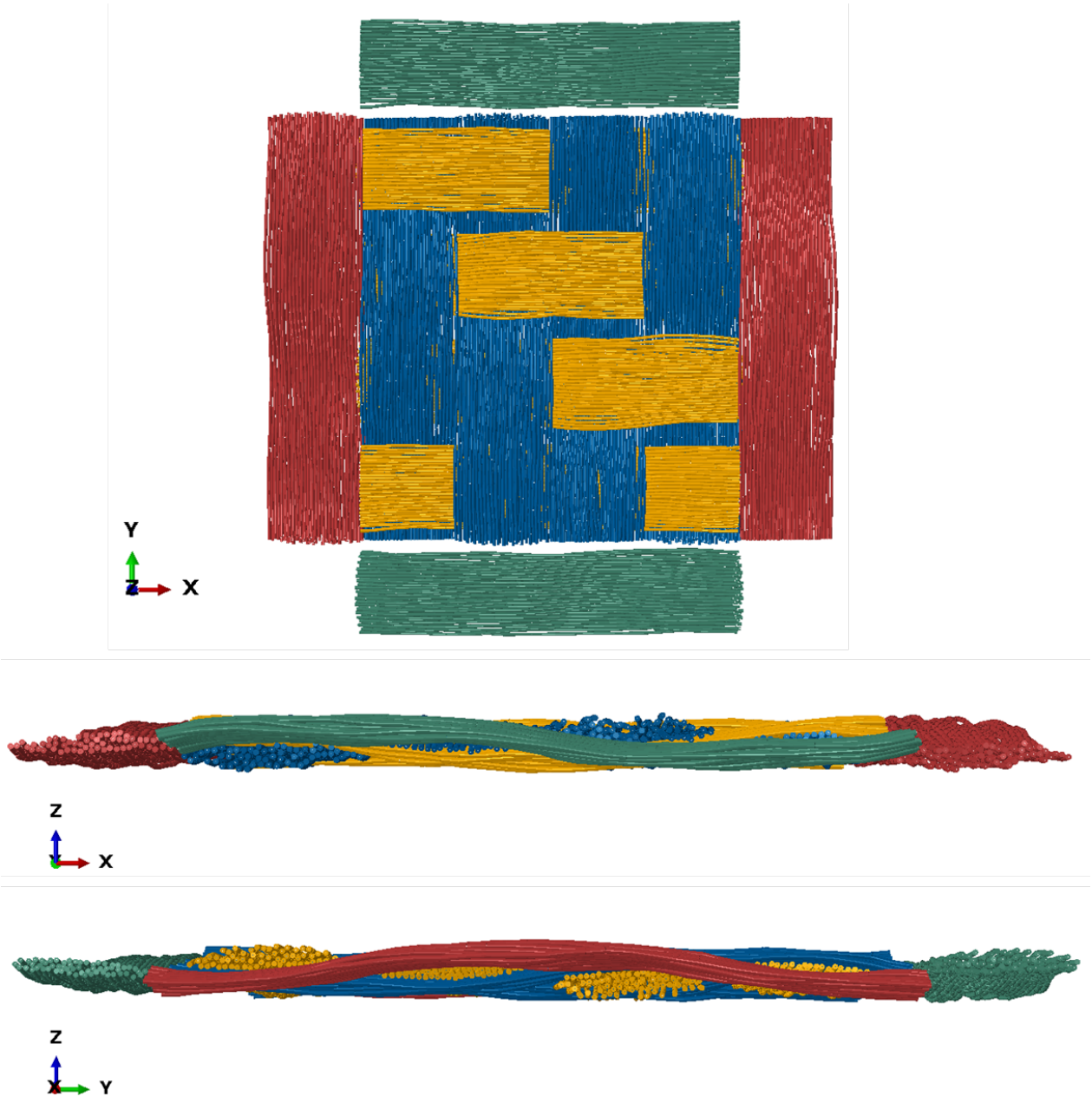

Figure 3.8: The basic truss fabric model (61 fibres per yarn) by Daelemans in its deformed, as-woven state. The warp yarns (X-direction) are yellow, the weft yarns (Y-direction) are blue. The green and red slave yarns have an artificially reduced Young's modulus.

After this update, the main change to the truss model was due: the superposition of beam elements on top of the truss elements. The ABAQUS input file editor was expanded to detect where elements are created and where sections are defined for those elements. This is because ABAQUS works in two stages to create a structural element: first, the element is created between certain nodes and is assigned an element type (e.g. truss, beam). Only after that are its properties defined in a section (solid section for trusses, beam section for beams). In the input file editor, the first stage is realised by creating an extra element for each time it detects a fibre being discretised into truss elements. It creates this extra element as a B31 beam element between the same nodes of the "truss fibre" node set, but as part of a separate "beam fibre" element set instead of the corresponding "truss fibre" element set. To then apply properties to these beam elements (stage 2), beam sections are defined below the already present solid (truss) sections. They are characterised as circular sections with the radius calculated in table 3.2, depending on the amount of virtual fibres per yarn. For ease of programming, they are assigned the same material as the slave yarns, as it was established that they need the same properties as the actual unit cell yarns, but with a Young's modulus lowered by two orders of magnitude, exactly like the slave yarns. Again, the Python script functions by copying all identical lines into a new input file but modifying non-identical lines where necessary. A version of the completed model is shown in figure 3.9.

In this superposition process, beam elements were not superimposed on top of the slave yarns, as these don't require a flexural rigidity: their deformation should follow the deformation of their master yarns without influencing that deformation, which was the original reason for their reduction in Young's modulus. Their sole purpose is to provide contact interactions for periodicity. On that note, no new contact interactions were defined for the beam elements: these serve only to provide a flexural rigidity and are not accurate representations of the real fibre dimensions - their radius is larger than the actual virtual fibre radius should be. To show that the beams exist but have no contact interaction with the trusses, a test model was created with hugely oversized beams. As can be seen in figure 3.10, the oversized beams result in a less tightly-woven fabric structure, meaning they apply a very large resistance to bending (flexural rigidity). At the same time, they also clip into each other as desired. The truss elements do represent the actual fibre dimensions and do not clip into each other.

Note that the truss elements as defined by Daelemans were left unchanged in the superposition of the beam elements, though their sections should have been updated with the cross sectional areas presented in table 3.1.

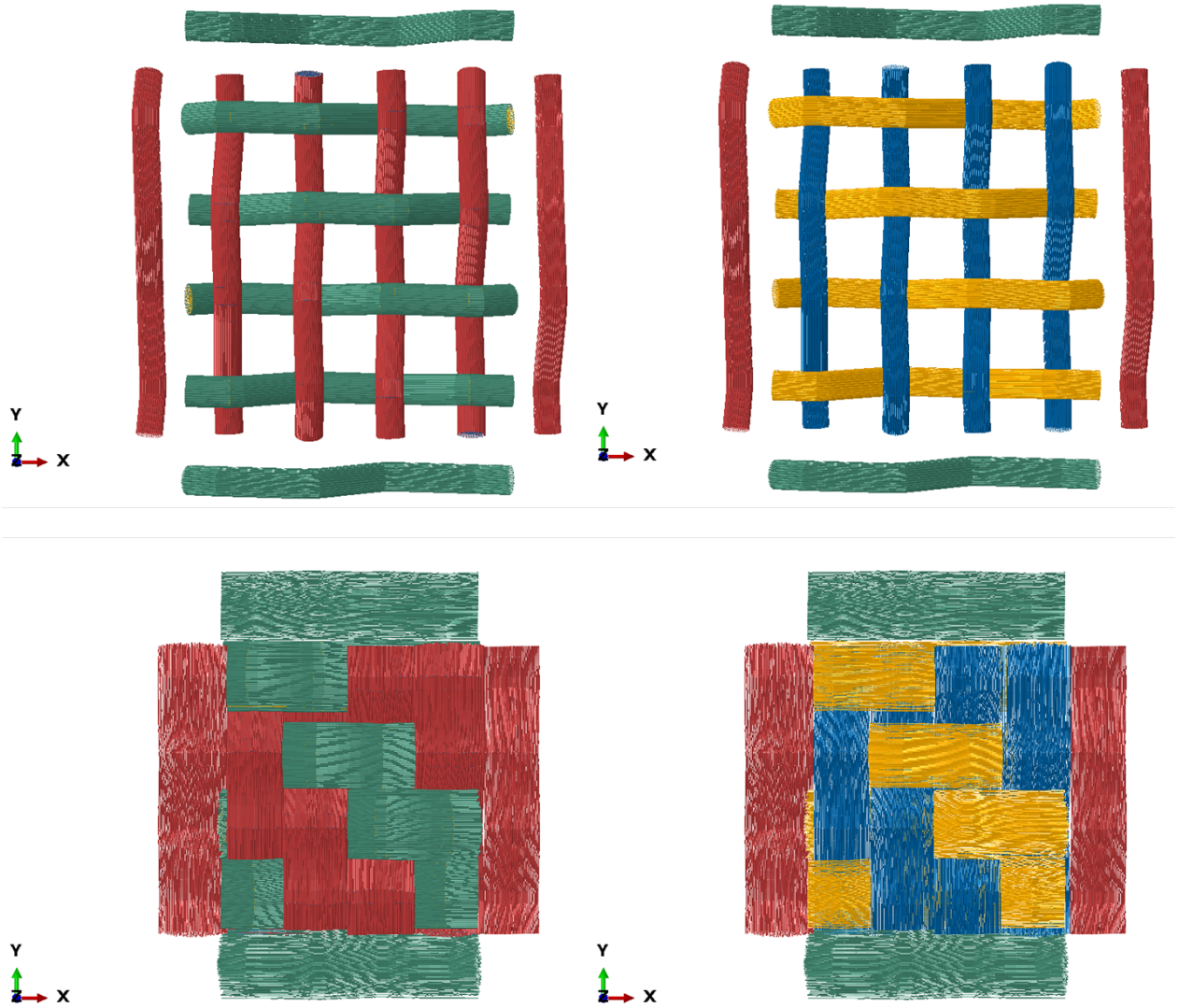

Figure 3.9: The combined truss-and-beam fabric model (127 fibres per yarn) in its undeformed state (top) and its as-woven state (bottom). The truss elements, representing the real fabric geometry, are yellow in the warp direction (X-direction) and blue in the weft direction (Y-direction) (right). The beam elements, only contributing their flexural rigidity, are made from the same material as the slave yarns with an artificially reduced Young's modulus and are coloured green in the warp direction (X-direction) and red in the weft direction (Y-direction) (left).

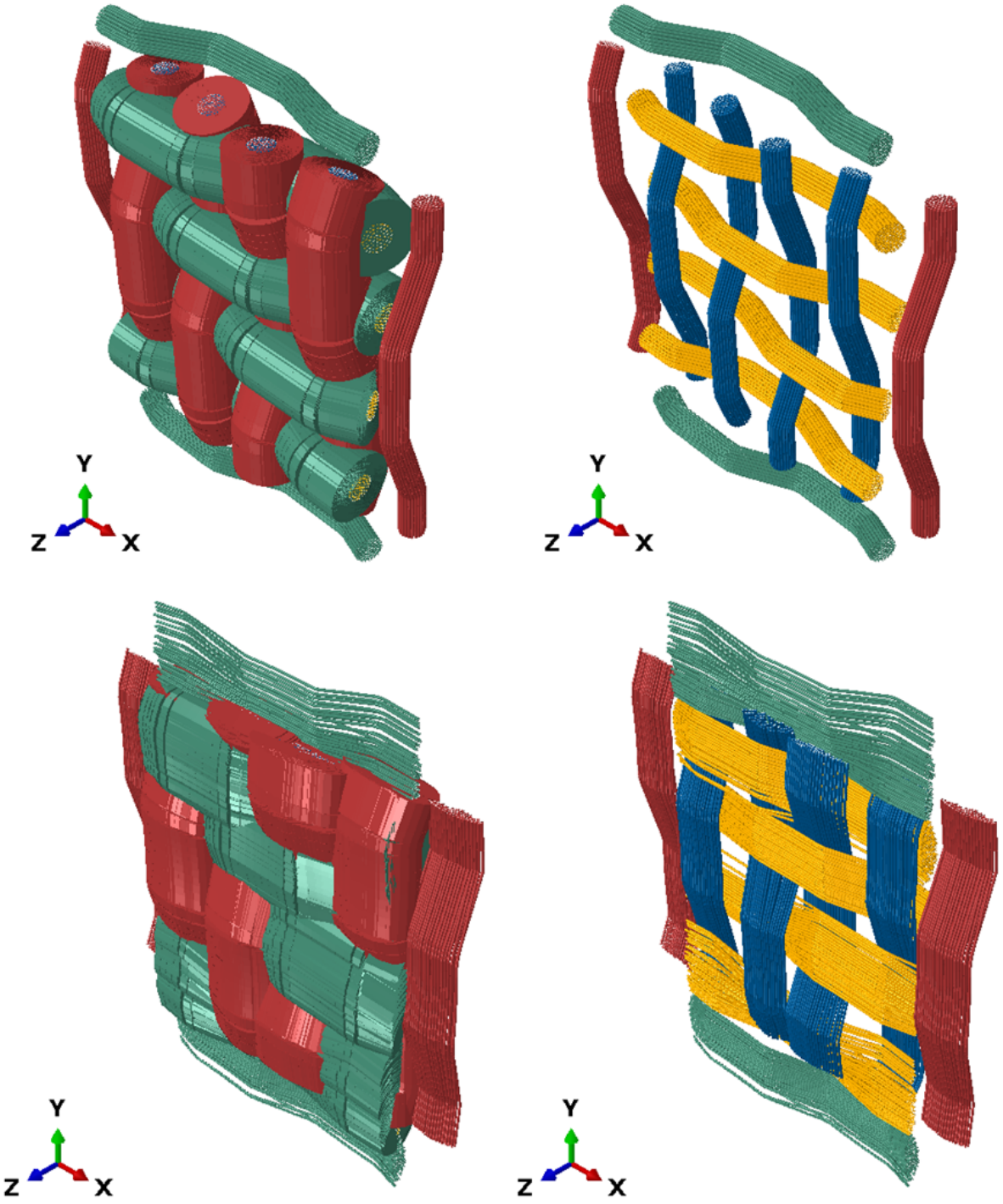

Figure 3.10: The combined truss-and-beam fabric model (61 fibres per yarn) with oversized beam elements in its undeformed state (top) and its as-woven state (bottom). The truss elements are coloured yellow and blue (right) while the beam elements are coloured green and red (left). It is clear that the beams contribute to the flexural rigidity of the fabric because the as-woven state is much looser but at the same time do not constrict node movement through contact interactions.

Chapter 4

Fabric model validation

To validate the created truss-and-beam fabric model, the final yarn widths of its deformed, as-woven state were compared to yarn widths found in the real, woven glass fibre fabric. The distances in the digital model were measured as described in subsubsection 2.2.1.2. The distances in the real fabric were first visualised by taking µCT-scans of the fabrics, and then measuring distances on the µCT images as described in subsubsection 2.2.2.2. These scans came from the two experimental compression tests, before any consolidation pressure was applied.

4.1 µCT image quality

Originally, only compression test 1 was planned in this dissertation. When the µCT-scans of that test were received, however, the image quality was much lower than expected due to three factors: resolution, noise and contrast. The resolution was low because a voxel size of 15.525 µm was obtained whereas previous scans at the UGCT had achieved voxel sizes between 9 and 10 µm. One goal of the scans was to image individual fibres in every voxel, but as the voxel size was larger than the fibre diameter, this was impossible. Additionally, there was a lot of noise on the image, which made it very difficult to determine the correct boundaries between warp and weft yarns, and even between the yarns and the surrounding air. This was not helped by the fact that the contrast on the image was not very strong; see figure 4.1. To make use of the data but take the inaccuracy into account, an extra error margin of 4 voxels (62.1 µm) was added to the standard deviation of any measurements performed on experiment 1's µCT image data.

In an attempt to improve the image quality, many parameters were investigated. It was argued that the most influential contributors to the image quality reduction were the PEEK jaws around the Deben cell, the sample size and the materials used within the sample itself. The PEEK jaws will always absorb some X-rays during scanning and thus interfere with proper imaging. Garcea et al. proved that sample size is a limiting factor in the maximum resolution of a µCT image, though mechanical behaviour is also affected by sample size, so simply reducing sample size may cause the sample to no longer be representative for the real fabric [127]. Finally, it is known that contrast in X-ray images is formed by the materials in the sample having different X-ray absorption coefficients, which are correlated to material density and atomic number [127, 128].

Using this knowledge, a second experiment was designed. To replace the PEEK jaw material, less absorbing materials such as polyethylene or polypropylene foams were suggested, but in the end it was decided to remove the Deben cell altogether and opt for pre-loaded samples over continuous loading during scanning. To reduce the "sample size", the scanning area of the µCT-scanner was reduced without making physically smaller samples. This kept the samples large enough to be representative for the entire fabric, as long as at least one central unit cell was accurately scanned. Concerning the used materials, thought was given to using hybrid fabrics, where the warp yarns and weft yarns are made of different materials. A carbon fibre/glass fibre fabric, for example, would increase contrast between warp and weft yarns because carbon has a lower density than E-glass (approximately 1800 $\frac{\text{kg}}{\text{m}^3}$). Even more extreme cases would concern hybrid fabrics with high molecular weight polypropylene (HMWPP) (density of approximately 840 $\frac{\text{kg}}{\text{m}^3}$) or UHMWPE (density of approximately 970 $\frac{\text{kg}}{\text{m}^3}$). This idea of using hybrid fabrics was eventually abandoned as that fabric would no longer represent the fabric that the truss-and-beam model was modelled after. This all led to the development of compression experiment 2, as described in subsubsection 2.2.3.2.

When the µCT images for compression experiment 2 were received, the image quality appeared to not be much better after all; see figure 4.1. The contrast with the surrounding matrix and the resolution (voxel size of 10 µm) were better, but there was still a lot of noise and the warp and weft yarns were possibly even more indistinguishable. The exact reason for this has not yet been found, but it is assumed that X-ray absorption by the resin used to keep the fabric in place plays a small role, as does the noise filtering applied to the image reconstruction. To use the data from these images, an arbitrary extra error of 3 voxels (30 µm) was added to the standard deviation of any measurements.

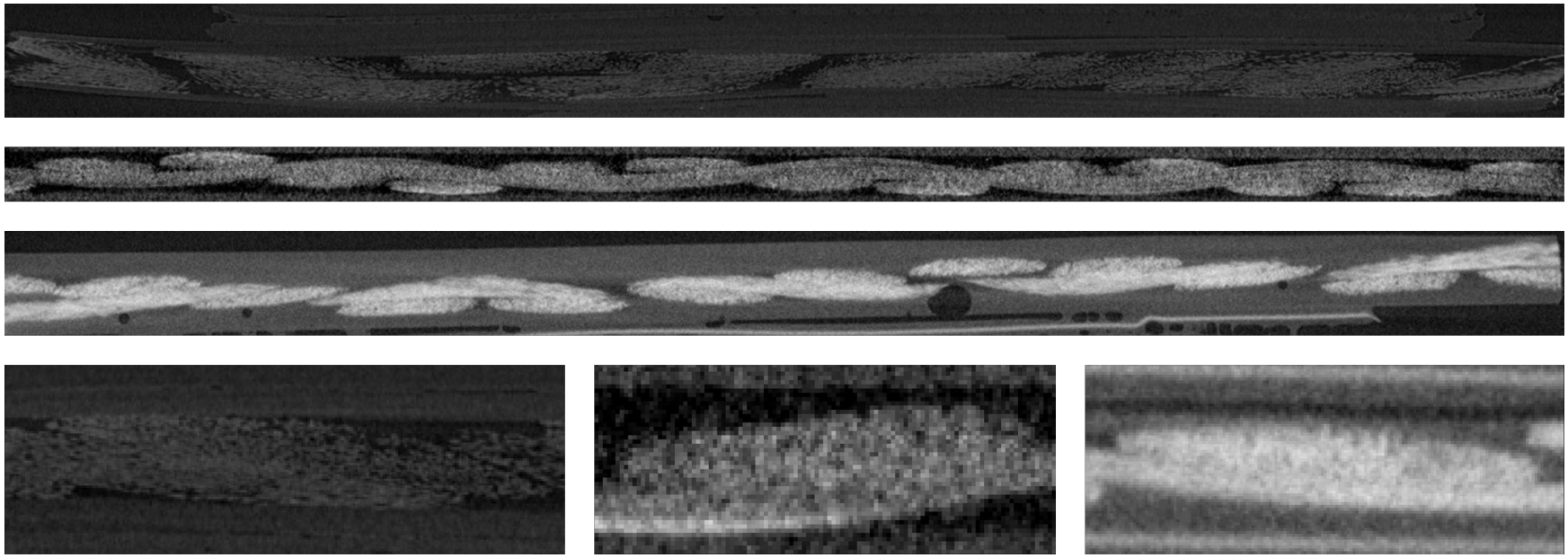

Figure 4.1: A comparison of the µCT images of single layers of glass fibre fabric. Previous scans at the UGCT provided images with very high resolution, where every fibre is visualised individually, even if the contrast is low (top/left). Scans of experiment 1 showed very low resolution and high amounts of noise (middle/middle). Scans of experiment 2 had a better resolution and contrast with the matrix material, but lower contrast between yarns and almost equally much noise (bottom/right).

4.2 Influence of the model parameters

With the measuring of yarn widths from numerical models and their comparison to available experimental (if somewhat inaccurate) data, several parameters of the truss-and-beam model were investigated: the coefficient of friction, the time step, the weaving process and the number of fibres per digital yarn. To easily change the first two parameters in between simulations, the ABAQUS input file editor, as given in appendix A, was expanded.

The first parameter examined in the search for the most accurate fabric model was the coefficient of friction, which is a measure for the interfibre friction. The higher this coefficient gets, the more interfibre slippage is hindered, making the fanning out of fibres more difficult and thus leading to more compact yarns. This friction coefficient was numerically calculated by Daelemans to be 0.18 but was implemented in their truss model as 0.15 in the models with 61 or 91 fibres per yarn, and as 0.20 in the model with 127 fibres per yarn. In all cases, the yarn widths measured in the truss-and-beam model at a friction coefficient of 0.15 or 0.20 were lower than those measured experimentally, so simulations of the weaving process were run with reduced coefficients of friction (0.15, 0.10, 0.05 and 0.00). The results are shown for the 61, 91 and 127 fibres per yarn models in figures 4.2, 4.3 and 4.4, respectively. In all cases, the yarn width increased with decreasing coefficient of friction, and with the exception of the weft direction for the 91 fibres per yarn model, all cases also showed that the yarn width becomes more variable (larger standard deviation). This all supports the explanation of the coefficient of friction: as it is reduced, fibres fan out more easily and yarn cross sections get larger but also more irregular.

These results also serve as insight into the effect of the amount of fibres per yarn. If the warp yarns across figures 4.2, 4.3 and 4.4 are compared, it is noticeable that the simulated yarn width increases with increasing amounts of fibres per yarn, even though each yarn has the same total cross sectional area contained in its constituent fibres. Additionally, the yarn width variability increases, especially in the case of the model with 127 fibres per yarn. This is even more apparent when comparing the weft yarns. The reason for this behaviour is similar to that of the friction coefficient: fibres with smaller diameters (more fibres per yarn) can migrate out of the yarn more easily and cause a general fanning out of the yarn. Even the maximum modelled amount, 127 fibres per yarn, is nowhere near the real amount of fibres per yarn (2314.28 in the warp direction and 1840.74 in the weft direction, as calculated in section 3.2), meaning digital fibres will always lead to an underestimation of yarn widths.

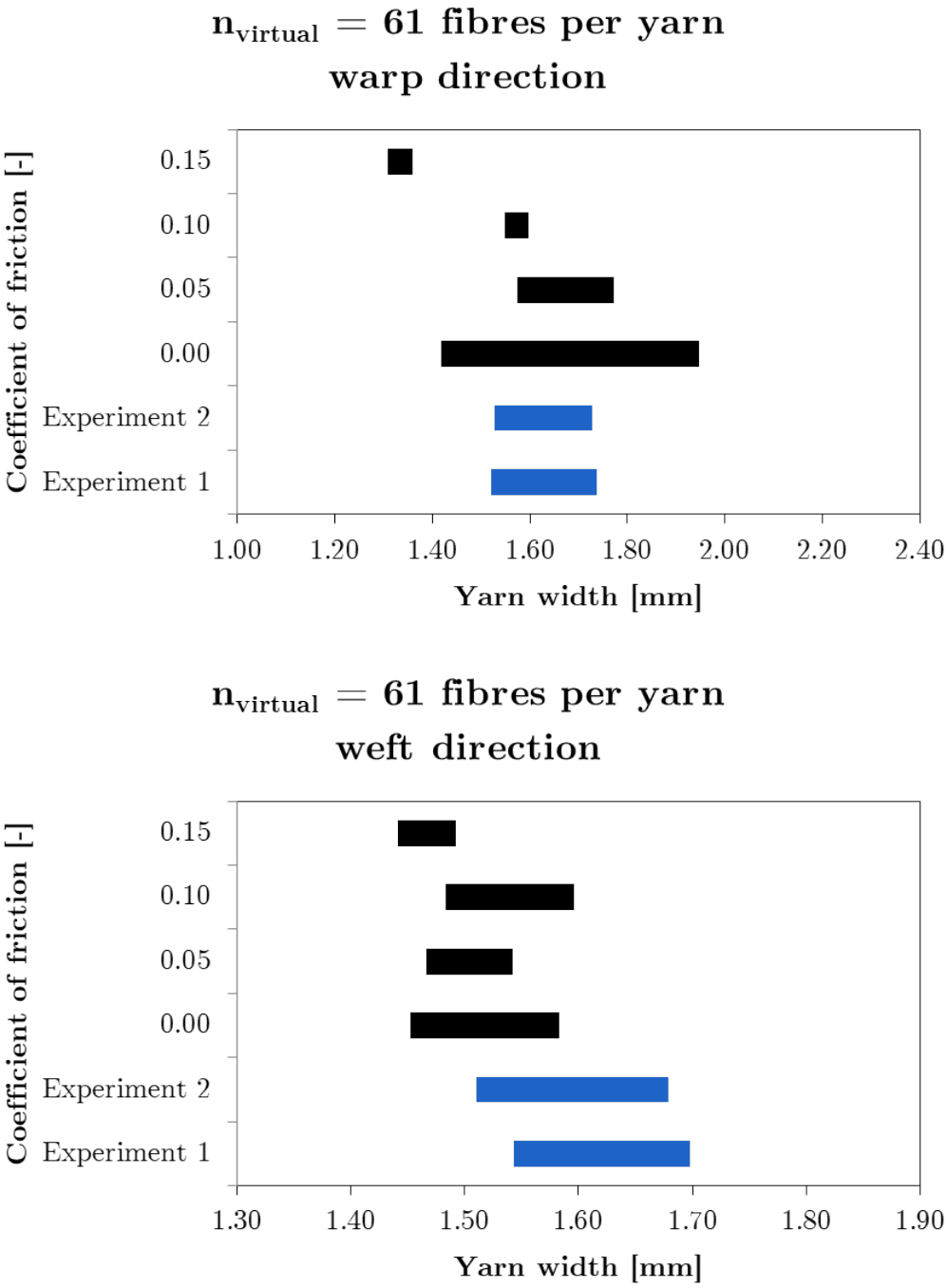

Figure 4.2: The influence of the coefficient of friction on warp (top) and weft (bottom) yarn width in the truss-and-beam model with 61 fibres per yarn. The time step for weaving is set at 0.040 s and the two-stage weaving process is used. Note that the X-axes do not start at 0 mm. The bars shown encompass the average yarn width and one standard deviation along either side.

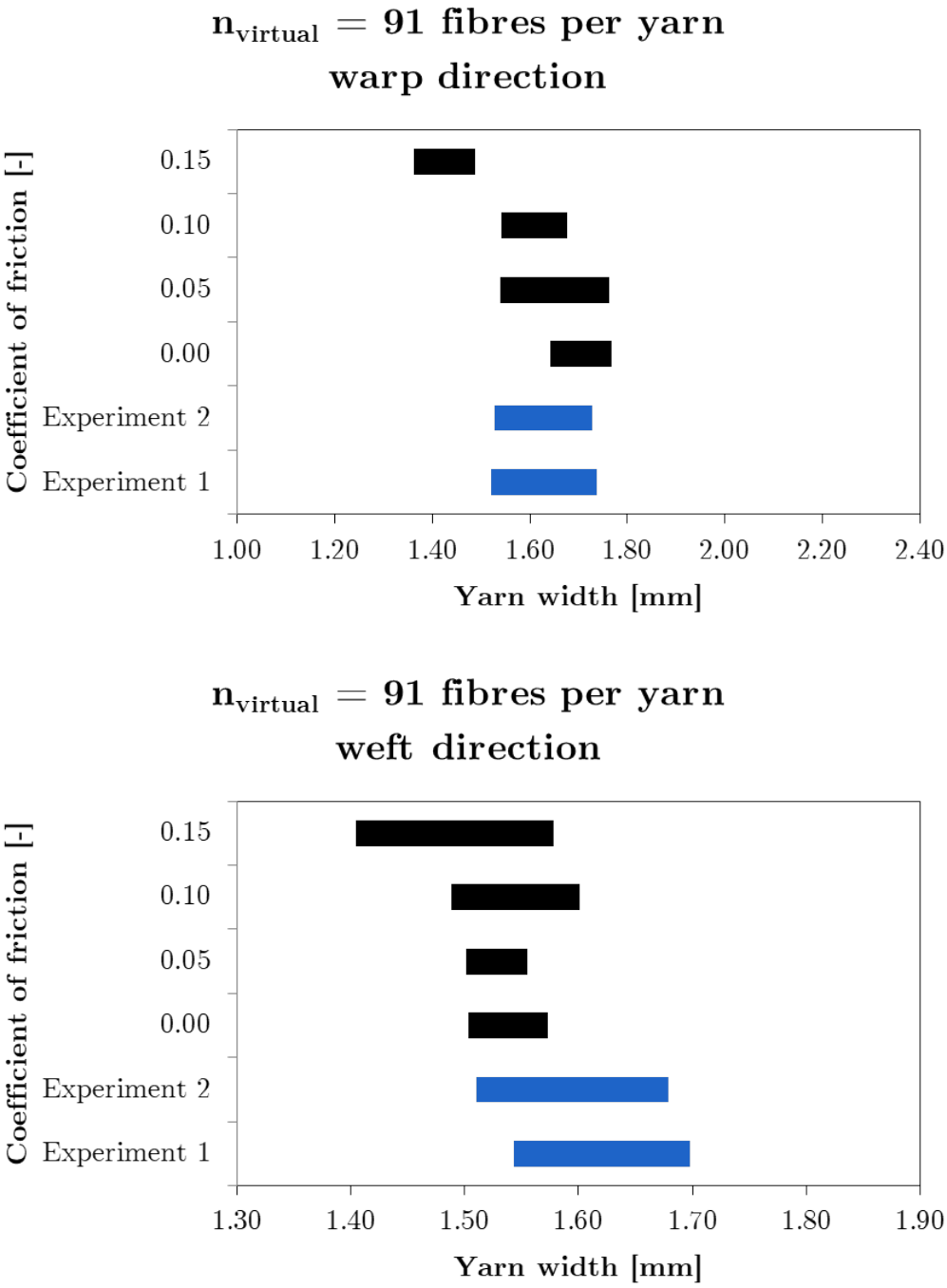

Figure 4.3: The influence of the coefficient of friction on warp (top) and weft (bottom) yarn width in the truss-and-beam model with 91 fibres per yarn. The time step for weaving is set at 0.040 s and the two-stage weaving process is used. Note that the X-axes do not start at 0 mm. The bars shown encompass the average yarn width and one standard deviation along either side.

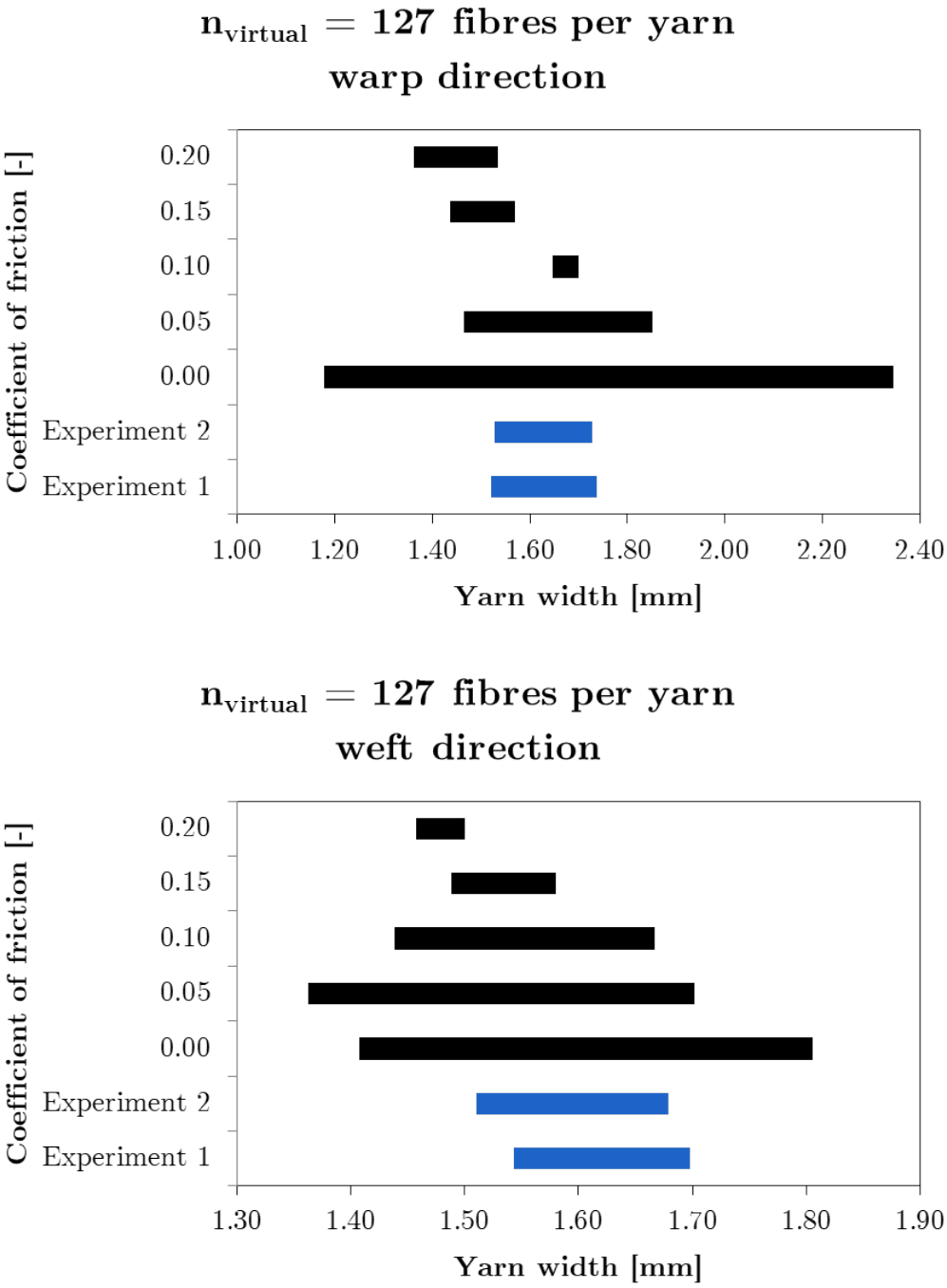

Figure 4.4: The influence of the coefficient of friction on warp (top) and weft (bottom) yarn width in the truss-and-beam model with 127 fibres per yarn. The time step for weaving is set at 0.040 s and and the two-stage weaving process is used. Note that the X-axes do not start at 0 mm. The bars shown encompass the average yarn width and one standard deviation along either side.

Another crucial parameter is the time step. This is the amount of time ABAQUS is given to perform the desired loading or deformation - in this case the weaving process. Note that it is not the computation time taken by the program (the time the user has to wait for results after submitting a job) but rather the time used in internal calculations. For example, if a part is modelled to move constantly at 1 $\frac{\mathrm{m}}{\mathrm{s}}$ and the time step is 5 s, the part will displace 5 m, even if ABAQUS takes 3 hours to compute this displacement. Results of simulations given different time steps are displayed in figures 4.5 and 4.6. It seems that increasing the time step leads to more variable yarn widths, without clearly increasing or decreasing the size of the yarn cross sections. This may be a product of dynamic inertia effects during simulation.

As the ABAQUS/Explicit solver is used, inertia effects play a role in the deformation calculations, meaning node mass and displacement time are taken into account. This signifies that the distinction between dynamic and quasi-static simulations becomes important. If a simulation is dynamic, the exact time step is very influential, as a small change in time step can have a large effect on the calculations: increasing the time step greatly lowers the impact of dynamic effects on the calculations, while decreasing it does the opposite. If a simulation is quasi-static, the time step is less influential and the calculations are more "robust". While it is difficult to determine whether a simulation is dynamic or quasi-static without running it multiple times at different time steps, a general idea can be formed by looking at the simulation's energy balance. Internal energy is the energy that is present as stresses inside the material, while kinetic energy is the energy spent to displace nodes at a certain velocity. A general rule of thumb dictates that if the internal energy is much larger (often a factor 5) than the kinetic energy, the simulation is considered quasi-static. If the kinetic energy is much higher than the internal energy, the simulation is considered highly dynamic. Figure 4.7 shows the energy balance for the truss-only model with 61 fibres per yarn, a time step of 0.04 s, a coefficient of friction of 0.15 and a two-stage weaving process, and compares that to the energy balance of the truss-and-beam model with the same parameters. No major changes are observed, except that both internal and kinetic energies are higher in the truss-and-beam model. Near the end of the simulation, the kinetic energy also surpasses the internal energy, becoming slightly less stable.

A much more pronounced effect is seen when comparing models that differ in the final investigated parameter - the weaving process. As discussed in subsection 3.3.1, the weaving process is split into two stages. In stage 1 the weaving itself is simulated and high shrinkage is applied, reaching a fabric crimp value below the measured experimental value. In stage 2,

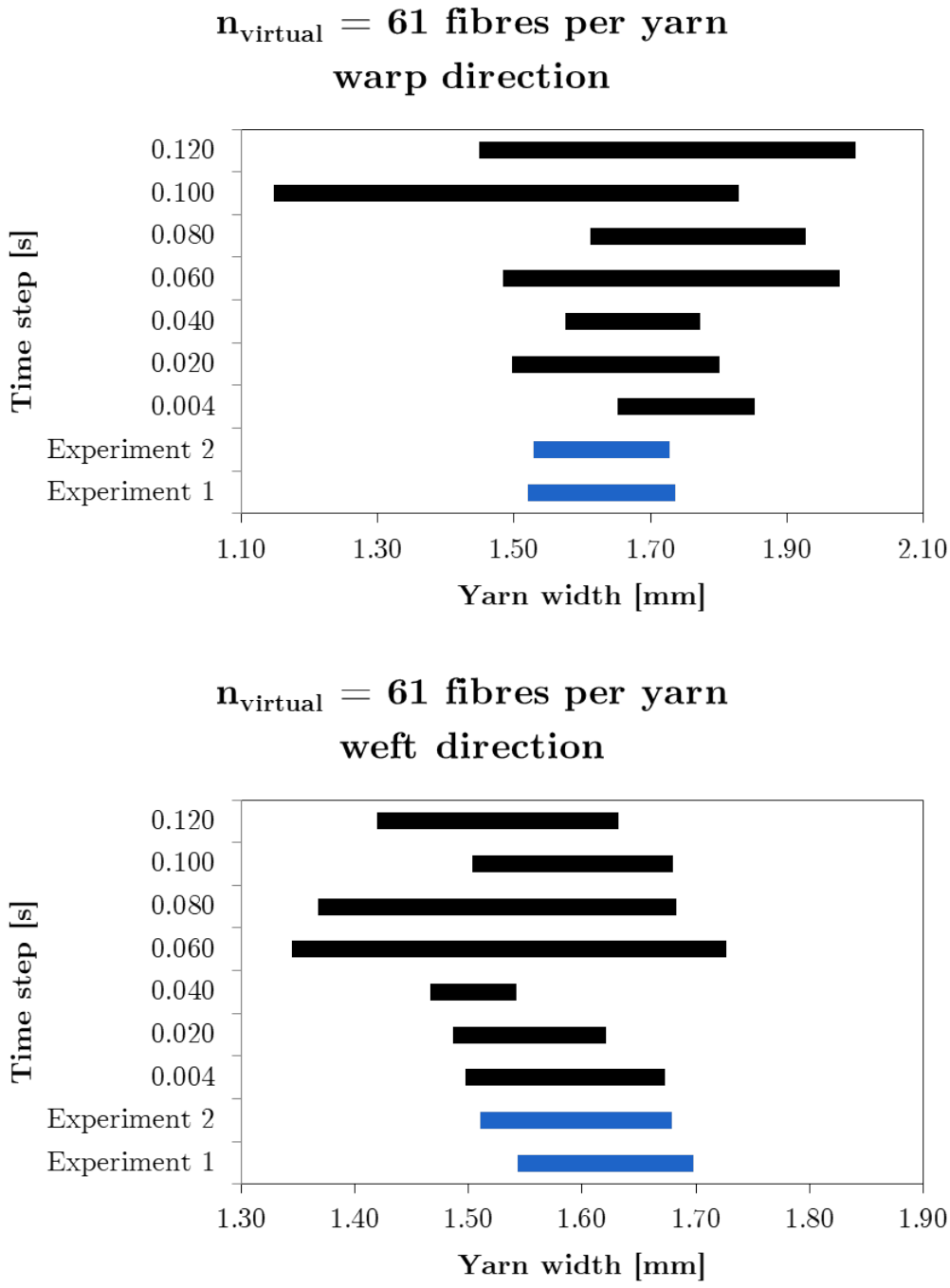

Figure 4.5: The influence of the time step on warp (top) and weft (bottom) yarn width in the truss-and-beam model with 61 fibres per yarn. The coefficient of friction is set at 0.00 and the two-stage weaving process is used. Note that the X-axes do not start at 0 mm. The bars shown encompass the average yarn width and one standard deviation along either side.

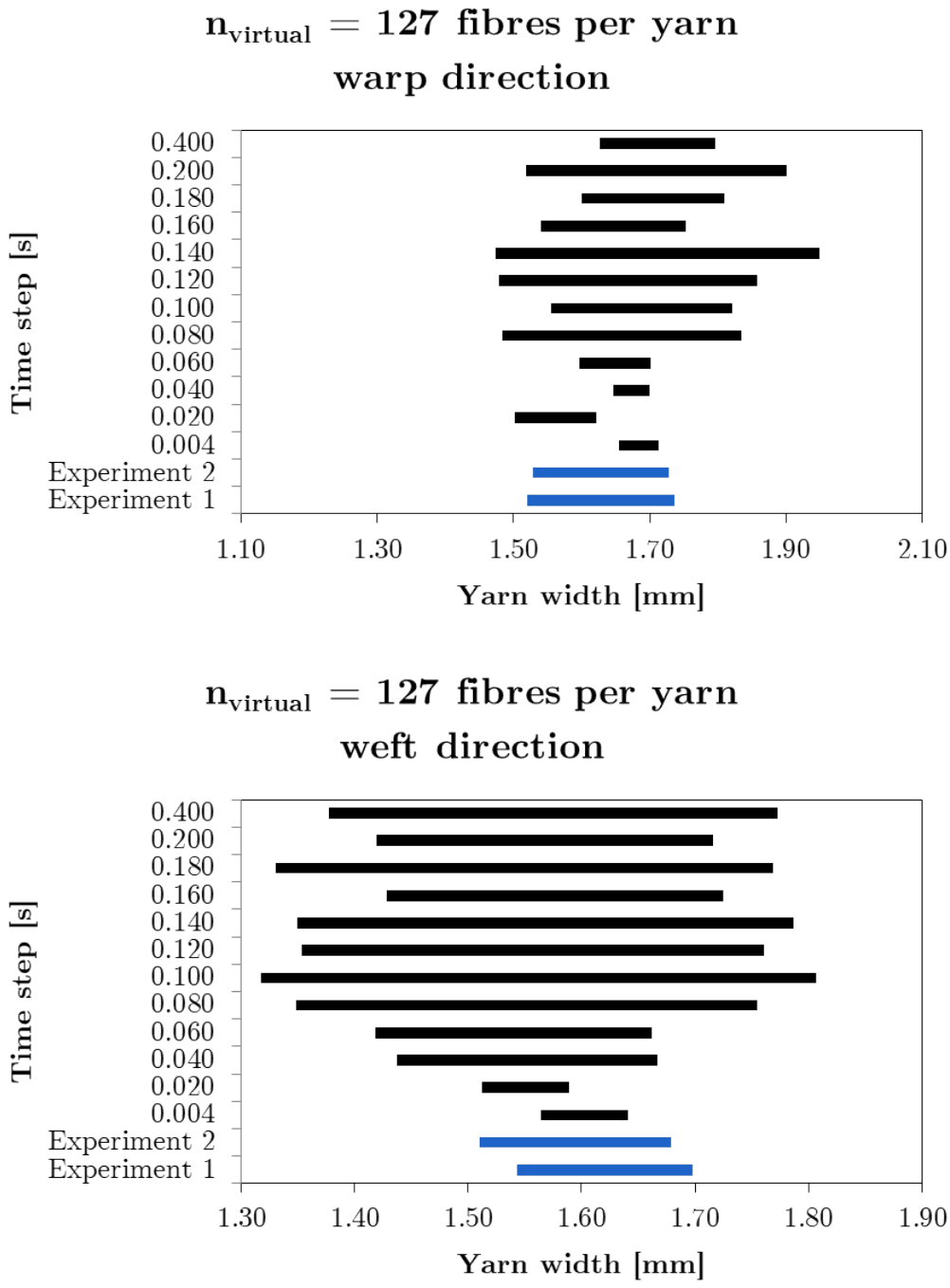

Figure 4.6: The influence of the time step on warp (top) and weft (bottom) yarn width in the truss-and-beam model with 127 fibres per yarn. The coefficient of friction is set at 0.10 and the two-stage weaving process is used. Note that the X-axes do not start at 0 mm. The bars shown encompass the average yarn width and one standard deviation along either side.

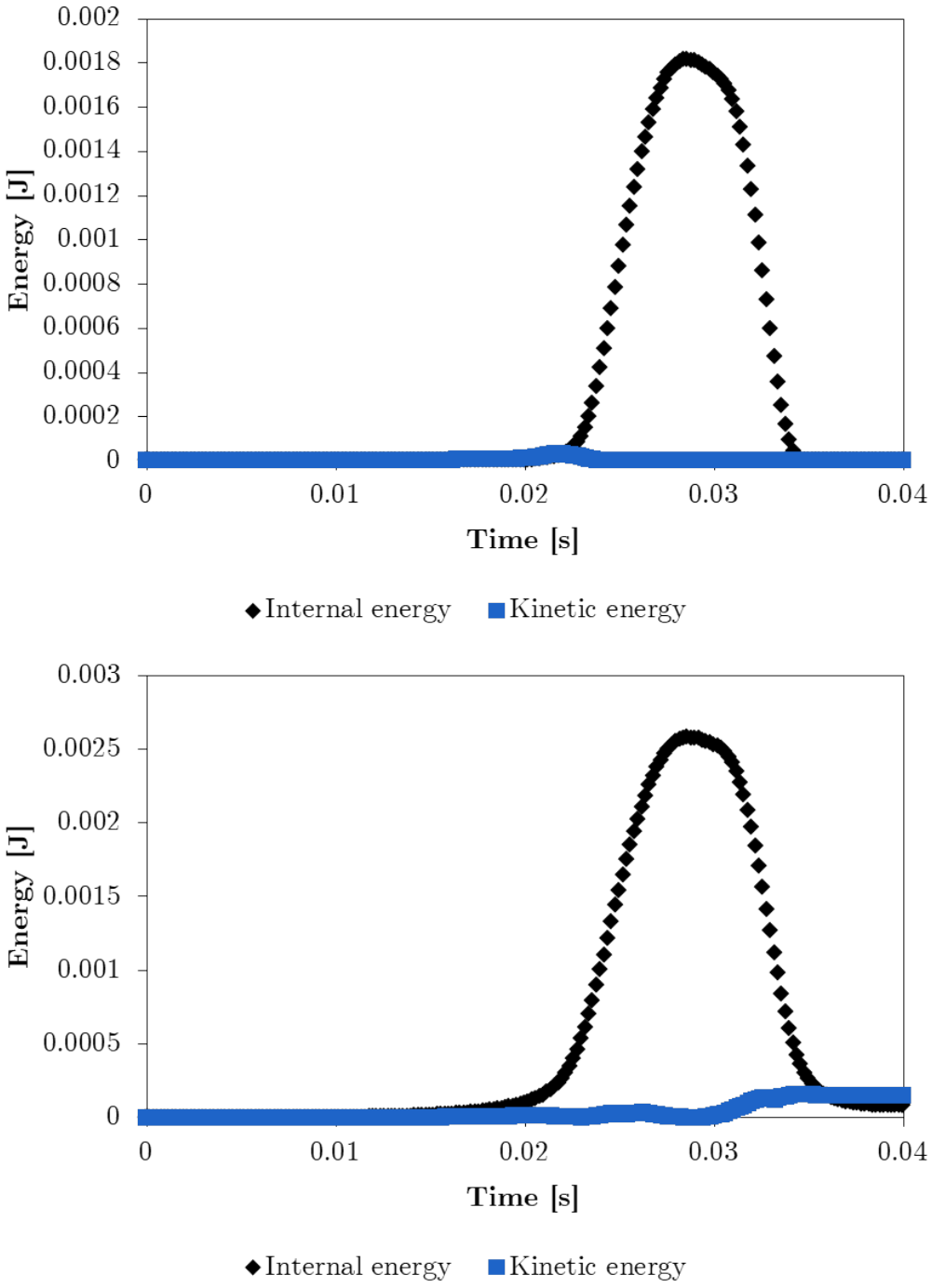

Figure 4.7: Energy balance for the weaving process of the truss-only model with 61 fibres per yarn, a time step of 0.04 s, a coefficient of friction of 0.15 and a two-stage weaving process (top), and the truss-and-beam model with the same parameters (bottom). The truss model is clearly quasi-static, as the internal energy is always higher than the kinetic energy. The truss-and-beam model remains mostly quasi-static, but becomes less stable towards the end of the simulation.

relaxation after weaving is simulated until the correct crimp value is reached. To investigate the effect of this two-stage process on the yarn width, simulations were run with a one-stage loading step, deforming immediately from the loose topology to the final as-woven state with the correct crimp value. In figure 4.8, an energy balance is given for two simulations at a high time step, that differ only in the number of stages of the weaving process. It is clear that, contrary to the quasi-static one-stage process, the more realistic two-stage process encompasses high kinetic energy and thus becomes a very dynamic simulation, requiring care to be taken with computation time optimisation, as any mass scaling and time step variation will have a significant impact on the obtained results. The yarn width results of similar simulations are displayed in figure 4.9. A general shift towards smaller yarn widths is found when two-step weaving is disabled, but the variability does not clearly increase or decrease. This shift corresponds to the behaviour observed by Daelemans in the truss model: disallowing relaxation leads to more stressed yarns, keeping fibres more stretched within their yarns and hindering migration.

In the end, a single fabric model had to be chosen to perform the consolidation simulation on. To emulate reality as closely as possible, the model with 127 fibres per yarn was chosen, and two-stage weaving was allowed (despite the dynamic simulation conditions). This provided as many fibres per yarn as possible and the most realistic weaving process, while keeping computation time reasonable. Considering the presented data on the influence of the model parameters, a coefficient of friction of 0.10 was chosen. For the time step, significant because of the dynamic nature of the simulation, three candidates were examined: 0.040 s, 0.060 s and 0.080 s. For each model, warp and weft yarn heights were measured and compared to experimental measurements from experiment 2; the image quality of the µCT-scans of experiment 1 was too low to accurately measure yarn heights. This served as a comparison between the three final models, but also as a validation of the models in a second measurement. The results are shown in figure 4.10. While the simulated yarn heights all seem low compared to the experimental results, the scale on the X-axis is much smaller than on previous graphs concerning the yarn widths. Coupled with the fact that the number of fibres per yarn is much lower than in reality and fanning out is thus hindered, the achieved yarn heights are correct within the required order of magnitude. Of the three examined models, the model with a time step of 0.060 s was chosen. Note that subjecting each yarn to the applied thermal shrinkage for 0.060 s can be compared to the frequency which real

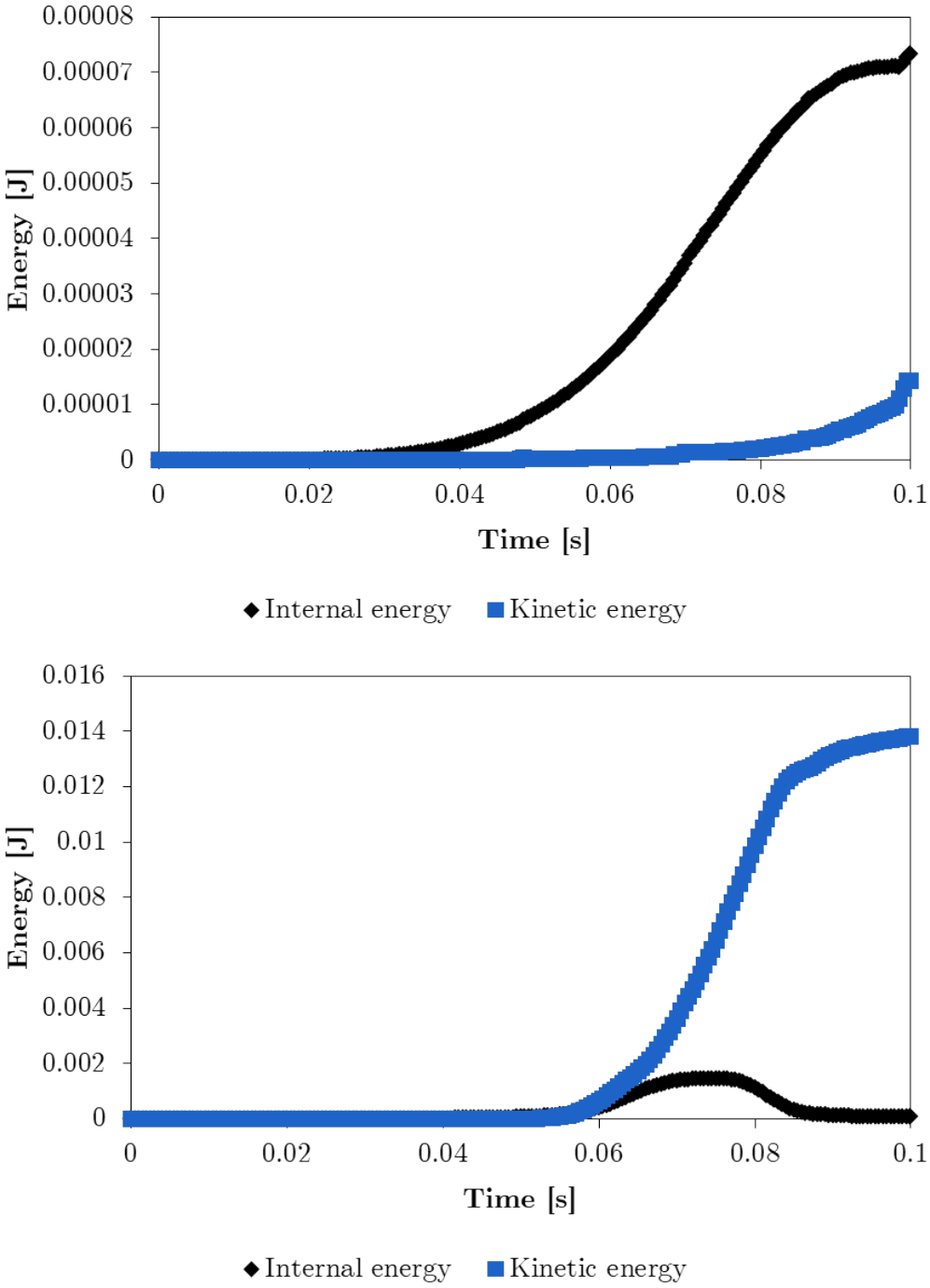

Figure 4.8: Energy balance for the weaving process of the truss-and-beam model with 127 fibres per yarn, a time step of 0.1 s, a coefficient of friction of 0.10 and a one-stage weaving process (top), and the same model with a two-stage weaving process (bottom). The one-stage weaving simulation is clearly quasi-static, as the internal energy is always higher than the kinetic energy. The two-stage weaving simulation behaves oppositely, becoming highly dynamic and more unstable at high time steps.

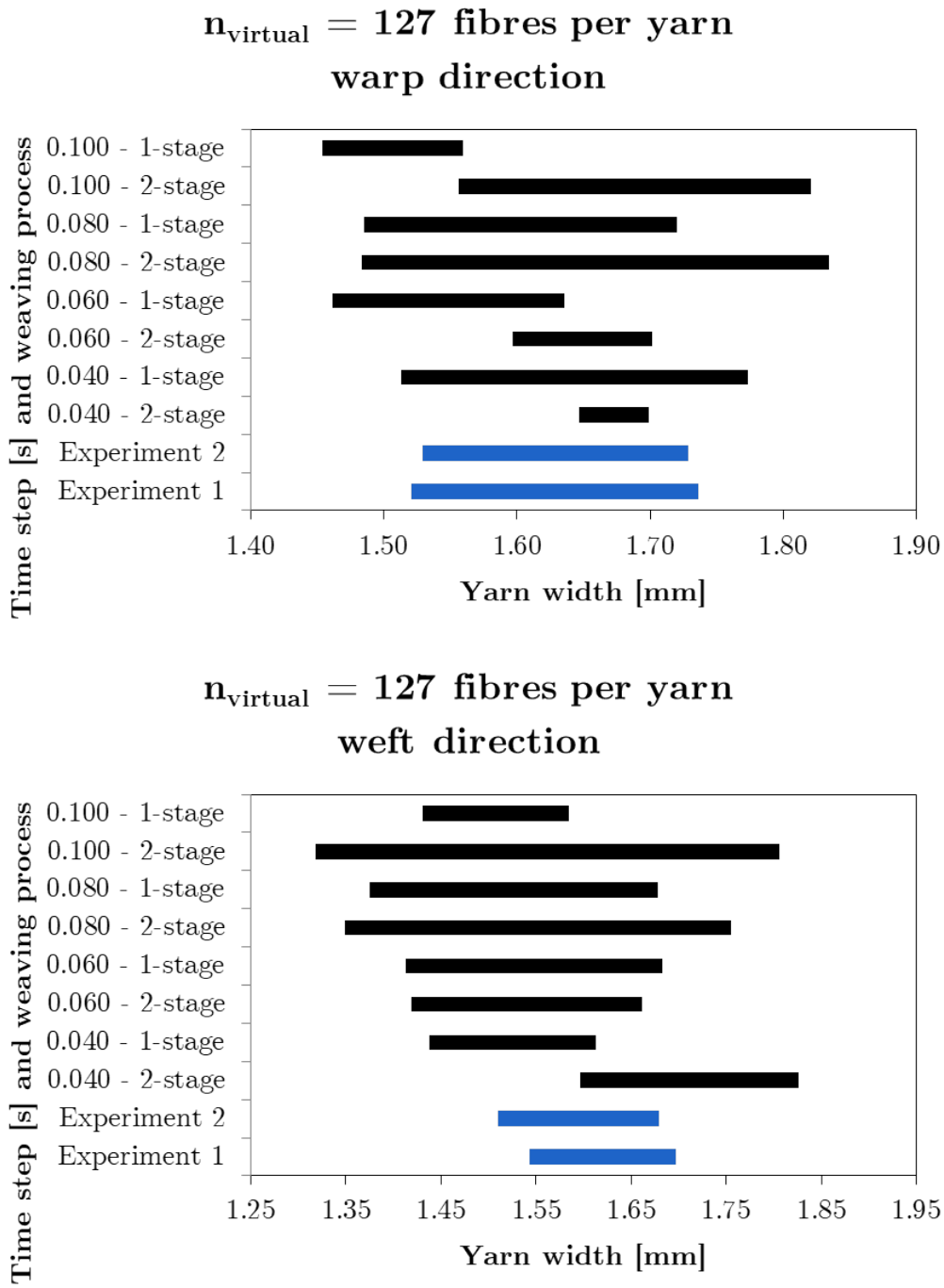

Figure 4.9: The influence of the one- or two-stage weaving process on warp (top) and weft (bottom) yarn width in the truss-and-beam model with 127 fibres per yarn. The coefficient of friction is set at 0.10. Note that the X-axes do not start at 0 mm. The bars shown encompass the average yarn width and one standard deviation along either side.

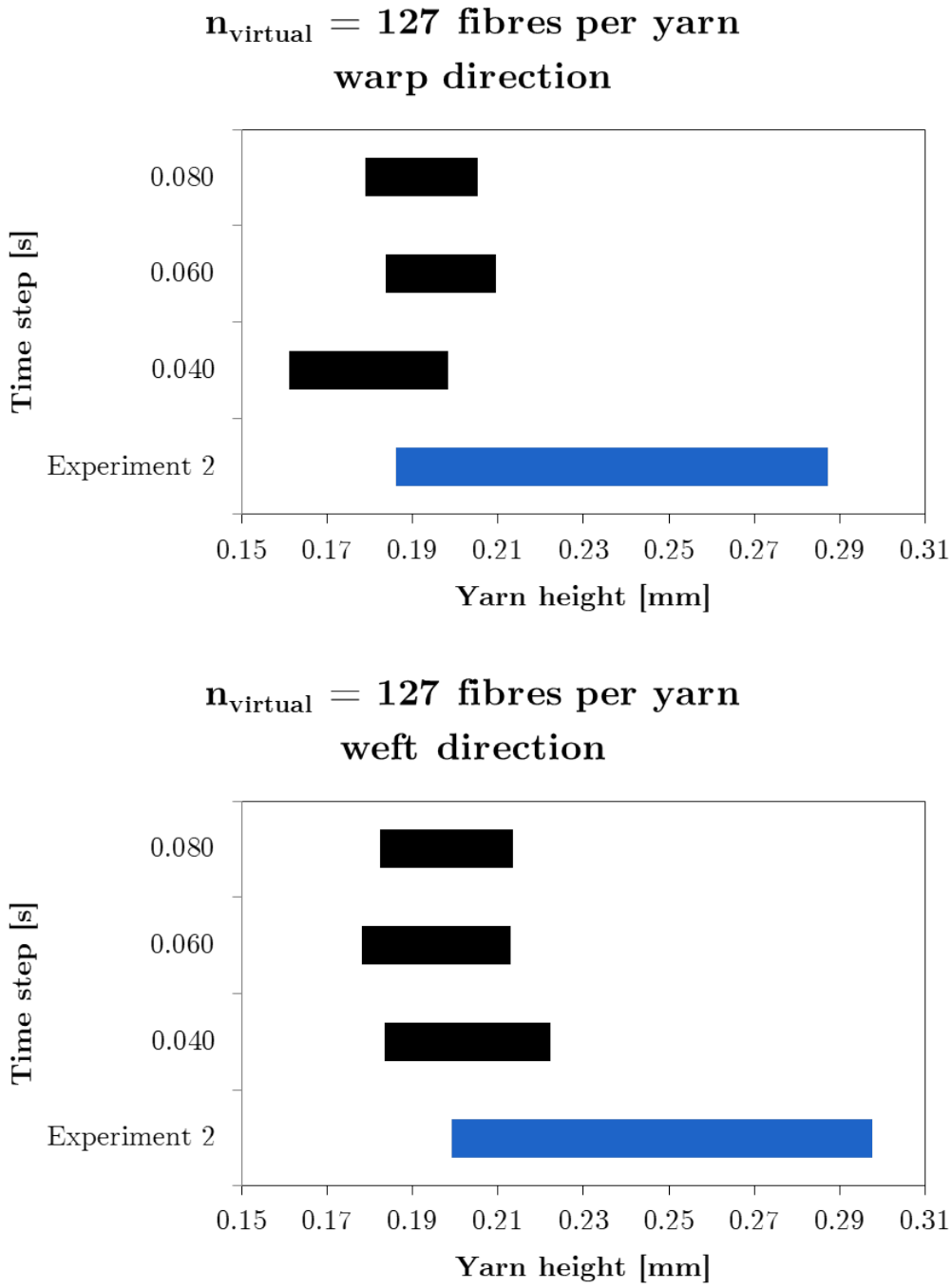

Figure 4.10: Validation of the truss-and-beam model with 127 fibres per yarn, a coefficient of friction of 0.10 and a two-stage loading process (relaxation allowed) via comparison of its warp (top) and weft (bottom) yarn heights with experimental data. Note that the X-axes do not start at 0 mm. The bars shown encompass the average yarn width and one standard deviation along either side.

weaving processes use:

$$\begin{aligned} weaving\ frequency &= \frac{1}{0.060\frac{s}{yarn}} \\ &= 16.67\frac{yarns}{s} \\ &= 1000\frac{yarns}{min} \end{aligned}$$

This corresponds very well to the weaving frequency of projectile, rapier and air-jet looms, all three of which are commonly used to weave glass fibre fabrics [136].

The chosen final model is shown during its weaving process in figures 4.11 and 4.12. This clearly visualises that the yarns are flattened and the cross-sections are deformed as thermal shrinkage is applied. In the relaxation stage of the process, the yarns spring back and some gaps are created in between the yarns, as the fabric increases in thickness. In figures 4.13 and 4.14, the cross sections of the digital warp and weft yarns are compared to the experimental µCT images of the real glass fibre fabric, respectively.

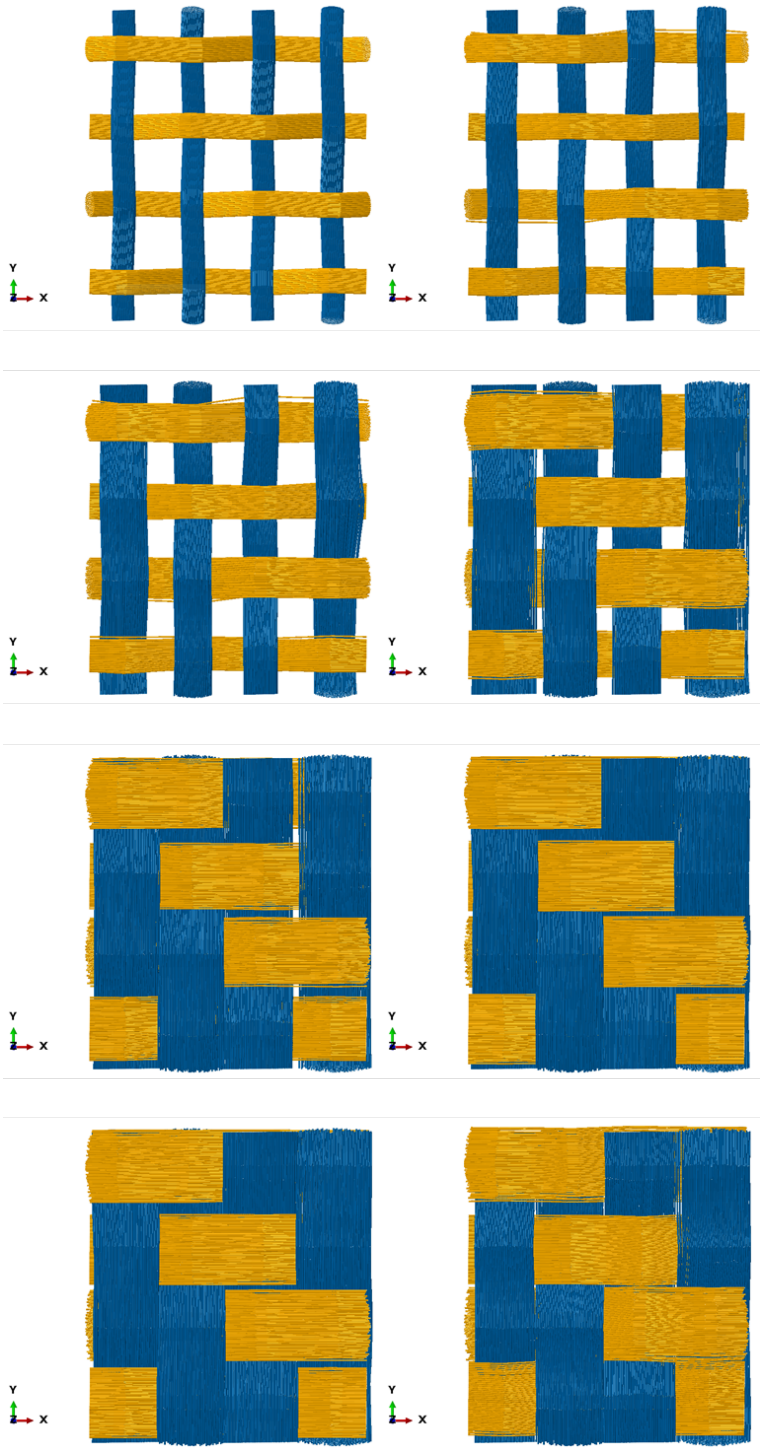

Figure 4.11: An XY-view of the final truss-and-beam model with 127 fibres per yarn and a coefficient of friction of 0.10, deformed from its loose topology state (top left) to its as-woven state (bottom right) in a time step of 0.06 s via a two-stage weaving process. Only the truss elements are shown, as they represent the fabric geometry. These are yellow in the warp direction (X-direction) and blue in the weft direction (Y-direction). Note the relaxation occurring between the last two images.

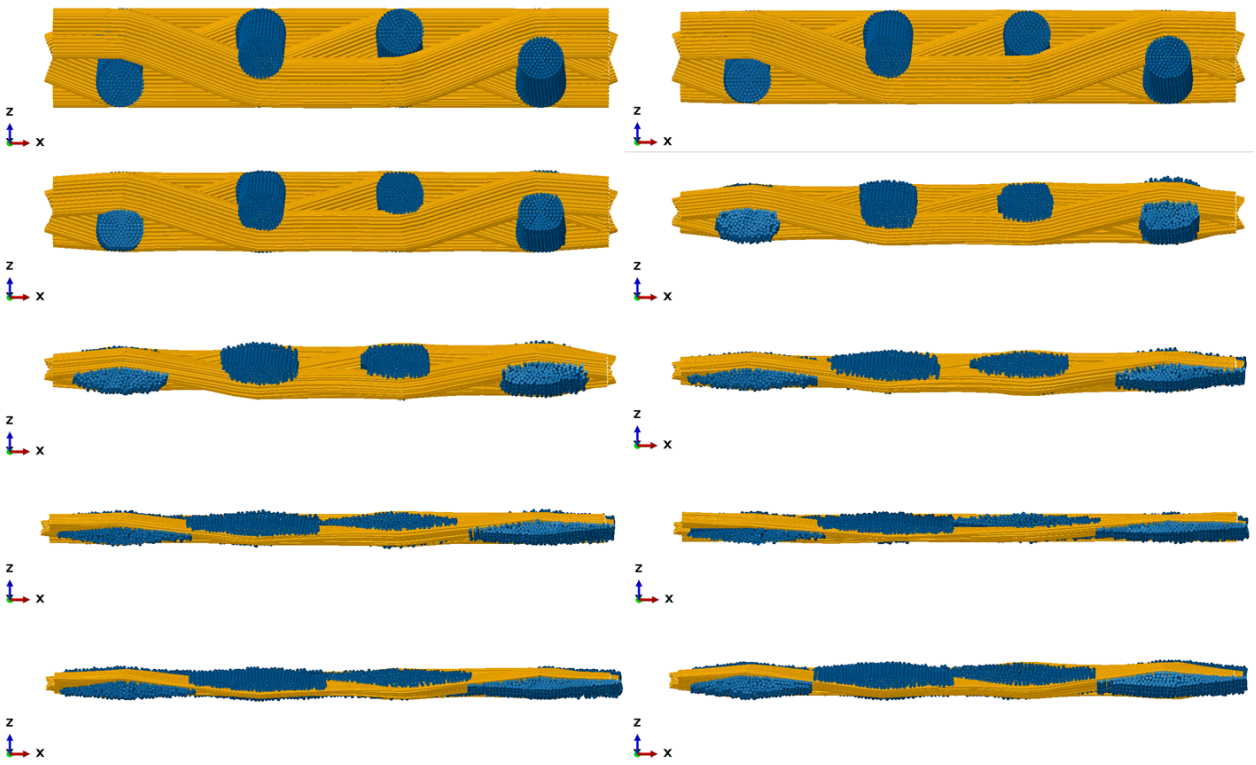

Figure 4.12: An XZ-view of the final truss-and-beam model with 127 fibres per yarn and a coefficient of friction of 0.10, deformed from its loose topology state (top left) to its as-woven state (bottom right) in a time step of 0.06 s via a two-stage weaving process. Only the truss elements are shown, as they represent the fabric geometry. These are yellow in the warp direction (X-direction) and blue in the weft direction (Y-direction). Note the relaxation occurring in the last two images.

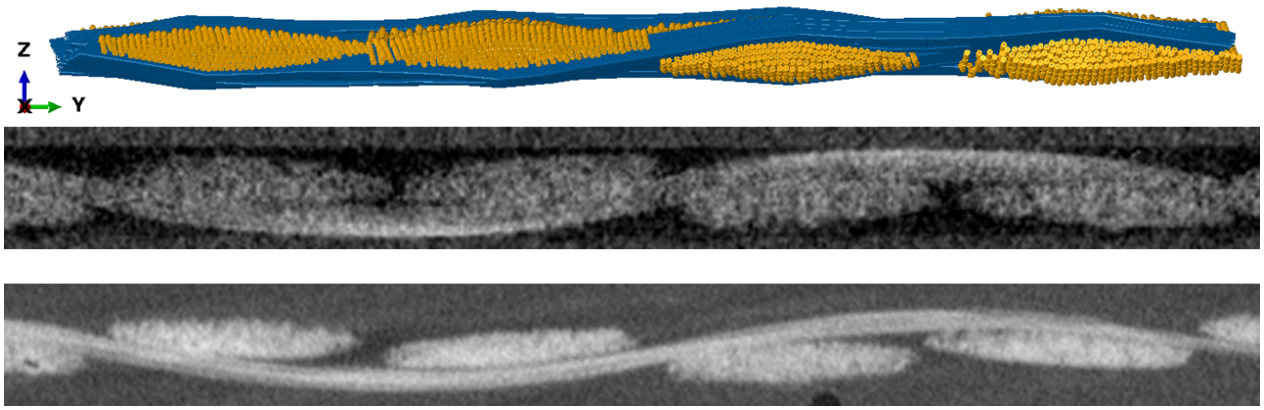

Figure 4.13: A YZ-view of the final as-woven truss-and-beam model with 127 fibres per yarn and a coefficient of friction of 0.10, deformed in a time step of 0.06 s via a two-stage weaving process. The cross sections of the warp yarns (yellow) are shown and compared to cross sections of warp yarns imaged via µCT-scanning in experiment 1 (middle) and experiment 2 (bottom).

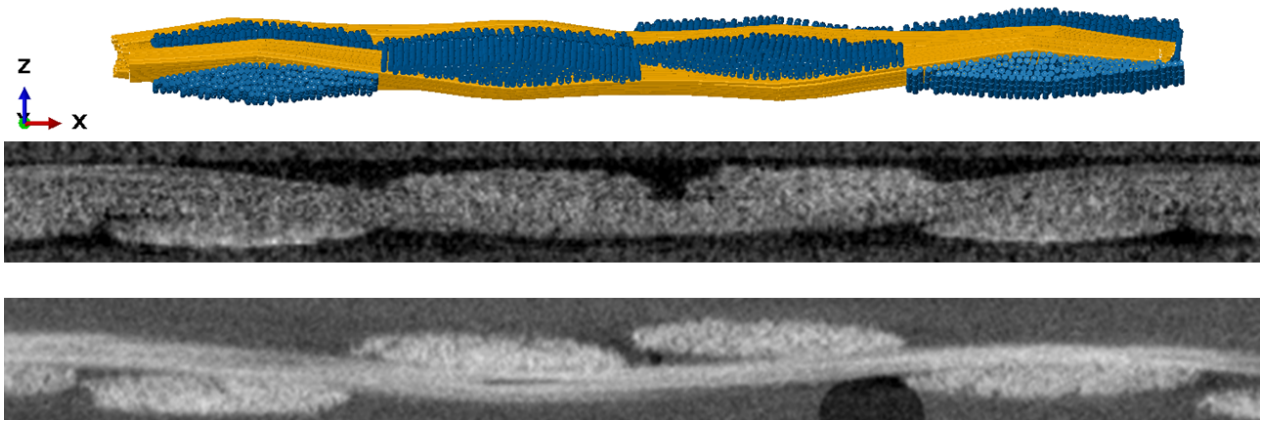

Figure 4.14: An XZ-view of the final as-woven truss-and-beam model with 127 fibres per yarn and a coefficient of friction of 0.10, deformed in a time step of 0.06 s via a two-stage weaving process. The cross sections of the weft yarns (blue) are shown and compared to cross sections of weft yarns imaged via µCT-scanning in experiment 1 (middle) and experiment 2 (bottom).

Chapter 5

Fabric consolidation

5.1 Experimental compression

In this dissertation, two compression experiments were carried out, as described in subsection 2.2.3. The first experiment, using continuous loading applied by the Deben cell, was always planned but turned out to result in low quality µCT images (see section 4.1). To achieve better results, a second experiment was designed, using static loading, but after viewing the µCT images, the quality was not judged to be much better. The time investment that would be necessary to measure and process all distances in these µCT images was not deemed worthwile for the minimal improvement in accuracy it could bring. As such, only the results from compression experiment 1 will be discussed in this section.

5.1.1 Machine and image data

As described in subsubsection 2.2.3.1, the Deben cell was able to apply pressure to the fabric samples continuously, but the µCT-scanning was discontinuous. To combine these two, the samples were subjected to compaction until a certain pressure was reached, at which the Deben cell maintained its position and the tomograph took a µCT-scan. After scanning was done, the compaction process was resumed, until a next threshold was reached, at which the Deben cell would again pause, and so on. The Deben cell was never actually turned off, and so measured the force it exerted and its own displacement continuously. At the same time, µCT-scans are available at discrete pressures, from which displacements can be measured as descibed in subsubsection 2.2.2.2, providing two different sources for the same data - so called machine and image data, respectively.

Logic dictates that the machine and image data must be the same, considering they measure the exact same parameters in one experiment. To compare them, the machine data was discretised to the pressures (or forces) the µCT-scans were taken at. For example, if a scan was taken at a force of 30 N, all measurements by the Deben cell around the measurement of 30 N (with an arbitrary limit, e.g. 29.6 N to 30.4 N) were averaged out. In each case, at least 5000 measurement points were combined, leading to very low standard deviations on the machine data. Note that the aimed at forces were never precisely reached. The 30 N threshold, for example, was actually a scan around 27.06 N.

The data provided by the Deben cell consisted of the force it exerted on the sample, and the distance between its PEEK clamps. The latter was calibrated by first compressing the Deben cell at 900 N without inserting a fabric sample - a force higher than those applied in the experiment - and setting that clamp distance at 0 m. From the applied force F, the applied pressure P was calculated:

$$\begin{aligned} P &= \frac{F}{A_{sample}} \\ \Rightarrow P_{1\ layer} &= \frac{F}{A_{sample,1\ layer}} \\ \Rightarrow P_{4\ layers} &= \frac{F}{A_{sample,4\ layers}} \end{aligned}$$

Here, A_{sample} is the average fabric area of each sample, as calulated in subsubsection 2.2.3.1. From the clamp distance, V_f was calculated:

$$\begin{aligned} V_f &= \frac{V_{fibres}}{V_{clamps}} \\ &= \frac{A_{sample} \cdot \frac{\rho_A}{\rho_V}}{A_{sample} \cdot h} \\ &= \frac{\rho_A}{\rho_V \cdot h} \\ &= \frac{\rho_A}{\rho_V \cdot h} \cdot 100\% \end{aligned}$$

Here, V_{fibres} is the absolute volume of the fibres and V_{clamps} is the absolute volume of the three dimensional space between the clamps, which is a function of the "height", or distance between the clamps, h. ρ_A and ρ_V are the areal and volumetric densities of the samples, respectively. This is a simple formula as both densities are constant within each sample, and so the V_f depends only on the distance between the clamps.

The µCT images allowed for measurement of this distance h directly on the images, and so equal pressure-V_f curves should have been obtained for the machine and image data. This was, however, not the case. As the machine data depends on internal measurements within the Deben cell and is thus less reliable than the image data, corrections were sought for the machine data. Eventually, two corrections were applied: PEEK jaw compliance was taken into account, and the zero-point was shifted slightly.

The first correction was the most significant: little attention had been paid to the fact that the PEEK jaws of the Deben cell were themselves elastically compressible, and so distorted the displacement measurements. To remedy this, five calibration measurements were made, activating the Deben cell without an inserted sample. This returned the calibration curves displayed in figure 5.1. The curves were converted into stress-strain curves by:

$$\begin{aligned}
\sigma_{jaws} &= \frac{F}{A_{jaws}} \\
&= \frac{F}{\pi \cdot {r_{jaws}}^2} \\
&= \frac{F}{\pi \cdot 44\ mm^2} \\
\epsilon_{jaws} &= \frac{\Delta L}{L_0} \\
&= \frac{\Delta L}{59.5\ mm + 19.5\ mm}
\end{aligned}$$

Here, σ_{jaws} and ϵ_{jaws} are the stress and strain of the PEEK jaws. F is the applied force by the Deben cell and A_{jaws} is the cross sectional area of the jaws, calculated using their radius r_{jaws}. ΔL is the compressed height of the jaws and L_0 is their original, uncompressed height. Remarkably, the calibration curves seem to be split into two linear regions. The gradients of these linear trendlines reveal the compliance of the jaws: if a force below 64.71 N is applied, the jaws compress by $6 \cdot 10^{-4}$ mm per N, but upwards of that value, the compliance is $9 \cdot 10^{-5}$ mm per N. The slopes in the converted stress-strain curves show that this corresponds to linear elastic behaviour for materials with a Young's modulus of approximately 98 and 576 MPa. The fact that these curves have two linear regions instead of one, and that the Young's modulus is much lower than the average Young's modulus of PEEK (approximately 3.6 GPa) has not yet been explained, but it is thought to be the result of the jaws not touching each other in a completely parallel way during compression. In any case, the compliance from these calibration tests was applied to the machine data generated by the Deben cell.

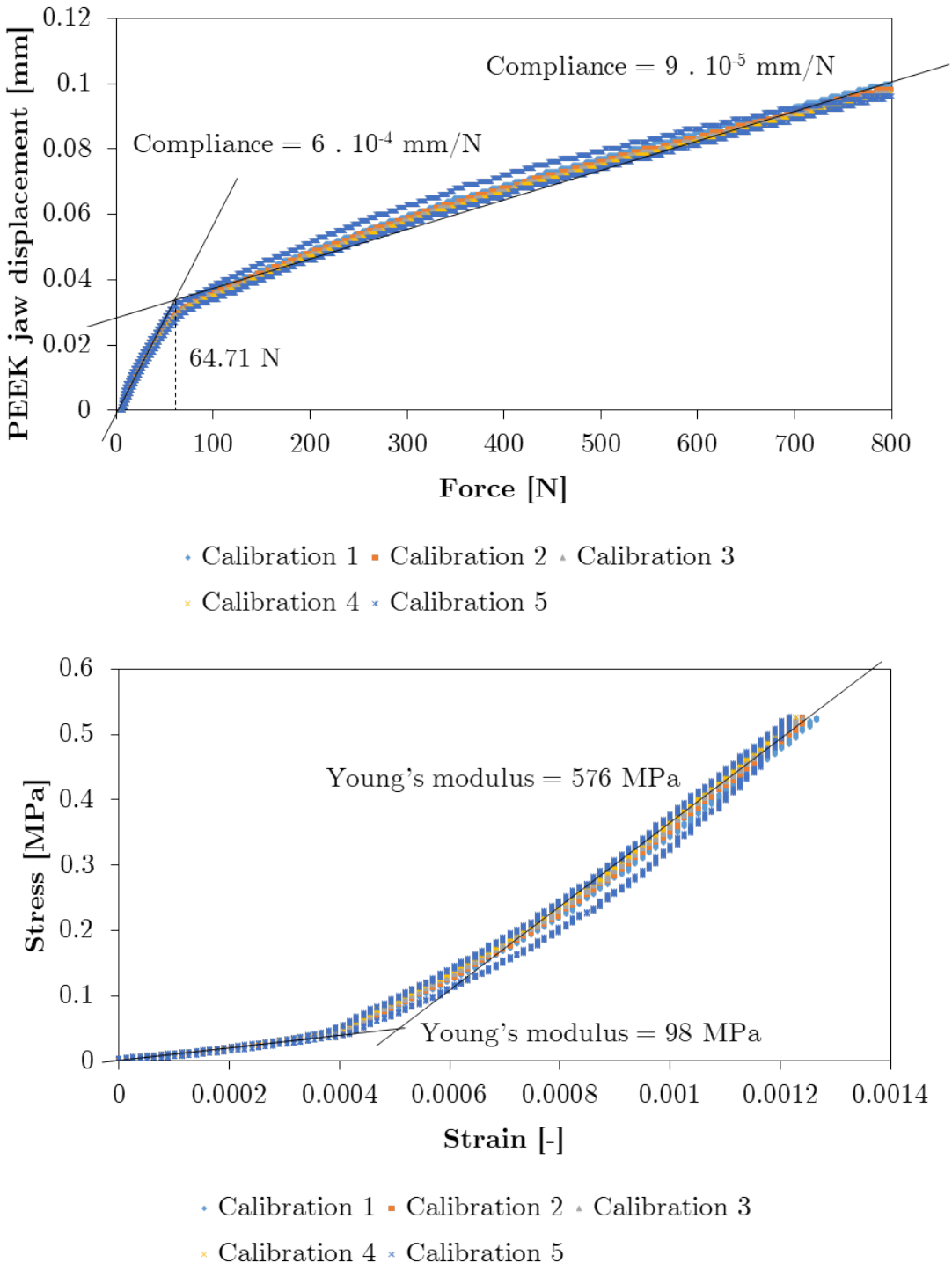

Figure 5.1: Calibration curves to evaluate the compliance of the PEEK jaws used to apply pressure in experiment 1. The compliance is equal to the slope of the linear elastic regions in the displacement-force curve (top). These regions can be described with a Young's modulus, found similarly as the slope in the stress-strain curve (bottom). Linear elastic behaviour was expected, but two regions with differing Young's moduli were not. Additionally, the moduli are much lower than the reported value for PEEK.

As the machine data still did not correspond to the image data after this correction, a minor secondary correction was applied: the zero point was artificially shifted so that the distance between the jaws, h (and thus also V_f), for the uncompressed fabric samples, was equal in both machine and image data. Applying both corrections yielded the graphs in figure 5.2. From this, it is clear that there is still a difference between the machine and image data, though it is quite minor. Plots of the machine data versus the image data are shown in figure 5.3, and reveal that the machine data for the four layer fabric is actually more accurate than the machine data for the single layer fabric. For both samples, the µCT image data is considered more correct than the machine data, so only image data will be used in further discussion.

5.1.2 Experimental compression results

Combining the previous pressure-V_f curves yields figure 5.4. The first observation that should be made is that the shape of these curves agrees well with the linear-exponential-linear consolidation behaviour of fabrics outlined in subsection 1.2.2. Stage 1 consolidation appears to occur up to 45-50% V_f, as a large increase in V_f is found for a very minimal increase in pressure. It is at this stage that the Deben cell jaws come into contact with the fabric and crimp balance takes place by flattening of the yarns. This continues on for longer in the four layer fabric sample, as there are more gaps (δ) to remove in the thickness direction. Stage 2 consolidation then occurs for most of the rest of the measurement, up to approximately 60% V_f for the single layer fabric sample and 70% for the four layer fabric sample. Here, voids are removed between the yarns and individual fibres within the yarns but the fibres start coming into contact with each other, providing exponentially increasing resistance to displacement and thus compaction, due to interfibre friction. Stage 3 consolidation takes place at the end of the experiment, when the removal of voids and the slipping of the fibres have reached their limits. Further compaction is now only possible by deformation of the fibres themselves, which is almost impossible, explaining the very high increase in pressure for minimal increases in V_f.

At equal pressures, the four layer fabric seems to exhibit higher V_f than the single layer fabric. One of the main reasons for this could be nesting, the concept described in subsection 1.2.2. As yarns fill the spaces between yarns in the layers above and below their own layer, voids are efficiently removed and the fabric thickness is reduced significantly more at the same compression than if the yarns remained neatly stacked on top of each other. This hypothesis is strengthened by the fact that larger hysteresis takes place upon decompression. For the single

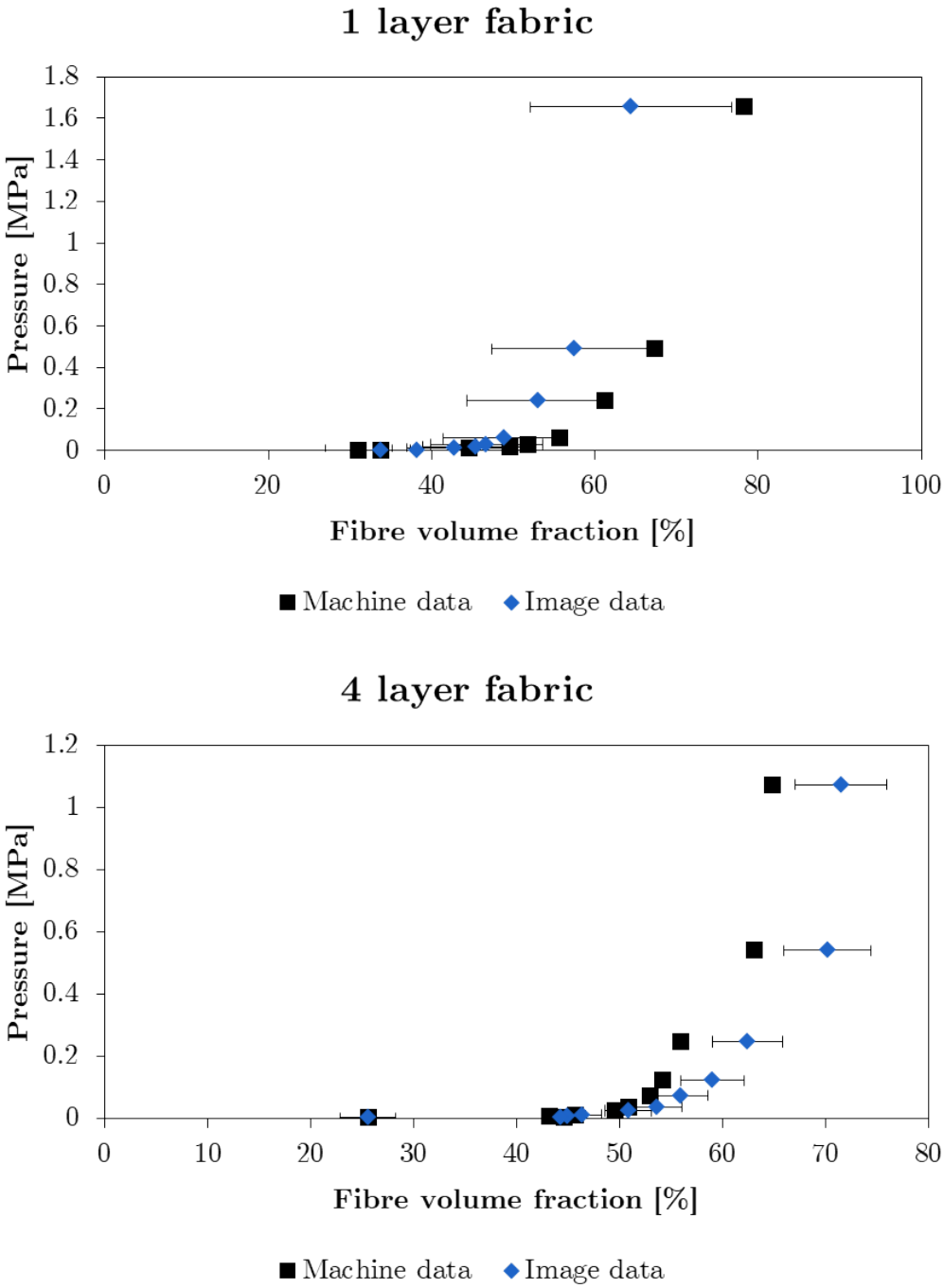

Figure 5.2: Plots of the pressure versus the V_f for the single layer fabric sample (top) and the four layer fabric sample (bottom), after corrections were applied to the machine data. The machine data still differs from the image data, though they should be the same. The shape of the curves is in good agreement with the linear-exponential-linear consolidation curve observed in literature.

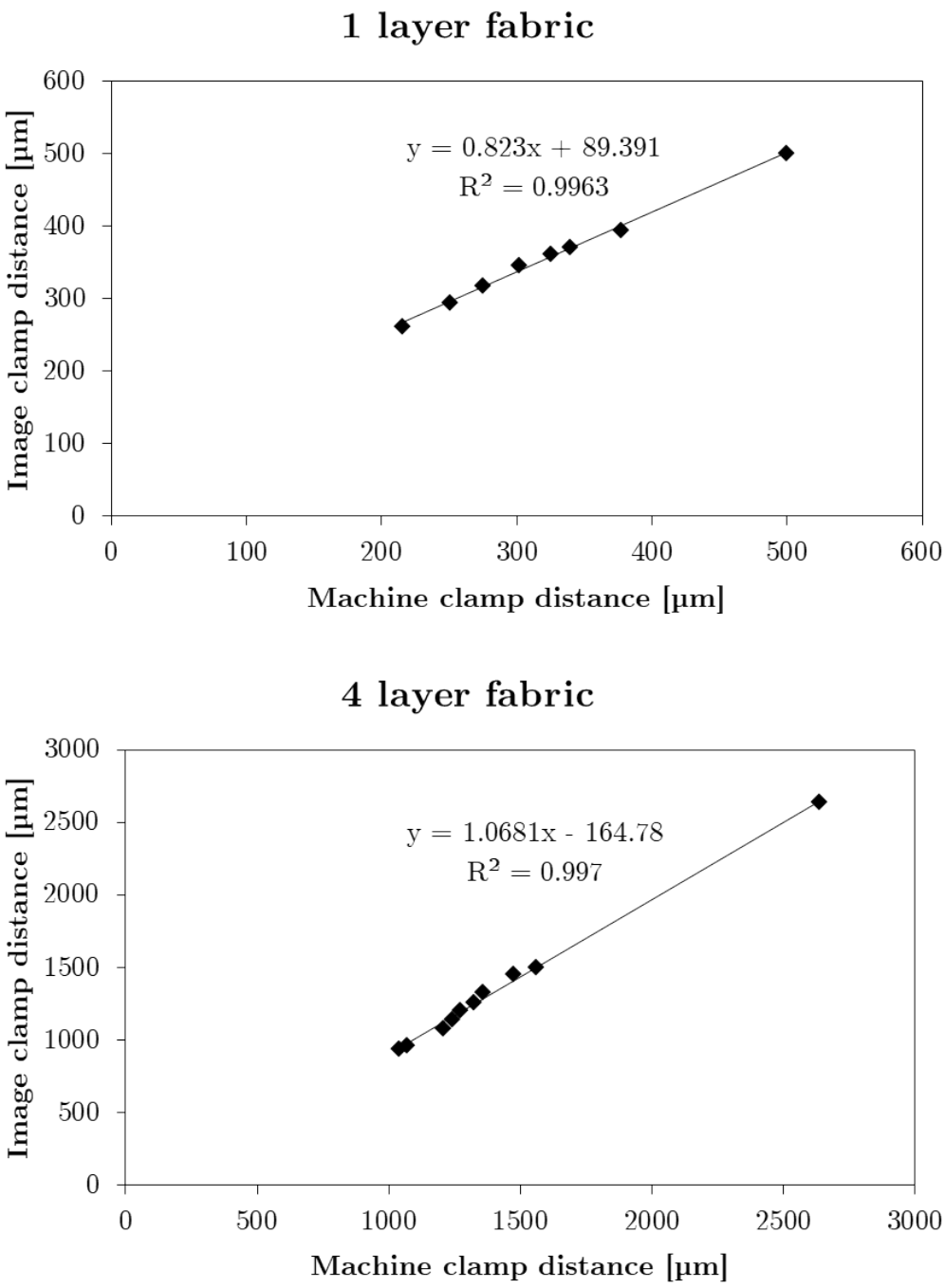

Figure 5.3: Plots of the clamp distance as gathered from the image data versus the machine data, for the single layer fabric sample (top) and the four layer fabric sample (bottom). While clearly correlated, both values are not identical: the slopes of the trendlines should be 1.

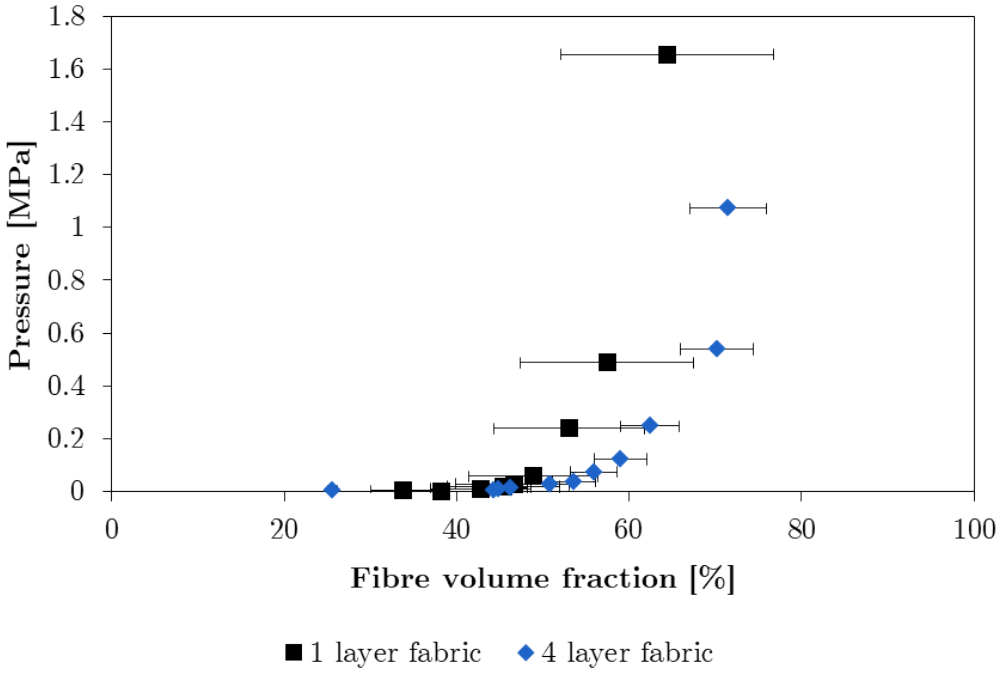

Figure 5.4: Plot of the pressure versus the V_f for the µCT image data of the single layer and the four layer fabric samples. The shape of the curves is in good agreement with the linear-exponential-linear consolidation curve observed in literature. The four layer fabric sample seems to have a higher V_f at equal stress, indicating a larger thickness reduction took place, which can be ascribed to more crimp balance, a higher void content before compression, and nesting.

layer of fabric, the average V_f before compression was 33.72%, while after decompression this was 38.15%, indicating that the deformation caused by compaction was not fully elastic. This makes sense considering it is not energetically beneficial for many of the removed voids to reintroduce themselves, for example. For the four layer fabric sample. the difference was much higher: a V_f of 25.56% was noted before compression, but a V_f of 44.30% remained after decompression. As nesting is an inelastic displacement, this likely occurred, on top of void removal and intrayarn fibre displacement.

These same observations can be made by inspecting the µCT images visually, as in figures 5.5 and 5.6. At low applied forces, the yarns are moved into contact with the clamps of the Deben cell and each other. This is achieved by flattening the yarns and thus balancing out any crimp inequalities, which can also be seen by the apparent rotation of the yarn cross sections. At intermediate applied forces, the yarns are stuck in place and voids between them are removed by interyarn fibre displacement, deforming the yarn cross sections. Due to the low image quality, this cross section deformation is difficult to notice, but it is clear that the yarns no longer shift and the voids are removed. At very high applied forces, almost no further deformation takes place, corresponding to the third stage of consolidation.

In an attempt to quantify the difficult to detect yarn cross section deformation, average yarn widths were measured on the µCT images. The results for the single layer fabric are shown in figure 5.7. It is clear that the error margins are large; this is due to the noise on the image preventing accurate selection of voxels on the extrema of the yarn. As such, no statistically significant results can be extrapolated. This means the expected increase in yarn width with increasing pressure cannot be confirmed experimentally until better quality µCT images are obtained. Curiously, the chart seems to indicate that the warp yarns actually decrease in width between the uncompressed state and the loaded state. Note that the measurement at 10 N should be ignored, as this anomaly is caused by the sample being shifted with respect to the µCT-scanner (see figure 5.5). Due to the missing results and the multilayer fabric image displaying even more noise, especially at high pressures (see figure 5.6), no attempt was made to measure yarn widths on the four layer fabric sample.

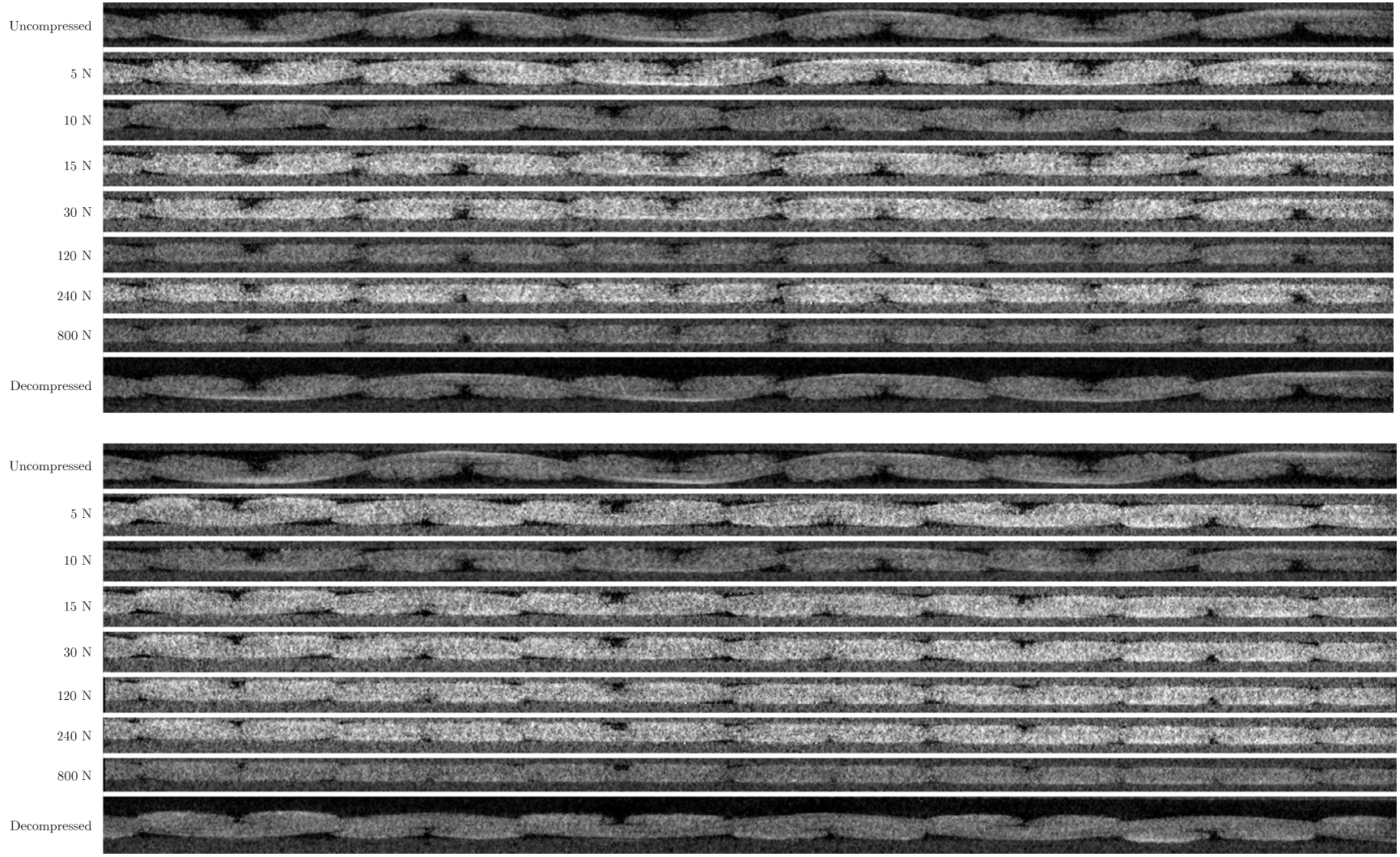

Figure 5.5: µCT images of the single layer fabric sample during compression. The XZ section shows the cross section of the weft yarns (top), while the YZ section shows the cross section of the warp yarns (bottom). Yarn flattening, void removal and minor yarn cross section deformation can be observed.

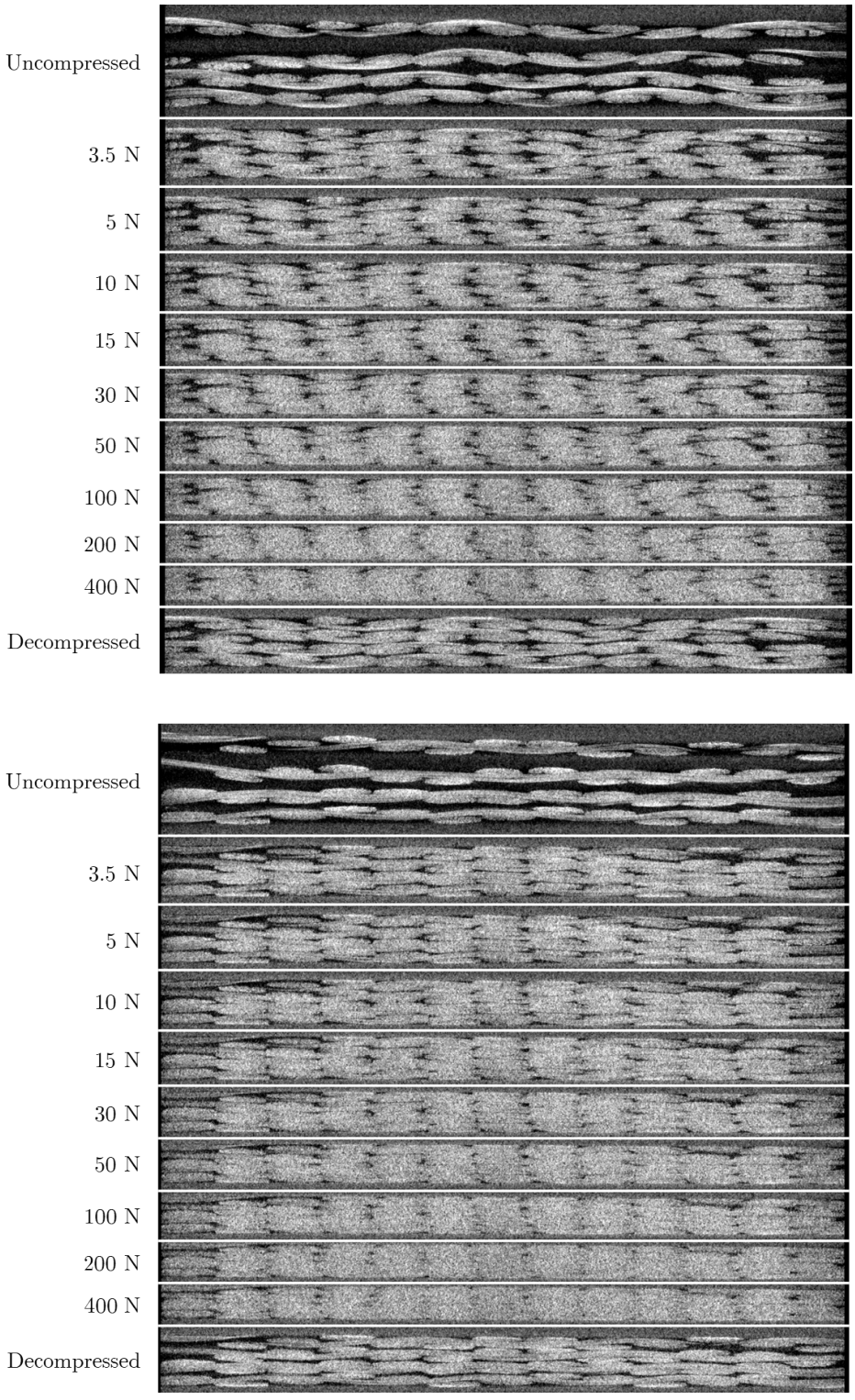

Figure 5.6: µCT images of the four layer fabric sample during compression. The XZ section shows the cross section of the weft yarns (top), while the YZ section shows the cross section of the warp yarns (bottom). Yarn flattening, void removal and minor yarn cross section deformation can be observed. From the decompressed image, it is clear that nesting has taken place.

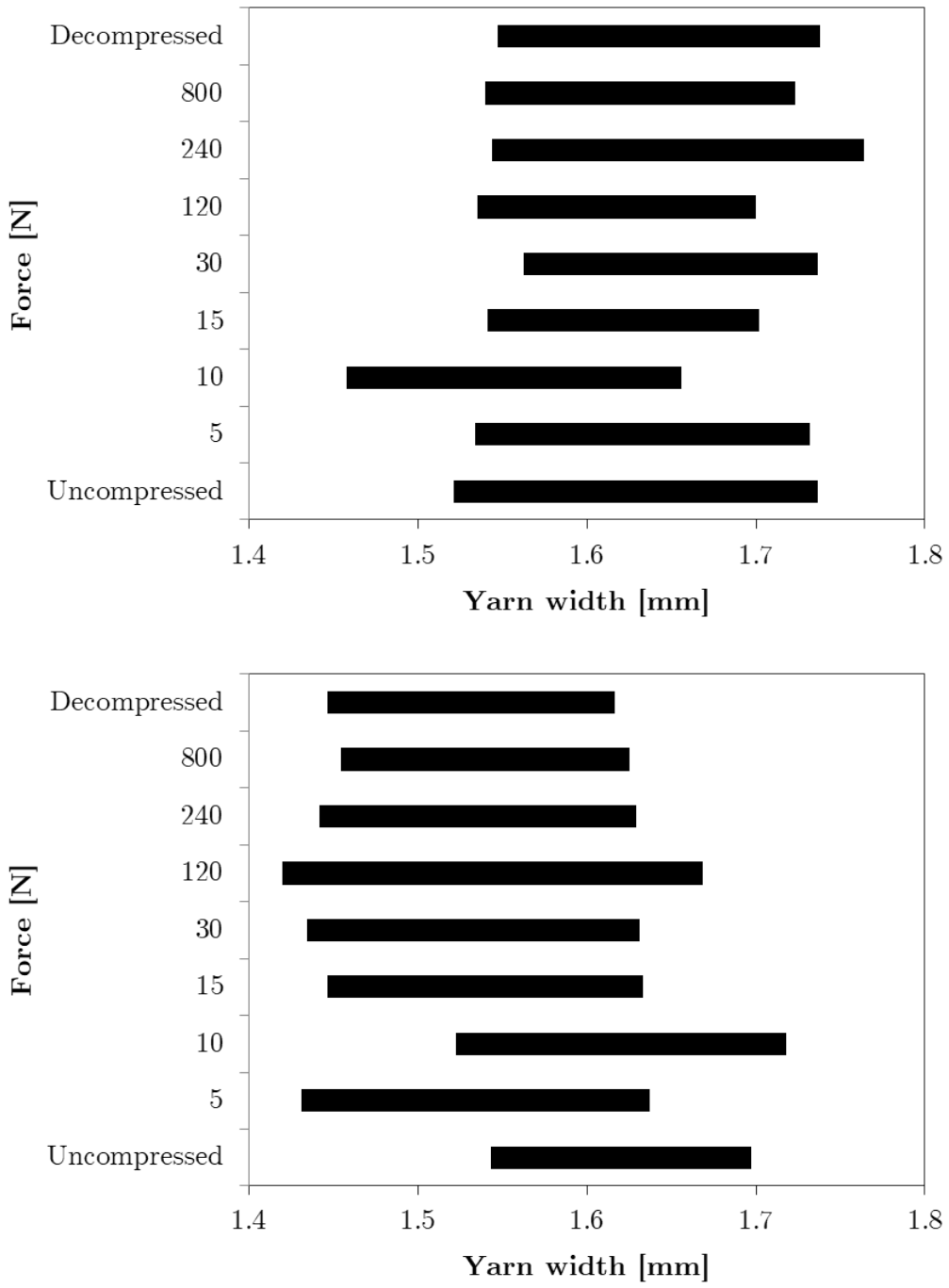

Figure 5.7: Experimental weft (top) and warp (bottom) yarn width measurements of the single layer fabric sample under increasing compression. The error margins are large due to the low µCT image quality, so no statistically significant results can be obtained. Note that the X-axes do not start at 0 mm. The bars shown encompass the average yarn width and one standard deviation along either side. The anomalous measurement at 10 N should be discounted.

5.2 Numerical compression

5.2.1 Compression simulation

Consolidation behaviour was investigated numerically by subjecting the final truss-and-beam model chosen in section 4.2 (127 fibres per yarn, a coefficient of friction of 0.10, a time step of 0.06 s and a two-stage weaving process) to a compression simulation. To do this, the output of the woven model was used as the input for a new simulation, and two rigid plates were added to either side of the fabric. The output nodes of the woven model - including those of the slave yarns - were read using an adapted Python script, originally by Daelemans. The script of this output node reader is given in Appendix A. These nodes were then copied and pasted into a new ABAQUS input file. The rigid plates were created as two separate, new parts in ABAQUS/CAE, with a surface area larger than the fabric area. The plates were set to be undeformable but displaceable, and were brought to either side of the fabric (in the Z-direction) by translation in the ABAQUS/CAE assembly. Care was taken to ensure the plates were not touching any of the fibres. Contact interactions were also defined between the plates and the truss elements. The beam elements were still not given any contact properties as they do not represent the fabric geometry; they are just a tool for bestowing flexural rigidity. Two loading steps were then defined. The first step entailed a displacement of the plates towards each other, compressing the fabric in between them. The second step was a mirror of this, simulating decompression by separating the plates over the same distance. The distance moved by each plate in each step was 0.18 mm, meaning the fabric was compressed by 0.36 mm in total. The time allocated to each step was 0.1 s. YZ- and XZ-views of the compression/decompression simulation are shown in figures 5.8, 5.9, 5.10 and 5.11.

In these figures, the warp and weft yarns seem to migrate away from the centre of the fabric at higher pressures during compression, or all throughout decompression, destroying the woven structure. This is likely the result of an error in the contact interactions or boundary conditions linked to a larger time step. Peculiarly, the simulation is not dynamic as this would imply, but quasi-static - as judged by the energy balance in figure 5.12. The internal energy during the simulation is always much higher than the kinetic energy, for both the compression and the decompression loading steps. An explanation for this phenomenon or a method to prevent the migration is yet to be found.

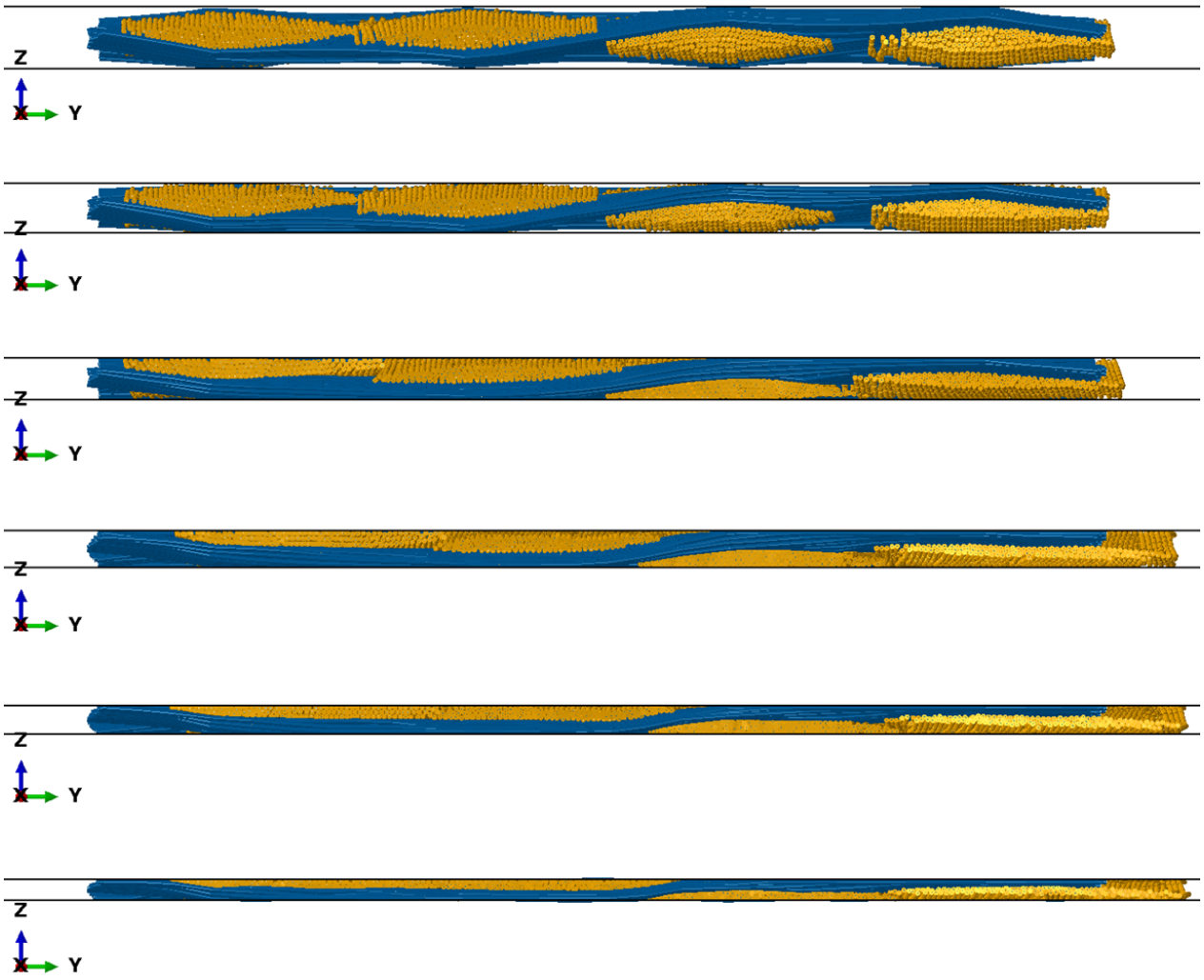

Figure 5.8: A YZ-view of the compression simulation of the truss-and-beam model. The as-woven fabric (top) is deformed by the nearing of two rigid plates, until it reaches its final compressed state (bottom). The plates are displaced by 0.18 mm each, in a time step of 0.1 s. Only the truss elements are shown, as they represent the fabric geometry. These are yellow in the warp direction (X-direction) and blue in the weft direction (Y-direction). Note that the warp and weft yarns seem to migrate away from each other in the Y-direction.

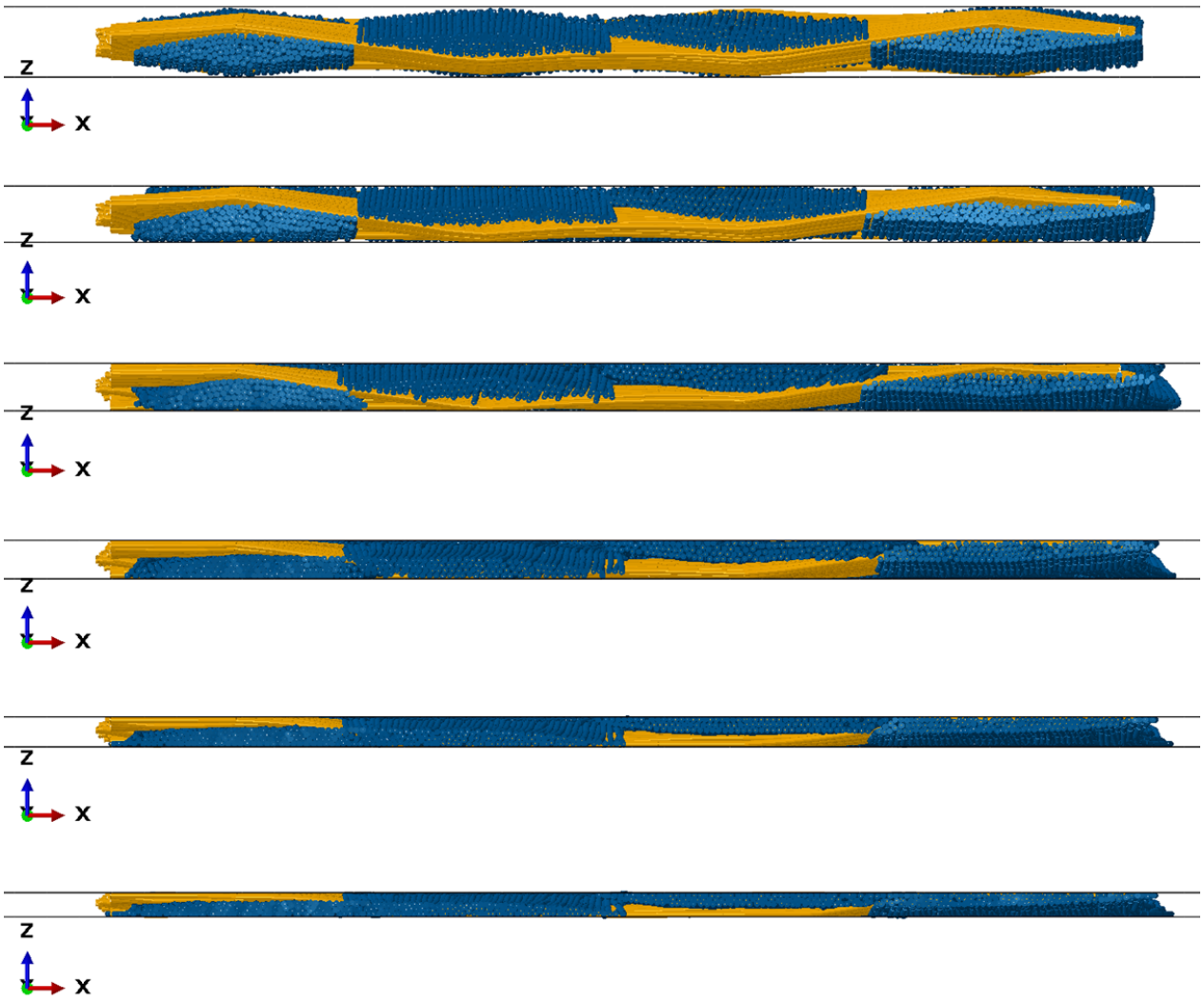

Figure 5.9: An XZ-view of the compression simulation of the truss-and-beam model. The as-woven fabric (top) is deformed by the nearing of two rigid plates, until it reaches its final compressed state (bottom). The plates are displaced by 0.18 mm each, in a time step of 0.1 s. Only the truss elements are shown, as they represent the fabric geometry. These are yellow in the warp direction (X-direction) and blue in the weft direction (Y-direction).

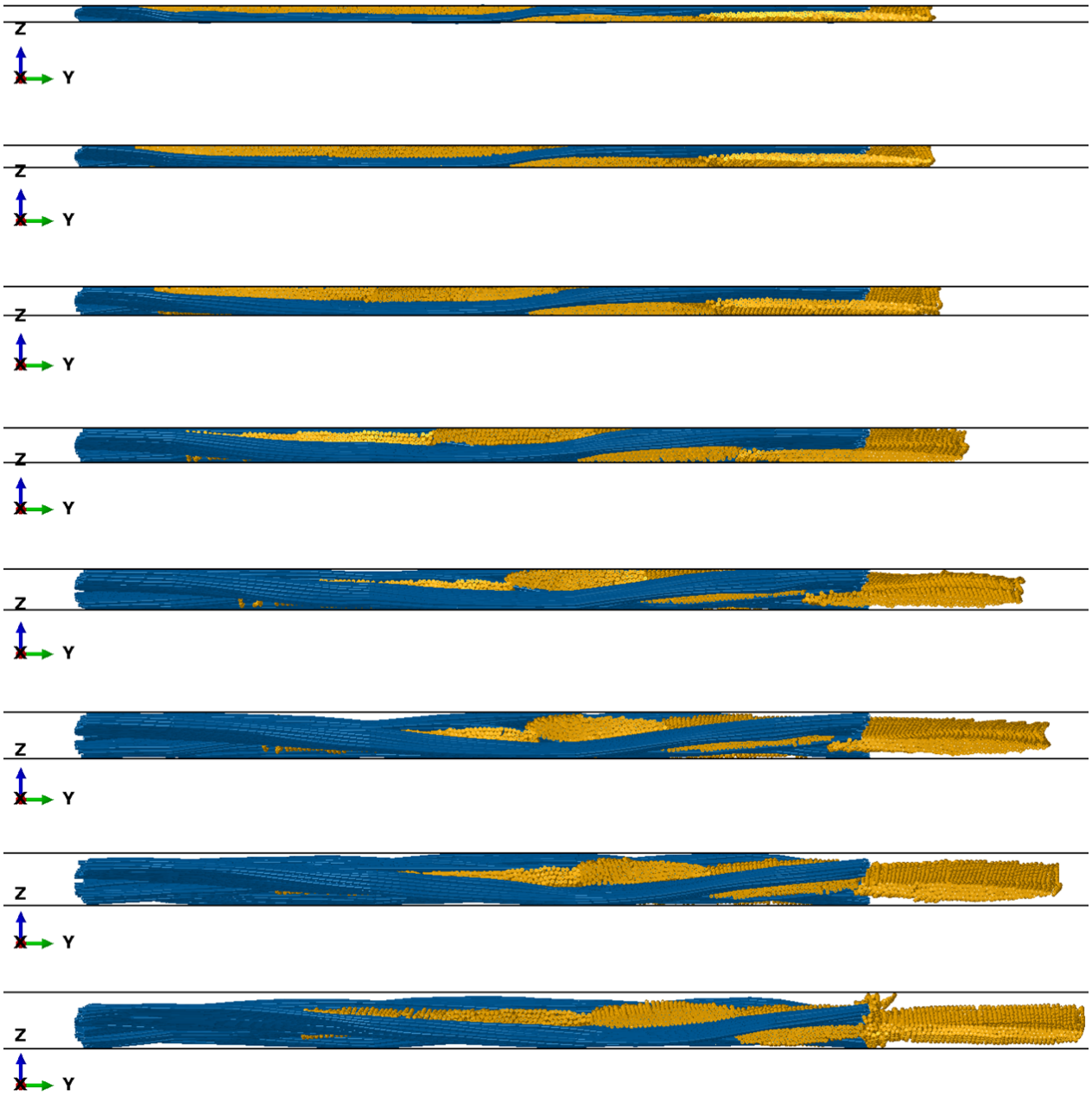

Figure 5.10: A YZ-view of the decompression simulation of the truss-and-beam model. The fully compressed fabric (top) is allowed to relax by the separating of two rigid plates, until it reaches its final relaxed state (bottom). The plates are displaced by 0.18 mm each, in a time step of 0.1 s. Only the truss elements are shown, as they represent the fabric geometry. These are yellow in the warp direction (X-direction) and blue in the weft direction (Y-direction). Note that the warp and weft yarns seem to migrate away from each other in the Y-direction.

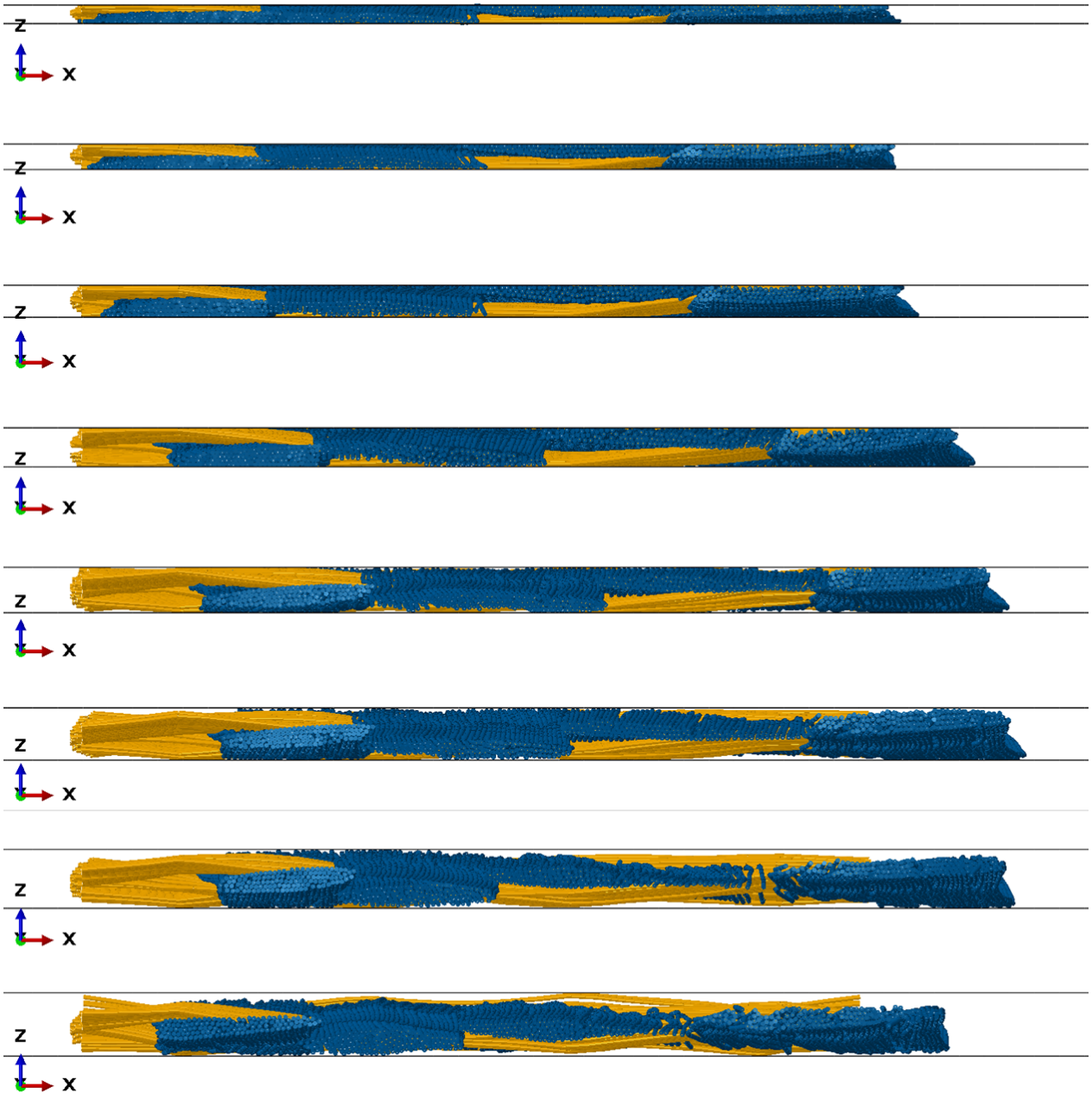

Figure 5.11: An XZ-view of the decompression simulation of the truss-and-beam model. The fully compressed fabric (top) is allowed to relax by the separating of two rigid plates, until it reaches its final relaxed state (bottom). The plates are displaced by 0.18 mm each, in a time step of 0.1 s. Only the truss elements are shown, as they represent the fabric geometry. These are yellow in the warp direction (X-direction) and blue in the weft direction (Y-direction). Note that the warp and weft yarns seem to migrate away from each other in the X-direction.

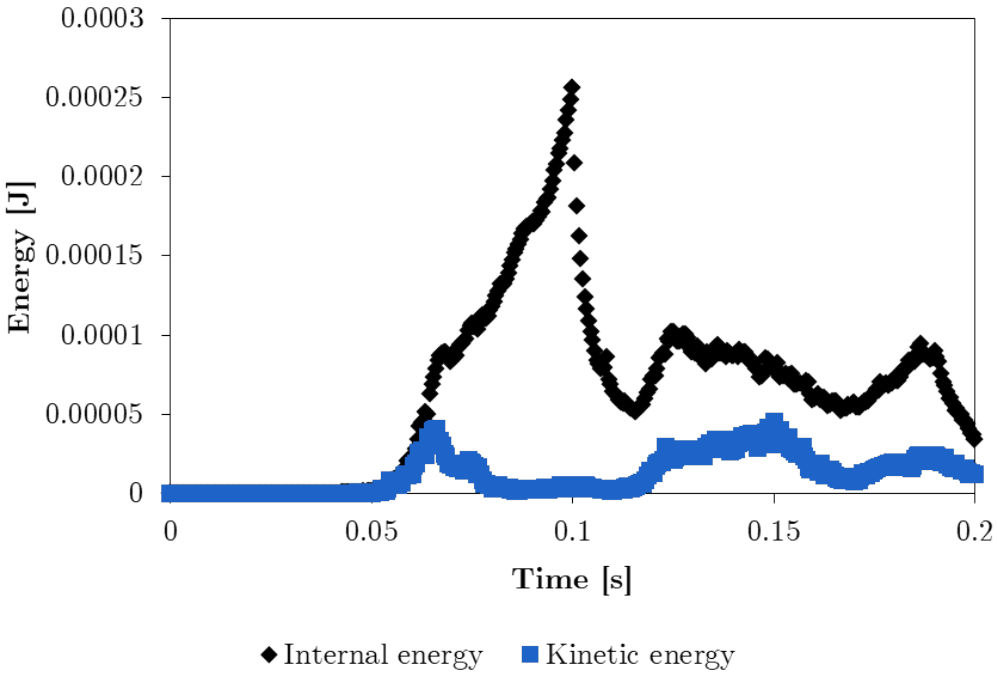

Figure 5.12: Energy balance for the compression/decompression simulation of the truss-and-beam model in a total time step of 0.2 s. Both loading steps in the simulation are clearly quasi-static, as the internal energy is always higher than the kinetic energy.

5.2.2 Numerical compression results

Visually, figures 5.8 and 5.9 display the same consolidation behaviour that has been observed thus far, if the erroneous yarn migration is ignored. The plates first make contact with the fabric at the peaks of its yarns. Immediately the yarn cross-sections are deformed, flattening the peaks, as the fibres touched by the plate start displacing. At the same time, any large voids cause by crimp inequalities are removed. As pressure increases, yarn cross section deformation becomes very pronounced - much more so than was visible in the experimental results. The yarn cross sections are flattened and fibres fan out to fill the interyarn voids. Further compression continues to result in further yarn cross section deformation through fibre displacement, but the extent of new deformation is gradually decreased as fibres block each other. Figures 5.10 and 5.11 show that yarn heights increase and yarn widths decrease as pressure is lifted, by virtue of the fibres finding locations where they are no longer compressed into neighbouring fibres. The fully relaxed fabric is shown to remain much more deformed and "disorganised" than the original uncompressed, woven fabric, with fibres almost spread in between yarns. This signifies that much of the fibre displacement is inelastic.

To gain numerical data on the consolidation behaviour, two history outputs were queried in ABAQUS during the simulation: the displacement of the rigid plates, and the reaction forces on those plates. By Newton's third law of motion, the reaction forces $F_{reaction}$ on both plates were equal and represented the force applied by the plates onto the fabric during the simulation. This allowed for easy calculation of the applied pressure P via:

$$\begin{aligned} P &= \frac{F_{reaction}}{A_{fabric}} \\ &= \frac{F_{reaction}}{b_{warp} \cdot b_{weft}} \end{aligned}$$

Here, A_{fabric} is the area of the fabric that was being compressed, and b_{warp} and b_{weft} are the average widths of the entire fabric in warp and weft direction, respectively. These widths were measured in ABAQUS according to the method described in subsubsection 2.2.1.2, at several points during the deformation. Due to the constraint equations applied to the end nodes of each fibre, the fabric had the same size throughout the whole simulation. The width of the fabric in the warp direction was found to be 7.06 mm, and in the weft direction this was found to be 6.40 mm, leading to a fabric area of approximately 45.18 mm^2. The queried plate displacement was used to calculate the V_f with an analogous formula as employed in experiment 1:

$$V_f = \frac{\rho_A}{\rho_V \cdot h} \cdot 100\%$$

Here, h represents the distance between the plates, which was kept track of by measuring the original distance between the plates before compression, and subtracting the combined displacement of both plates from that value.

These calculations led to a pressure-V_f graph, as given in figure 5.13. Immediately, it is clear that the shape of the curve is in good agreement with the experimental data and the linear-exponential-linear curve described in literature. This is an improvement over the consolidation behaviour displayed by the truss-only model by Daelemans. However, the curve is also shifted towards higher V_f, though the attained pressures are within the correct order of magnitude. The curve shift is so substantial that V_f over 100% are obtained, which is physically impossible - the volume of fibres between the plates cannot be higher than the total volume between the plates. A small contributor to this is likely to be the incorrect dimensions given to the truss elements: the cross sectional area of these elements were left

as defined by Daelemans instead of being updated to the values given in table 3.1. As these cross sectional areas differ only approximately 10% from the values assigned in the truss model, this cannot be the sole explanation for the abnormally high V_f.

Instead, the explanation was found when zooming in on the compressed state of the model; see figure 5.14. It was discovered that the contact interactions between the truss elements failed, leading to the clipping of fibres within other fibres and beyond the plates. Two fibres taking up the same volume within the plate volume or finding their way out of the plate volume illustrate how the V_f was able to increase above 100%. A theory was posited that this clipping was caused by the constraint equations on the end nodes of the fibres: if all voids have been removed from the fabric but compression continues, stage 3 consolidation must occur, inducing elastic extension of the fibres due to the Poisson contraction effect. The constraint equations prevent this extension as the unit cell is kept at a fixed size. This would lead ABAQUS/Explicit to internal conflict, forcing it to allow more clipping and to compensate for that by adding reaction forces to split the fibres later. A compression/decompression simulation was run without constraint equations, but the results were no better: clipping still occurred, disproving the theory. The only parameter found to affect the clipping behaviour was the total applied compression. A simulation where the plates were only moved towards each other by 0.284 mm instead of 0.36 mm displayed no clipping. A permanent solution to this problem, other than restricting the simulation to lower compression, likely requires the definition of new, stricter contact interaction properties or boundary conditions (which were also the problematic components in the yarn migration issue). This was not attempted in this dissertation due to time constraints.

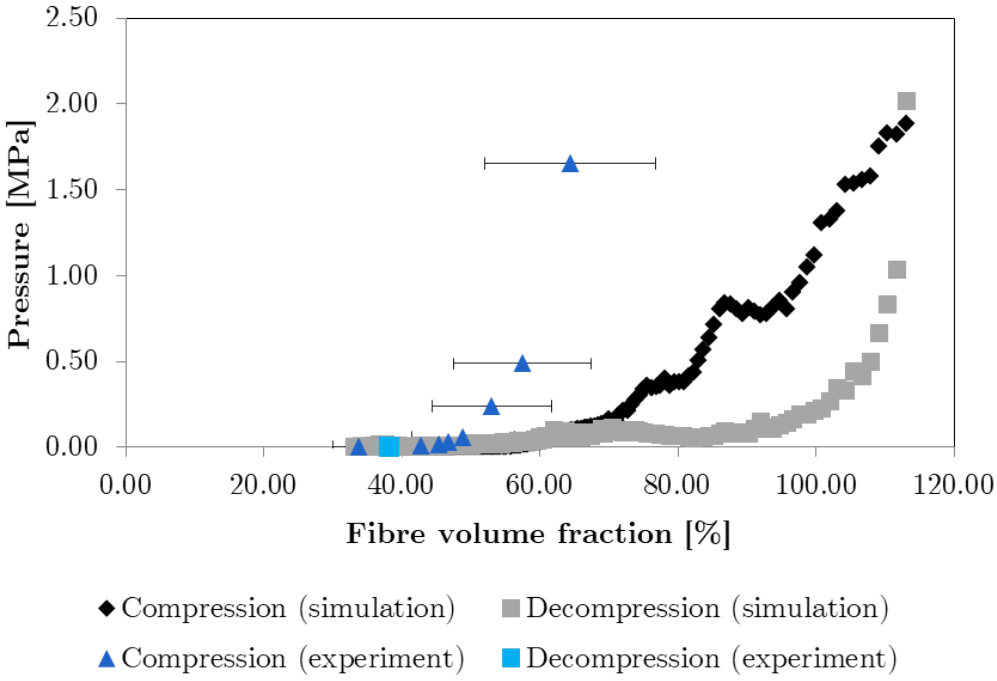

Figure 5.13: Plot of the pressure versus the V_f for the numerical compression/decompression simulation of the truss-and-beam model, compared to the experimental results of the single layer fabric sample from experiment 1. The shape of the simulation curves is in good agreement with the experimental linear-exponential-linear consolidation curve, but it is shifted towards higher V_f.

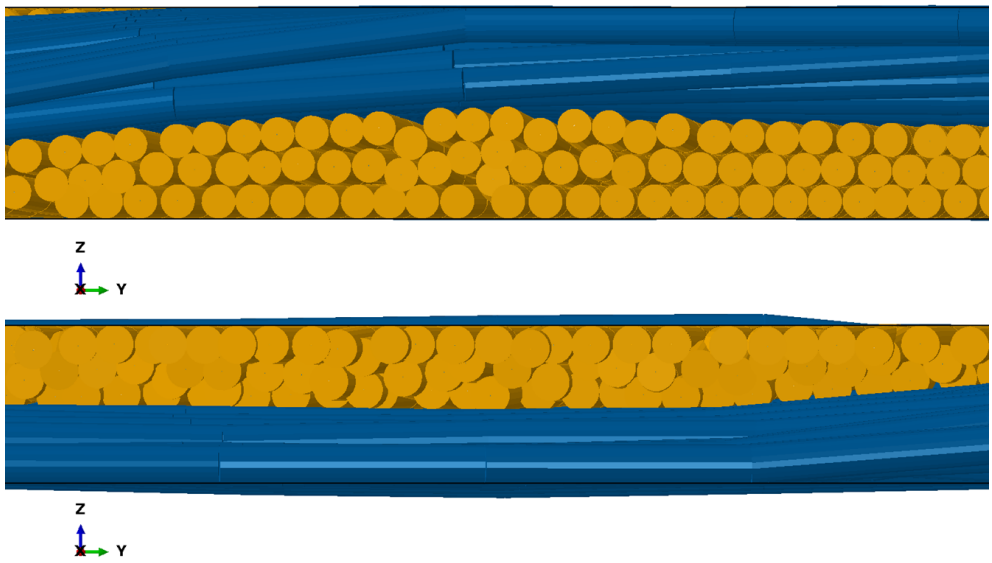

Figure 5.14: A zoomed in YZ-view of fully compressed truss-and-beam models, at a compression of 0.284 mm (top) and 0.36 mm (bottom). The smaller compression seems to cause few contact problems, but the larger compression results in clipping of the fibres within each other and beyond the plates.

Chapter 6

Conclusion

6.1 Summary

The goal of this dissertation was to investigate fabric behaviour under compression, both experimentally and numerically, though focused on the latter. This is because all commonly used FRP production processes apply pressure to reinforcing fabrics during a consolidation stage, to increase V_f. During this consolidation, different defects (e.g. porosity and fibre waviness) can be introduced, resulting in large costs for the industry and maluses to the environment. There is, thus, a need for robust predictive tools such as finite element fabric models.

A novel, discrete meso-scale fabric model was constructed, starting at the micro-scale, to portray a 2/2 twill woven glass fibre fabric produced by P-D Interglas Technologies GmbH. At the microscopic scale, fibres were created as chains of sequentially connected truss elements, upon which beam elements were then superimposed, in an effort to decouple the fibres' Young's modulus and flexural rigidity. The truss elements only transmit axial loads and are responsible for the stiffness (Young's modulus) of the model while also representing the actual geometry. The beam elements, on the other hand, can transmit flexural loads and are responsible for the flexural rigidity of the model. At the mesoscopic scale, yarns were created by arranging the fibres in a hexagonal bundle, and experimentally measured values were assigned to each element, ensuring correct dimensions and properties of the assembled yarns. At the macroscopic scale, the fabric was built by expanding on a model by Daelemans containing only truss elements. Via a custom Python script, material properties were edited and beam elements were superimposed on top of the existing truss elements.

With the model constructed, its weaving process was investigated to discover the influence of different parameters (coefficient of friction, number of fibres per yarn, time step and one- or two-stage loading) on the final as-woven geometry. From these results, the best model was chosen by comparison to experimental measurements gathered via µCT-scans. A combined truss-and-beam model with 127 fibres per yarn, a coefficient of friction of 0.10, a time step of 0.06 s and a two-stage weaving process was chosen. While the model is not completely accurate, it was validated within the correct order of magnitude.

To study the behaviour of the fabric during consolidation, two experiments were set up, where pressure was applied to fabric samples (continuously or statically) and the samples were µCT-scanned. While there were challenges due to inaccurate machine data and low µCT image quality (leading to the results of only one experiment being used), yarn flattening, removal of voids and yarn cross-section deformation were all observed, as well as nesting in the multilayer sample. In addition, hysteresis was encountered upon decompression, showing that the compression deformation was not entirely elastic.

To investigate similar behaviour in the truss-and-beam model, the output of the weaving simulation was used as the input for a new compression simulation. The fabric was surrounded by two rigid plates that were brought together and subsequently separated, and the reaction forces on these plates were numerically calculated. This was then compared to the pressures and V_f from the experimental data. The same pressure-V_f curve shape was obtained as in the experiments, which was an improvement over the truss-only fabric model, but the curve was shifted towards higher V_f, mainly due to contact interaction errors in the form of clipping.

6.2 Further research

The work done in this dissertation can provide useful information on fabric behaviour during consolidation. The truss-and-beam model, especially, can be used to predict behaviour, if the present errors are resolved, and the accuracy of the model is increased. The fact that it applies flexural rigidity separately from other material properties allows it to be finetuned easily. The model can also be used for other research in the composite industry as a robust all-purpose fabric model, for example to study draping behaviour over complex shapes. If a method is found to add twist to the yarns, it could even be used as a general fabric model in the textiles industry.

The first improvements that should be made to this model are those that can increase the accuracy of its as-woven state. One change that should be made is to update the truss element dimensions: the cross sectional areas in the model were left as they were designed by Daelemans, but should be substituted by the values given in table 3.1. While these only differ by approximately 10%, they define the size of the truss elements and so define the geometry of the entire model. Secondly, a way should be sought to make the fanning out of fibres easier in the model, to compensate for the reduced amount of fibres in a yarn as compared to the real fabric. Thirdly, more attention should be paid to the quasi-static or dynamic nature of the weaving simulations, as this was only investigated after all measurements were processed but could greatly increase the robustness of the model.

To increase the accuracy of the compression simulation, the yarn migration and clipping issues must be solved. This would likely require more complex contact interactions and possible changes to the periodic boundary conditions. If after solving the issues, the pressure-V_f curve is still shifted towards higher V_f, it can be artificially shifted back. This means not allowing the fabric to compress as much, which could be achieved by increasing the flexural rigidity of the beam elements by increasing their radius. Because their Young's modulus is so low, this would have a negligible effect on the other fabric properties. Another route that could be taken is to use the as-woven state of the truss-only model (which displayed better congruency with the real woven fabric but could not simulate consolidation accurately), and superimpose beam elements onto the fibres of that deformed model before consolidation, instead of superimposing them in the loose topology state. This would provide a more accurate framework to subject to compression, while keeping the improvements in the shape of the pressure-V_f curve that were added by the inclusion of a flexural rigidity.

Concerning the carried out experiments, the µCT image quality of experiment 2 should be improved, after which the images should be processed as a valuable second - hopefully more accurate - source of experimental data. For both the experimental and the numerical analysis of consolidation behaviour, the effect of parameters other than the consolidation pressure could be studied. Known parameters include temperature during the consolidation stage, the number of compaction cycles, the compaction speed, the number of fabric layers and their stacking sequence, interply friction, and matrix material viscosity. It would be a good start to scale up the truss-and-beam model to allow for multiple layers of fabric (and possibly 3D-weaving). Materials other than glass fibre, such as carbon fibre or aramid fibre, could also be investigated.

Bibliography

[1] W. Van Paepegem and I. De Baere, *Composites*. Ghent University, 2018-2019.

[2] A. Khan and C. Lemmen, "Bricks and urbanism in the Indus Valley rise and decline," *American Journal of Archeology*, Feb 2013.

[3] T. Tsuen-Hsuin, "Paper and printing," *Chemistry and Chemical Technology*, vol. 5, no. 1, 1985.

[4] MHRD, *Module 1: Introduction to Composites*. Government of India.

[5] S. Prashanth, K. M. Subbaya, N. Kundachira, and S. Sachhidananda, "Fiber reinforced composites - a review," *Journal of Materials Science Engineering*, vol. 6, May 2017.

[6] M. Kaufmann, D. Zenkert, and M. Åkermo, "Material selection for a curved C-spar based on cost optimization," *Journal of Aircraft*, vol. 48, pp. 797–804, Jun 2011.

[7] A. J. Timmis, A. Hodzic, L. Koh, M. Bonner, C. Soutis, A. W. Schäfer, and L. Dray, "Environmental impact assessment of aviation emission reduction through the implementation of composite materials," *The International Journal of Life Cycle Assessment*, vol. 20, pp. 233–243, Feb 2015.

[8] European Commission, "Clean sky 2: developing new generations of greener aircraft," 2014.

[9] A. Jacob, "BMW unveils i8 Spyder," *Reinforced Plastics*, vol. 56, p. 5, 2012.

[10] A. Jacob, "BWM begins series production of i3 electric car," *Reinforced Plastics*, vol. 57, p. 6, 2013.

[11] Solvay, "Composite materials for automotive applications," Jul 2018.

[12] S. Chu and A. Majumdar, "Opportunities and challenges for a sustainable energy future," *Nature*, vol. 488, pp. 294–303, Aug 2012.

[13] G. Fontaras and Z. Samaras, "On the way to 130 g CO_2/km - estimating the future characteristics of the average European passenger car," *Energy Policy*, vol. 38, pp. 1826–1833, Apr 2010.

[14] F. Taheri, *Advanced Fibre-Reinforced Polymer (FRP) Composites for Structural Applications*. Woodhead Publishing, 2013. Chapter 18 - Advanced fiber-reinforced polymer (FRP) composites for the manufacture and rehabilitation of pipes and tanks in the oil and gas industry, pp. 662-704.

[15] A. C. Filho, *Durability of Industrial Composites*. CRC Press, second ed., Oct 2018. Chapter 21 - Impermeable pipes, pp. 379-392.

[16] K. K. Sadasivuni, D. Ponnamma, J. Kim, J. J. Cabibihan, and M. A. Al Maadeed, *Biopolymer Composites in Electronics*. Elsevier, first ed., 2017.

[17] D. D. L. Chung, *Composite Materials*, vol. 4 of *Engineering Materials and Processes*. London: Springer, 2010. Chapter 4 - Mechanical properties - Composite materials for electrical applications, pp. 73-89.

[18] Lucintel, "Composites market report: trends, forecast and competitive analysis," Jan 2019.

[19] SmarTech Analysis, "3D-printed composites materials markets - 2017: an opportunity analysis and ten-year forecast," Nov 2016.

[20] M. Flemming, G. Ziegmann, and S. Roth, *Faserverbund Bauweisen - Halbzeuge und Bauweisen*. Berlin: Springer, 1996.

[21] D. Cripps, "NetComposites - manufacturing," 2019.

[22] P. Potluri and T. V. Sagar, "Compaction modelling of textile preforms for composite structures," *Composite Structures*, vol. 86, pp. 177–185, Mar 2008.

[23] T. Grieser and P. Mitschang, "Investigation of the compaction behavior of carbon fiber NCF for continuous preforming processes," *Polymer Composites*, vol. 38, pp. 2609–2625, Nov 2017.

[24] B. Chen and T. W. Chou, "Compaction of woven-fabric preforms in liquid composite molding processes: single-layer deformation," *Composites Science and Technology*, vol. 59, pp. 1519–1526, 1999.

[25] B. Chen and T. W. Chou, "Compaction of woven-fabric preforms: nesting and multi-layer deformation," *Composites Science and Technology*, vol. 60, pp. 2223–2231, 2000.

[26] B. Chen, E. J. Lang, and T. W. Chou, "Experimental and theoretical studies of fabric compaction behavior in resin transfer molding," *Materials Science and Engineering*, vol. A317, pp. 188–196, 2001.

[27] R. A. Saunders, C. Lekakou, and M. G. Bader, "Compression in the processing of polymer composites: a mechanical and microstructural study for different glass fabrics and resins," *Composites Science and Technology*, vol. 59, pp. 983–993, 1999.

[28] R. A. Smith, "Composite defects and their detection," *Materials Science and Engineering*, vol. 3, Jan 2009.

[29] L. Liu, B. M. Zhang, Z. J. Wu, and D. F. Wang, "Effects of cure pressure induced voids on the mechanical strength of carbon/epoxy laminates," *Journal of Materials Science and Technologies*, vol. 21, no. 1, 2005.

[30] A. Siver, "Mechanistic effects of porosity on structural composite materials," Master's thesis, University of California, 2014.

[31] J. W. Tang, W. I. Lee, and G. S. Springer, "Effects of cure pressure on resin flow, voids and mechanical properties," *Journal of Composite Materials*, vol. 21, pp. 421–440, Jan 1987.

[32] P. Olivier, J. P. Cottu, and B. Ferret, "Effects of cure cycle pressure and voids on some mechanical properties of carbon/epoxy laminates," *Composites*, vol. 26, no. 7, pp. 509–515, 1995.

[33] X. Liu and F. Chen, "A review of void formation and its effects on the mechanical performance of carbon fiber reinforced plastic," *Engineering Transactions*, vol. 64, no. 1, pp. 33–51, 2016.

[34] L. Q. Zhuang, "Effects of voids on delamination growth in composite laminates under compression," Master's thesis, Texas A&M University, 2012.

[35] A. M. Rubin and K. L. Jerina, "Evaluation of porosity in composite aircraft structures," *Mechanics of Composite Materi*, vol. 30, no. 6, pp. 587–600, 1994.

[36] M. A. Suhot and A. R. Suhot, "The effects of voids on the flexural properties and failure mechanisms of carbon/epoxy composites," *Jurnal Teknologi*, vol. 71, no. 2, pp. 151–157, 2014.

[37] A. Demma and B. B. Djordjevic, "Effects of porosity on the mechanical strength and ultrasonic attenuation of CF-PEEK fibre placed composites.," in *15th World Conference on Nondestructive Testing*, Feb 2008.

[38] P. M. Mohite, *Composite Materials*. NPTEL, Aug 2014.

[39] S. R. Ghiorse, "Effect of void content on the mechanical properties of carbon epoxy laminates," *SAMPE Quarterly*, pp. 54–59, Jan 1993.

[40] J. C. Suarez, F. Molleda, and A. Guemes, "Void content in carbon fibre/epoxy resin composites and its effect on compressive properties," in *9th International Conference on Composite Materials*, (Madrid), 1993.

[41] J. Cinquin, V. Triquenaux, and Y. Rousne, "Porosity influence on organic composite material mechanical properties," in *16th International Conference on Composite Materials*, (Japan), 2007.

[42] S. F. M. Almeida and Z. S. N. Neto, "Effect of void content on the strength of composite laminates," *Composite Structures*, vol. 28, pp. 139–148, 1994.

[43] A. Chambers, J. Earl, C. Squires, and M. Suhot, "The effect of voids on the flexural fatigue performance of unidirectional carbon fibre composites developed for wind turbine applications," *International Journal of Fatigue*, vol. 28, pp. 1389–1398, 2006.

[44] M. W. Czabaja and J. G. Ratcliffe, "Comparison of intralaminar and interlaminar mode I fracture toughnesses of a unidirectional IM7/8552 carbon/epoxy composite," *Composites Science and Technology*, vol. 89, pp. 15–23, Dec 2013.

[45] K. Farnand, Z. N, P. A, and G. Fernlund, "Micro-level mechanisms of fiber waviness and wrinkling during hot drape forming of unidirectional prepreg composites," *Composites: Part A*, vol. 103, pp. 168–177, Oct 2017.

[46] P. S. Bhargav, "Effect of in-plane fiber tow waviness in the strength characteristics of different fiber reinforced composites," Master's thesis, Wichita State University, May 2015.

[47] D. Kugler and T. J. Moon, "Identification of the most significant processing parameters on the development of fiber waviness in thin laminates," *Journal of Composite Materials*, vol. 36, pp. 1451–1479, Jun 2002.

[48] J. P. H. Belnoue, O. J. Nixon-Pearson, A. J. Thompson, D. S. Ivanov, K. D. Potter, and S. R. Hallett, "Consolidation-driven defect generation in thick composite parts," *Journal of Manufacturing Science and Engineering*, vol. 140, Jul 2018.

[49] P. Hallander, M. Åkermo, C. Mattei, M. Petersson, and T. Nyman, "An experimental study of mechanisms behind wrinkle development during forming of composite laminates," *Composites: Part A*, vol. 50, pp. 54–64, Mar 2013.

[50] A. J. Thompson, J. P. H. Belnoue, and S. R. Hallett, "A numerical study examining the formation of consolidation induced defects in dry textile composites," in *13th International Conference on Textile Composites*, vol. 406 of *IOP Conference Series: Materials Science and Engineering*, IOP Publishing Ltd., 2018.

[51] P. Harrison, M. F. Alvarez, and D. Anderson, "Towards comprehensive characterisation and modelling of the forming and wrinkling mechanics of engineering fabrics," *International Journal of Solids and Structures*, vol. 154, pp. 2–18, Jan 2017.

[52] T. J. Dodwell, R. Butler, and G. W. Hunt, "Out-of-plane ply wrinkling defects during consolidation over an external radius," *Composites Science and Technology*, vol. 105, pp. 151–159, Oct 2014.

[53] T. Grankäll, P. Hallander, and M. Åkermo, "Geometric compensation of convex forming tools for successful final processing in concave cure tools - an experimental study," *Composites: Part A*, vol. 116, pp. 187–196, 2019.

[54] P. Boisse, N. Hamila, and A. Madeo, "Modelling the development of defects during composite reinforcements and prepreg forming," *Philosophical Transactions of the Royal Society A*, vol. 374, Mar 2016.

[55] S. Erland, T. J. Dodwell, and R. Butler, "Characterisation of inter-ply shear in uncured carbon fibre prepreg," *Composites: Part A*, vol. 77, pp. 210–218, Jul 2015.

[56] W. W. Johanns, "The effect of tow grouping resolution on shearing deformation of unidirectional non-crimp fabric," Master's thesis, Iowa State University, 2012.

[57] I. Taha, Y. Abdin, and S. Ebeid, "Comparison of picture frame and bias-extension tests for the characterization of shear behaviour in natural fibre woven fabrics," *Fibers and Polymers*, vol. 14, pp. 338–344, Feb 2013.

[58] A. G. Prodromou and J. Chen, "On the relationship between shear angle and wrinkling of textile composite preforms," *Composites: Part A*, vol. 28, pp. 491–503, 1997.

[59] T. Gereke, O. Döbrich, M. Hübner, and C. Cherif, "Experimental and computational composite textile reinforcement forming: a review," *Composites: Part A*, vol. 46, pp. 1–10, 2013.

[60] S. Allaoui, G. Hivet, A. Wendling, P. Ouagne, and D. Soulat, "Influence of the dry woven fabrics meso-structure on fabric/fabric contact behavior," *Journal of Composite Materials*, vol. 46, pp. 627–639, Jan 2012.

[61] G. Hivet, S. Allaoui, B. T. Cam, P. Ouagne, and D. Soulat, "Design and potentiality of an apparatus for measuring yarn/yarn and fabric/fabric friction," *Experimental Mechanics*, vol. 52, no. 8, pp. 1123–1136, 2012.

[62] M. R. Piggott, "The effect of fibre waviness on the mechanical properties of unidirectional fibre composites: a review," *Composites Science and Technology*, vol. 53, pp. 201–205, 1995.

[63] J. Zhu, J. Wang, and L. Zu, "Influence of out-of-plane ply waviness on elastic properties of composite laminates under uniaxial loading," *Composite Structures*, vol. 132, pp. 440–450, May 2015.

[64] J. Zhu, J. Wang, A. Ni, W. Guo, X. Li, and Y. Wu, "A multi-parameter model for stiffness prediction of composite laminates with out-of-plane ply waviness," *Composite Structures*, vol. 185, pp. 327–337, 2018.

[65] N. Xie, R. A. Smith, S. Mukhopadhyay, and S. R. Hallett, "A numerical study on the influence of composite wrinkle defect geometry on compressive strength," *Materials and Design*, vol. 140, pp. 7–20, Nov 2018.

[66] B. D. Allison and J. L. Evans, "Effect of fiber waviness on the bending behavior of s-glass/epoxy composites," *Materials and Design*, vol. 36, pp. 316–322, 2012.

[67] A. Altmann, P. Gesell, and K. Drechsler, "Strength prediction of ply waviness in composite materials considering matrix dominated effects," *Composite Structures*, vol. 127, pp. 51–59, Mar 2015.

[68] S. Mukhopadhyay, M. I. Jones, and S. R. Hallett, "Compressive failure of laminates containing an embedded wrinkle; experimental and numerical study," *Composites: Part A*, vol. 73, pp. 132–142, Mar 2015.

[69] S. S. Nimbal, M. M. Banker, A. Roopa, B. Varughese, and R. Sundaram, "Effect of gap induced waviness on compressive strength of laminated composites," in *International Conference on Advancements in Aeromechanical Materials for Manufacturing*, pp. 8355–8369, 2016.

[70] S. Mukhopadhyay, M. I. Jones, and S. R. Hallett, "Tensile failure of laminates containing an embedded wrinkle; numerical and experimental study," *Composites: Part A*, vol. 77, pp. 219–228, Jul 2015.

[71] L. D. Bloom, J. Wang, and K. D. Potter, "Damage progression and defect sensitivity: an experimental study of representative wrinkles in tension," *Composites: Part B*, vol. 45, pp. 449–458, 2013.

[72] K. Potter, B. Khan, M. Wisnom, T. Bell, and J. Stevens, "Variability, fibre waviness and misalignment in the determination of the properties of composite materials and structures," *Composites: Part A*, vol. 39, pp. 1343–1354, Sep 2008.

[73] S. Hörrmann, A. Adumitroaie, C. Viechtbauer, and M. Schagerl, "The effect of fiber waviness on the fatigue life of CFRP materials," *International Journal of Fatigue*, vol. 90, pp. 139–147, Apr 2016.

[74] S. Mukhopadhyay, O. J. Nixon-Pearson, and S. R. Hallett, "An experimental and numerical study on fatigue damage development in laminates containing embedded wrinkle defects," *International Journal of Fatigue*, vol. 107, pp. 1–12, 2018.

[75] L. Daelemans, "Realistic numerical modelling of the yarn behaviour in the production of stitched sandwich panels," Master's thesis, Ghent University, May 2013.

[76] S. Green, A. Long, B. El Said, and S. R. Hallett, "Numerical modelling of 3D woven composite preform deformations," *Composite Structures*, vol. 108, pp. 747–756, Feb 2014.

[77] T. Diehl, R. D. Dixon, M. A. Lamontia, and J. A. Hanks, "The development and use of a robust modeling approach for predicting structural performance of woven fabrics using ABAQUS," in *ABAQUS Users' Conference*, 2003.

[78] Dassault Systèmes, *SIMULIA User Assistance 2018*, 2017.

[79] B. Nadler, P. Papadopoulos, and D. Steigmann, "Multiscale constitutive modeling and numerical simulation of fabric material," *International Journal of Solids and Structures*, vol. 43, pp. 206–221, 2006.

[80] P. Boisse, N. Hamila, E. Vidal-Sallé, and F. Dumont, "Simulation of wrinkling during textile composite reinforcement forming - influence of tensile, in-plane shear and bending stiffnesses," *Composites Science and Technology*, vol. 71, pp. 683–692, Jan 2011.

[81] S. Allaoui, P. Boisse, S. Chatel, N. Hamila, G. Hivet, D. Soulat, and E. Vidal-Sallé, "Experimental and numerical analyses of textile reinforcement forming of a tetrahedral shape," *Composites: Part A*, vol. 42, pp. 612–622, Feb 2011.

[82] S. Kawabata, M. Niwa, and H. Kawai, "The finite-deformation theory of plain-weave fabrics, part I: the biaxial-deformation theory," *Journal of the Textile Institute*, vol. 64, no. 1, pp. 21–46, 1973.

[83] S. Kawabata, M. Niwa, and H. Kawai, "The finite-deformation theory of plain-weave fabrics, part II: the uniaxial-deformation theory," *Journal of the Textile Institute*, vol. 64, no. 2, pp. 47–61, 1973.

[84] S. Kawabata, M. Niwa, and H. Kawai, "The finite-deformation theory of plain-weave fabrics, part III: the shear-deformation theory," *Journal of the Textile Institute*, vol. 64, no. 3, pp. 62–85, 1973.

[85] A. Cherouat and J. L. Billoet, "Mechanical and numerical modelling of composite manufacturing processes deep-drawing and laying-up of thin pre-impregnated woven fabrics," *Journal of Materials Processing Technology*, vol. 118, pp. 460–471, Dec 2001.

[86] M. J. King, P. Jearanaisilawong, and S. Socrate, "A continuum constitutive model for the mechanical behavior of woven fabrics," *International Journal of Solids and Structures*, vol. 42, pp. 3867–3896, Jun 2005.

[87] P. Harrison, "Modelling the forming mechanics of engineering fabrics using a mutually constrained pantographic beam and membrane mesh," *Composites: Part A*, vol. 81, pp. 145–157, Nov 2015.

[88] A. Gasser, P. Boisse, and S. Hanklar, "Mechanical behaviour of dry fabric reinforcements - 3D simulations versus biaxial tests," *Computational Materials Science*, vol. 17, no. 1, pp. 7–20, 2000.

[89] P. Boisse, K. Buet, A. Gasser, and J. Launay, "Meso/macro-mechanical behaviour of textile reinforcements for thin composites," *Composites Science and Technology*, vol. 61, no. 3, pp. 395–401, 2001.

[90] J. Page and J. Wang, "Prediction of shear force using 3D non-linear FEM analyses for a plain weave carbon fabric in a bias extension state," *Finite Elements in Analysis and Design*, vol. 38, no. 8, pp. 755–764, 2002.

[91] R. Barauskas and A. Abraitiené, "Computational analysis of impact of a bullet against the multilayer fabrics in LS-DYNA," *International Journal of Impact Engineering*, vol. 34, pp. 1286–1305, jul 2007.

[92] P. Boisse, A. Gasser, and G. Hivet, "Analyses of fabric tensile behaviour: determination of the biaxial tension-strain surfaces and their use in forming simulations," *Composites: Part A*, vol. 32, no. 10, pp. 1395–1414, 2001.

[93] P. Boisse, A. Gasser, B. Hagege, and J. L. Billoet, "Analysis of the mechanical behaviour of woven fibrous material using virtual tests at the unit cell level," *Journal of Materials Science*, vol. 40, no. 22, pp. 5955–5962, 2005.

[94] P. Badel, E. Vidal-Sallé, and P. Boisse, "Computational determination of in-plane shear mechanical behaviour of textile composite reinforcements," *Computational Materials Science*, vol. 40, no. 4, pp. 439–448, 2007.

[95] P. Badel, E. Vidal-Sallé, and P. Boisse, "Large deformation analysis of fibrous materials using rate constitutive equations," *Computers & Structures*, vol. 86, no. 11, pp. 1164–1175, 2008.

[96] Q. T. Nguyen, E. Vidal-Sallé, P. Boisse, C. H. Park, A. Saouab, J. Bréard, and G. Hivet, "Mesoscopic scale analyses of textile composite reinforcement compaction," *Composites: Part B*, vol. 44, pp. 231–241, jan 2013.

[97] Y. Wang and X. Sun, "Digital-element simulation of textile processes," *Composites Science and Technology*, vol. 61, no. 2, pp. 311–319, 2001.

[98] G. Zhou, X. Sun, and Y. Wang, "Multi-chain digital element analysis in textile mechanics," *Composites Science and Technology*, vol. 64, pp. 239–244, Feb 2004.

[99] Y. Miao, E. Zhou, Y. Wang, and B. A. Cheeseman, "Mechanics of textile composites: micro-geometry," *Composites Science and Technology*, vol. 68, pp. 1671–1678, Jun 2008.

[100] Y. Wang, Y. Miao, D. Swenson, B. A. Cheeseman, C. F. Yen, and B. LaMattina, "Digital element approach for simulating impact and penetration of textiles," *International Journal of Impact Engineering*, vol. 37, pp. 552–560, May 2010.

[101] D. Durville, "Modelling of contact-friction interactions in entangled fibrous materials.," in *6th World Wide Congress on Computational Mechanics*, 2004.

[102] D. Durville, "Numerical simulation of entangled materials mechanical properties," *Journal of Materials Science*, vol. 40, no. 22, pp. 5941–5948, 2005.

[103] D. Durville, "Finite element simulation of textile materials at mesoscopic scale," *Finite Element Modelling of Textiles and Textile Composites*, 2007.

[104] D. Durville, "Simulation of the mechanical behaviour of woven fabrics at the scale of fibers," *International Journal of Material Forming*, vol. 3, no. 2, pp. 1241–1251, 2010.

[105] N. D. Chakladar, P. Mandal, P. Potluri, and J. Hearle, "Application of ABAQUS beam model to mod elling mechanical properties of woven fabrics," in *5th World Conference on 3D Fabrics and Their Applications*, (Delhi), Dec 2013.

[106] Y. Mahadik and S. R. Hallett, "Finite element modelling of tow geometry in 3D woven fabrics," *Composites: Part A*, vol. 41, no. 9, pp. 1192–1200, 2010.

[107] A. J. Thompson, B. El Said, D. Ivanov, J. P. H. Belnoue, and S. R. Hallett, "High fidelity modelling of the compression behaviour of 2D woven fabrics," *International Journal of Solids and Structures*, vol. 154, pp. 104–113, 2018.

[108] M. Duhovic and D. Bhattacharyya, "Simulating the deformation mechanisms of knitted fabric composites," *Composites: Part A*, vol. 37, no. 11, pp. 1897–1915, 2006.

[109] L. Van Langenhove, "Simulating the mechanical properties of a yarn based on the properties and arrangement of its fibers - part I: the finite element model," *Textile Research Journal*, vol. 67, no. 4, pp. 263–268, 1997.

[110] L. Van Langenhove, "Simulating the mechanical properties of a yarn based on the properties and arrangement of its fibers - part II: results of simulations," *Textile Research Journal*, vol. 67, no. 5, pp. 342–347, 1997.

[111] L. Van Langenhove, "Simulating the mechanical properties of a yarn based on the properties and arrangement of its fibers - part III: practical measurements," *Textile Research Journal*, vol. 67, no. 6, pp. 406–412, 1997.

[112] J. Rybicka, A. Tiwari, P. A. Del Campo, and J. Howarth, "Capturing composites manufacturing waste flows through process mapping," *Journal of Cleaner Production*, vol. 91, pp. 251–261, Mar 2015.

[113] M. K. Hagnell and M. Åkermo, "Cost efficiency, integration and assembly of a generic composite aeronautical wing box," *Composite Structures*, vol. 152, pp. 1014–1023, 2016.

[114] M. K. Hagnell and M. Åkermo, "A composite cost model for the aeronautical industry: methodology and case study," *Composites: Part B*, vol. 79, pp. 254–261, 2015.

[115] M. K. Hagnell, "The development of a technical cost model for composites - adapted to the automotive industry," Master's thesis, KTH Royal Institute of Technology - School of Engineering Sciences, 2013.

[116] K. Potter, "Beyond the pin-jointed net: maximising the deformability of aligned continuous fibre reinforcements," *Composites: Part A*, vol. 33, pp. 677–686, Jan 2002.

[117] P-D Interglas Technologies GmbH, "Product information."

[118] R&G Faserverbundwerkstoffe GmbH, "Safety data sheet," Im Meiel 7 - 13, D-71111 Waldenbuch, Germany, Oct 2014.

[119] R&G, "Faserverbundwerkstoffe - composite technology." Online.

[120] Y. Nawab, T. Hamdani, and K. Shaker, *Structural textile design: interlacing and interlooping*. CRC Press, Mar 2017.

[121] F. T. Wallenberger, J. C. Watson, H. Li, and PPG Industries Inc., *ASM Handbook: Composites*, vol. 21. ASM International, 2001.

[122] Hexion, "Technical data sheet: EPIKOTE Resin MGS RIMR 135 and EPIKURE Curing Agent MGS RIMH 134 - RIMH 137," Aug 2006.

[123] Simuleon, "SIMULIA industry solutions." Online, May 2019.

[124] P. Wang, N. Hamila, and P. Boisse, "Thermoforming simulation of multilayer composites with continuous fibres and thermoplastic matrix," *Composites: Part B*, vol. 52, pp. 127–136, Mar 2013.

[125] D. Dörr, W. Brymerski, S. Ropers, D. Leutz, T. Joppich, L. Kärger, and F. Henning, "A benchmark study of finite element codes for forming simulation of thermoplastic UD-tapes," in *1st CIRP Conference on Composite Materials Parts Manufacturing*, vol. 66, pp. 101–106, 2017.

[126] D. Dörr, F. J. Schirmaier, F. Henning, and L. Kärger, "A viscoelastic approach for modeling bending behavior in finite element forming simulation of continuously fiber reinforced composites," *Composites: Part A*, vol. 94, pp. 113–123, Nov 2017.

[127] S. C. Garcea, Y. Wang, and P. J. Withers, "X-ray computed tomography of polymer composites," *Composites Science and Technology*, pp. 1–15, Oct 2017.

[128] J. Hemmer, C. Burtin, S. Comas-Cardona, C. Binetruy, T. Savart, and A. Babeau, "Unloading during the infusion process: direct measurement of the dual-scale fibrous microstructure evolution with X-ray computed tomography," *Composites: Part A*, Sep 2018.

[129] J. Y. Buffiere, E. Maire, J. Adrien, J. P. Masse, and E. Boller, "In situ experiments with X-ray tomography: an attractive tool for experimental mechanics," *Experimental Mechanics*, vol. 50, pp. 289–305, Jan 2010.

[130] J. F. Van Stappen, T. De Kock, G. De Schutter, and V. Cnudde, "Uniaxial compressive strength measurements of limestone plugs and cores: a size comparison and X-ray CT study," *Bulletin of Engineering Geology and the Environment*, Jan 2019.

[131] B. Cornelissen and R. Akkerman, "Analysis of yarn bending behaviour," in *17th International Conference on Composite Materials*, (Edinburgh, Scotland), The British Composites Society, Jul 2009.

[132] D. Petrulis and S. Petrulyté, "Properties of close packing of filaments in yarn," *Fibres & Textiles in Eastern Europe*, vol. 11, pp. 16–20, Mar 2003.

[133] K. B. Iyer and R. M. Phatarfod, "Some aspects of yarn structure," *Journal of Textile Institute Transactions*, vol. 56, no. 5, pp. 225–247, 1965.

[134] F. T. Peirce, "The "handle" of cloth as a measurable quantity," *Journal of Textile Institute Transactions*, vol. 21, no. 9, 1930.

[135] N. Lammens, M. Kersemans, G. Luyckx, W. Van Paepegem, and J. Degrieck, "Improved accuracy in the determination of flexural rigidity of textile fabrics by the Peirce cantilever test (ASTM D1388)," *Textile Research Journal*, pp. 1–8, 2014.

[136] S. Rajagopalan, "Advances in weaving technology and looms," aug 2004. S.S.M. College of Engineering, Komarapalayam.

Appendix A

Python code

A.1 ABAQUS input file editor

[Redacted for confidentiality]

A.2 ABAQUS output node reader

[Redacted for confidentiality]